BLOOD FLOW IN MICROCIRCULATION: INVESTIGATING THE CELL-FREE LAYER WITH CAPILLARY MICROCHANNELS

MAYA SALAME

THESIS SUBMITTED TO THE UNIVERSITY OF OTTAWA IN PARTIAL
FULFILLMENT OF THE REQUIREMENTS FOR THE DEGREE OF
MASTER OF APPLIED SCIENCE, BIOMEDICAL ENGINEERING

DEPARTMENT OF MECHANICAL ENGINEERING
FACULTY OF ENGINEERING
UNIVERSITY OF OTTAWA

MARIANNE FENECH

Abstract

Blood flow in the microcirculation is governed by complex interactions between red blood cells (RBCs) and plasma, resulting in distinct rheological behaviors that differ from bulk flow properties. A key microvascular phenomenon is the cell-free layer (CFL)—a plasma-rich region near vessel walls that plays a critical role in vascular resistance, oxygen transport, and nutrient exchange. Despite its physiological significance, the primary mechanisms driving CFL formation remain debated, and accurate measurement techniques are essential for a comprehensive understanding of this phenomenon. This study aims to investigate how channel size (25 and 50 µm), hematocrit, and suspension medium influence non-Newtonian properties and CFL formation. It also seeks to evaluate the suitability of different rheological models in capturing CFL behavior and compare measurement techniques for CFL quantification.

Microfluidic experiments were conducted using blood suspensions under controlled flow conditions. Various rheological models—including the Newtonian, Power Law, and Carreau Models—were analyzed to determine their effectiveness in predicting CFL behavior. The Double-Parameter Power (DPP) fit was also assessed for velocity profile characterization. CFL thickness was measured using both optical imaging and hydrodynamic methods, providing comparative insights into their accuracy and reliability.

The results indicate that the Core-Plasma Model, developed in this work, best captures the two-phase nature of blood flow by distinguishing the RBC-rich core from the plasma layer. Optical imaging was found to be the most reliable and accurate method for CFL measurement, while hydrodynamic methods offered indirect but complementary insights. Additionally, shear rate gradients were identified as a dominant factor in CFL formation. These findings enhance the understanding of CFL dynamics in microcirculation, providing a more accurate framework for modeling blood flow under physiologically relevant conditions.

Keywords: microcirculation, cell-free layer, non-Newtonian blood flow, hemodynamics, red blood cells, microfluidics, gradient of shear rate

Declaration of Authorship

I hereby certify that this thesis is entirely my own original work except where otherwise indicated. I am aware of the University's regulations concerning plagiarism, including those concerning consequent disciplinary actions. Any use of the works of any other author, in any form, is properly acknowledged at their point of use.

STATEMENT OF ETHICS APPROVAL

The research involves human subjects. The experimental work was done in compliance with the ethics committee of the University of Ottawa. File No. H-03-19-3441.

ACKNOWLEDGEMENTS

I would like to express my gratitude to Dr. Marianne Fenech for her unwavering support, mentorship, and patience throughout my studies. Your optimism, encouragement, and expertise have inspired me to strive for the best. I would like to give acknowledgments to Dr. Manouk Abkarian, collaborator in Montpellier, France, for mentoring me in microscopy and microfluidic techniques. I would like to thank my lab members for their continued support. I would also like to thank the Natural Sciences and Engineering Research Council of Canada (NSERC) and Mitacs Globalink for funding my research. Most importantly, I want to thank my parents—my dad, my guiding angel, and my mom, my greatest support.

CONTENTS

ABSTRACT **ii**

DECLARATION OF AUTHORSHIP **iii**

STATEMENT OF ETHICS APPROVAL **iv**

ACKNOWLEDGEMENTS **v**

LIST OF FIGURES **ix**

LIST OF TABLES **xi**

LIST OF ABBREVIATIONS **xii**

LIST OF SYMBOLS **xiii**

1 INTRODUCTION **1**
  1.1 Research Motivation 1
  1.2 Research Objectives 3
  1.3 Thesis Structure 4

2 LITERATURE REVIEW **6**
  2.1 Blood Composition 6
    2.1.1 Red Blood Cells 7
    2.1.2 Plasma 8
    2.1.3 Hematocrit 9
  2.2 Microcirculation 10
  2.3 Aggregation 11

2.4 Cell-Free Layer Formation 12
2.4.1 Established Theories of CFL Influencing Factors 14
2.4.2 Emerging Theories of CFL Influencing Factors 19
2.5 Blood Flow Modeling in Microcirculation 22
2.5.1 Newtonian Model 23
2.5.2 Power Law Model 24
2.5.3 Carreau Model 26
2.5.4 Double-Parameter Power Fit 28
2.5.5 Comparing Models with Blood Viscosity and Shear Rate 30
2.6 Conclusion 30

3 METHODOLOGY AND MATERIALS **33**

3.1 Microchannel Fabrication 33
3.2 Fluid Preparation 35
3.2.1 PBS Suspension 37
3.2.2 Plasma Suspension 38
3.2.3 Fluorescent Tracer Particles 38
3.2.4 Hematocrit Verification 39
3.3 Experimental Setup and Measurements 41
3.3.1 Flow Rate Measurements 43
3.3.2 Image Post-Processing 44
3.4 Mathematical Analysis of Velocity Profiles 49
3.4.1 Our Developed Blood Model: Core-Plasma 50
3.4.2 Determining Shear Rate, Shear Rate Gradient, and Shear Stress . . 54
3.4.3 Determining Local Viscosity Using the Carreau Model 56
3.4.4 MATLAB Framework 58
3.5 Statistical Analysis Methods 60

4 COMPARATIVE ANALYSIS OF BLOOD FLOW MODELS **63**

4.1 Results 63
4.1.1 Velocity Profiles and Model Performance 64
4.1.2 Characterization of Non-Newtonian Parameters 68
4.1.3 Comparison of Optical and Hydrodynamic CFL Measurements . . . 79
4.2 Discussion 81
4.2.1 Strengths and Limitations of Rheological Models and Fits 81
4.2.2 Interpretation of Non-Newtonian Parameters 83

4.2.3 Accuracy and Reliability of CFL Measurements 88

5 EVALUATING CELL-FREE LAYER INFLUENCING FACTORS **90**
5.1 Results 90
5.1.1 Impact of Hematocrit 90
5.1.2 Impact of Gradient of Shear Rate 92
5.1.3 Impact of Shear Stress 96
5.2 Discussion 97
5.2.1 Hematocrit-Driven CFL Variability 99
5.2.2 Shear Rate Gradient as a Determining Factor 100
5.2.3 Shear Stress, an Insufficient Predictor of CFL 103
5.2.4 Understanding Contradictions in Literature 104

6 CONCLUSIONS AND FUTURE WORK **108**
6.1 Optimal Model Selection for Microvascular Blood Flow 108
6.2 Unifying Mechanisms Governing CFL Formation 110
6.3 Proposal for Future Work 112

APPENDICES **115**

A SUPPORTING INFORMATION **116**
A.1 Micro-Particle Image Velocimetry 116
A.1.1 Limitations of µPIV 117
A.1.2 Correlation Techniques in µPIV 119
A.1.3 Application of μPIV in Blood Rheology Research 122
A.2 Experimental Flow Measurements 122
A.3 Core-Plasma Model Derivation 124
A.3.1 Governing Equations and Assumptions 125
A.3.2 Flow Rate 132
A.3.3 Shear Rate 135
A.3.4 Gradient of Shear Rate 136
A.4 Comparison of Imposed, Measured, and Optimized Pressure Drops 136

REFERENCES **141**

List of Figures

2.1 Top and side views of a typical human red blood cell 8
2.2 Visualization of red blood cell aggregation in buffer and dextran solutions . 12
2.3 Schematic of blood flow in a microchannel 13
2.4 Relative apparent viscosity of blood as a function of tube diameter 17
2.5 Schematic diagram of the force balance between cell-cell and cell-wall interactions 21
2.6 Log-log plot of predicted viscosity of blood by Carreau, Power Law, and Newtonian Model 31

3.1 Fabricated Microchannel with and without glycerol submersion of glass capillary 35
3.2 Assembly steps for microchannel fabrication 36
3.3 Crit Spin micro-hematocrit tubes displaying red blood cell suspensions at various hematocrit 40
3.4 Schematic of experimental setup for velocity profile and cell-free layer thickness measurement 41
3.5 High-speed camera images for a 50 µm diameter channel with PBS suspension 46
3.6 Graphical user interface on Matlab for cell-free layer thickness acquisition . 47
3.7 µPIV Velocity Profile Acquisition Workflow 49
3.8 Velocity profile illustrating the Core-Plasma Model in a 50 µm channel . . 52
3.9 Shear rate profile and discontinuity identification in 50 µm and 25 µm microchannels 57

4.1 Velocity and shear rate distributions with RMS error of 15% Ht plasma suspension case within 50 µm microchannel 65
4.2 Velocity and shear rate distributions with RMS error of 15% Ht plasma suspension case within 25 µm microchannel 66

4.3 Comparison of velocity and shear rate RMS values across various model types and conditions 67
4.4 Apparent viscosity derived from Poiseuille as a function of experimental pressure gradient for a 50 µm and 25 µm microchannel 71
4.5 Local viscosity from the Carreau Model compared to local shear rate for a 50 µm and 25 µm microchannel 72
4.6 Comparison of Carreau Model's zero viscosity (μ_0) trends across varying conditions 73
4.7 Comparison of Carreau Model's infinite viscosity (μ_∞) trends across varying conditions 74
4.8 Power Law Model parameters across varying conditions 75
4.9 Double-Parameter Power Fit parameters across varying conditions 77
4.10 Core-Plasma Model parameters across varying conditions 78
4.11 Comparison between optical and hydrodynamic cell-free layer thickness measurements scatter plot 79
4.12 Comparison between optical and hydrodynamic cell-free layer measurement box plot 80
4.13 Relationship between optical cell-free layer and Power Law Model parameters 86

5.1 Comparison of the optical cell-free layer across varying conditions 92
5.2 Relationship between optical cell-free layer and shear rate at discontinuity 94
5.3 Relationship between optical cell-free layer and gradient of shear rate . . . 95
5.4 Relationship between optical cell-free layer and shear stress 98
5.5 Schematic of shear rate gradient effects on red blood cell distribution . . . 102
5.6 Comparison of cell-free layer thickness between present study and literature 104

A.1 μPIV analysis of double frame-single exposure recordings of digital cross-correlation method 117
A.2 Schematic of a typical 2D, planar µPIV system 118
A.3 Ensemble correlation technique 121
A.4 Pressure drop as a function of flow rate for 50 µm and 25 µm microchannels with varying suspension mediums 139
A.5 Computed pressure drop from Core-Plasma Model compared to measured pressure drop 140

List of Tables

2.1 Summary of literature on governing factors of cell-free layer (δ) formation . 19

3.1 Summary of models and computational methods with initialized, fixed, and output parameters used in the MATLAB framework 60

4.1 Summary of Non-Newtonian parameters across varying channel sizes and hematocrit with comparison to the literature 70

A.1 Flow rate measurements for a 25 µm channel with PBS-suspension. Values are in [μL/min]. 123
A.2 Flow rate measurements for a 25 µm channel with plasma-suspension. Values are in [μL/min]. 123
A.3 Flow rate measurements for a 50 µm channel with PBS-suspension. Values are in [μL/min]. 124
A.4 Flow rate measurements for a 50 µm channel with plasma-suspension. Values are in [μL/min]. 124

List of Abbreviations

CCD	charged coupled device 42
CFL	cell-free layer 2, 52
DI	deionized water 34
DOC	depth of correlation 118
DPP	double-parameter power 28
dt	time interval between consecutive laser pulses in micro-particle image velocimetry 48
EDTA	ethylenediaminetetraacetic acid 35
HSC	high-speed camera 33
Ht	hematocrit 2
OD	outer diameter 34
OptiPrep®	Iodixanol 37
PBS	phosphate buffered saline 37
PCV	packed cell volume 39
PLL-PEG	poly(L-Lysine)-PEG methyl ether 34
RBCs	red blood cells 1
RMS	root mean square 61
WBCs	white blood cells 1
µPIV	micro-particle image velocimetry 33

LIST OF SYMBOLS

D	Channel or vessel diameter (m) 14
k_1	Core bluntness shape factor (-) 28
k_2	Wall bluntness shape factor (-) 28
K_{cp}	Core-Plasma Model consistency index in power-law model (Pa·s^n) 50
K_p	Power law consistency index in power-law model (Pa·s^n) 25
L	Channel or vessel length (m) 10
m_1	Slope of the linear region for red blood cell core in the shear rate versus radial position plot (-) 55
m_2	Slope of the linear region for cell-free layer in the shear rate versus radial position plot (-) 55
N	Total number of data points (-) 61
n_c	Carreau Model flow behavior index (-) 27
n_{cp}	Core-Plasma Model flow behavior index (-) 50
n_p	Power law flow behavior index (-) 25
P_{exp}	Measured pressure from pressure controller (mBar) 59
PG_{cp}	Pressure gradient from optimization of Core-Plasma Model (Pa/m) 60
PG_{exp}	Pressure gradient from experimental values (Pa/m) 59
Q	Volumetric flow rate (m^3/s or μL/min) 10
Q_{exp}	Measured flow rate using flow sensor (μl/min) 59
R	Channel or vessel radius (m) 23

r	Radial distance from channel center (m) 10
r_{ip}	Radial position of shear rate at discontinuity (m) 55
u	Velocity measurement from μPIV (m/s) 58
u_{max}	Maximum velocity measurement from μPIV (m/s) 28
$\bar{v}$	Mean flow velocity across the vessel cross-section (m/s) 16
V_{blood}	Total blood volume (μL) 9
V_{RBC}	Volume of red blood cells in total blood volume (μL) 9
y_i^{exp}	Experimentally measured value at point i 61
y_i^{model}	Model-predicted value at point i 61
δ_o	Optical cell-free layer thickness (μm) 44
δ_h	Hydrodynamic cell-free layer thickness (μm) 54
δ_{core}	Red blood cell core thickness (μm) 45
ΔP	Pressure drop (Pa) 10
$\dot{\gamma}$	Shear rate (s^{-1}) 13
$\dot{\gamma}_w$	Wall shear rate (s^{-1}) 13
$\nabla\dot{\gamma}$	Shear rate gradient (s$^{-1}\cdot\mu$m^{-1}) 21
λ_c	Time constant in Carreau Model (s) 27
μ	Viscosity (mPa·s) 10
μ_{app}	Apparent viscosity (mPa·s) 60
μ_p	Plasma viscosity (mPa·s) 50
μ_0	Zero-shear viscosity (mPa·s) 27
μ_∞	Infinite-shear viscosity (mPa·s) 27
μ_c	Carreau Model viscosity (mPa·s) 60
τ	Shear stress (Pa) 60
τ_w	Wall shear stress (Pa) 13

Chapter 1

Introduction

1.1 Research Motivation

Blood is a complex suspension of cellular components, including red blood cells (RBCs), white blood cells (WBCs), and platelets, all suspended in plasma. Among these, RBCs are the most abundant and play a critical role in oxygen transport. These cells are composed of a concentrated hemoglobin solution encased in a highly flexible membrane. Their deformability enables them to pass through the narrowest capillaries, ensuring efficient gas exchange and nutrient delivery at the microcirculatory level [1].

The microcirculation represents the smallest network of blood vessels in the body, comprising of capillaries, arterioles, and venules. This network is responsible for regulating blood flow to individual organs and facilitating exchange between blood and tissue, making it a crucial component of the cardiovascular system. Unlike in larger vessels, where blood can often be approximated as a Newtonian fluid [1, 2], the confined nature of microcirculatory vessels—typically less than 100 µm in diameter [3]—means that RBCs play an important role in shaping flow properties.

One of the most critical yet poorly understood phenomena in microcirculatory flow is the formation of the cell-free layer (CFL). As RBCs migrate toward the vessel center, they leave behind a plasma-rich region near the vessel walls [2]. This creates a two-phase flow structure, where the CFL acts as a lubrication layer with lower viscosity than the RBC-rich core. The formation of the CFL is driven by hydrodynamic interactions, including cell-wall interactions, which push RBCs away from the vessel walls, and cell-cell interactions, which promote RBC dispersion within the core [4].

Despite its recognized importance in microcirculatory flow, the mechanisms governing CFL formation remain widely debated. The Fåhraeus–Lindqvist effect, first described in 1931, established that blood viscosity decreases as vessel diameter decreases, driven by the migration of RBCs toward the vessel center. This early understanding suggested that CFL formation was primarily dictated by vessel diameter, with smaller microchannels promoting a more pronounced CFL [5]. However, later studies challenged the idea that diameter alone governs CFL behavior, pointing to additional factors such as RBC aggregation, hematocrit (Ht), and shear rate.

Some studies suggest that RBC aggregation is the dominant variable at lower shear rates, where aggregation reduces CFL, while at moderate shear rates, aggregation enhances CFL formation [6, 7]. Others suggest that Ht plays a greater role, with increased RBC concentrations leading to a thinner CFL due to higher cell-cell interactions [2, 8]. Meanwhile, additional studies point to shear rate as the key determinant, as RBC aggregation and deformation respond to changes in local shear conditions [4, 9]. The lack of consensus in these findings makes it difficult to develop a unified theoretical model of CFL behavior, leading to inconsistencies in blood flow predictions, particularly when transitioning between Newtonian and non-Newtonian modeling approaches. Understanding the mechanisms governing CFL formation is essential for accurately modeling microcirculatory flow, predicting oxygen transport efficiency, and improving disease diagnostics in the field of microfluidic technology [10].

Addressing this gap requires a systematic investigation that accounts for multiple variables under controlled conditions. This study aims to resolve these discrepancies through *in vitro* experiments using capillary microchannels (25–50 µm), allowing for direct measurement of CFL thickness under varying flow conditions, Ht levels, and aggregation states. This study also aims to develop a more accurate blood flow model that captures the transition between Newtonian and non-Newtonian behavior while identifying the primary drivers of CFL formation at the microscale.

1.2 Research Objectives

The ultimate objective of this experimental work is to understand the rheological properties of microcirculation, with a specific emphasis on CFL formation. This entails the following components:

- Characterizing the local velocity profile in capillary microchannels of varying diameter (50 µm and 25 µm), flow rates, suspension mediums, and hematocrit levels.

- To develop and validate rheological blood flow models that capture the dual-part Newtonian and non-Newtonian behavior, comparing various established models to identify which provides the most accurate representation of CFL dynamics.
- To directly compare different CFL measurement techniques (optical and hydrodynamic) to determine the most reliable approach for quantifying CFL thickness.
- To identify and clarify the primary mechanisms driving CFL formation, resolving existing contradictions in the literature.

1.3 Thesis Structure

The thesis is structured as follows:

Chapter 1: Introduction presents the research motivation, defines clear research objectives, and outlines the significance and scope of this work.

Chapter 2: Literature Review provides foundational background on blood composition, rheological properties, and microcirculatory dynamics. It critically evaluates existing studies from *in vitro*, *in vivo*, and computational approaches, emphasizing key concepts such as CFL formation, aggregation, and shear rate. The chapter identifies critical gaps and emphasizes the necessity for an improved understanding of CFL behavior.

Chapter 3: Methodology and Materials describes the materials, experimental setups, and data acquisition techniques. It also provides a detailed explanation of data processing and mathematical analysis, including velocity measurements and CFL quantification, ensuring experimental reproducibility.

Chapter 4: Comparative Analysis of Blood Flow Models evaluates various blood rheology models, assessing their accuracy in predicting experimentally observed velocity profiles, shear rates, and viscosity trends. This chapter recommends the most suitable blood rheology model for capturing CFL dynamics. It thoroughly examines how non-Newtonian parameters are influenced by hematocrit, suspension medium, and channel size. Additionally, it compares optical and hydrodynamic CFL measurement methods to determine the most reliable approach.

Chapter 5: Evaluating Cell-Free Layer Influencing Factors focuses specifically on identifying and clarifying the primary mechanisms that influence CFL thickness in microchannels. Hematocrit, shear rate, gradient of shear rate, and shear stress are analyzed to resolve the existing contradictions in the literature. Results are compared directly with established studies to provide a coherent framework for understanding CFL formation.

Chapter 6: Conclusions and Future Work summarizes the key findings from the comparison of rheological models and velocity profile fits. It also recaps the main factors influencing cell-free layer (CFL) formation, highlighting how these findings help reconcile contradictions reported in previous literature. Finally, it outlines proposed directions for future experimental and theoretical studies aimed at advancing microcirculatory research.

CHAPTER 2

LITERATURE REVIEW

This chapter provides background on blood composition, microcirculation, and hemorheology at the microscale. It reviews factors influencing CFL formation, including RBC aggregation and Ht, alongside established and emerging theories. Blood flow models such as Newtonian, Power Law, Carreau, and Double-Parameter Power Fit are discussed, as well as CFL measurement techniques and velocity profile analysis.

2.1 BLOOD COMPOSITION

Blood is a complex, non-Newtonian fluid, with viscosity that changes depending on the shear rate. The average human body contains approximately 4.5 to 6 liters of blood, which accounts for about 6-8% of total body weight [2, 11]. In a typical human blood sample, approximately 45% consists of formed elements by volume, including red blood cells (RBCs) (95%), white blood cells (WBCs) (0.13%), and platelets (4.9%). RBCs are primarily responsible for oxygen transport from the lungs to tissues throughout the body. Each RBC contains hemoglobin, a protein that binds oxygen in the lungs for transport throughout the body and carries carbon dioxide back to the lungs for exhalation. WBCs, or leukocytes, play essential roles in immune responses and defense against infections. Platelets, small cell fragments derived from megakaryocytes in the bone marrow, are crucial for blood clotting. Upon activation, platelets become spherical and work to seal injuries in blood vessels, with an active lifespan of around 10 days. The remaining 55% of blood volume is composed of plasma, an electrolyte-rich fluid containing various proteins. These proteins, such as albumin, help increase osmotic pressure, facilitating fluid absorption into capillaries. Plasma transports a range of components, including blood cells, nutrients, waste products, hormones, and proteins, across the body [11].

2.1.1 Red Blood Cells

RBCs, or erythrocytes, are the most abundant cells in human blood and serve a critical function in oxygen and carbon dioxide transport. Structurally, RBCs are characterized by their distinctive biconcave shape, measuring approximately 6-8 µm in diameter, 2.5 µm at the thickest point, and about 1 µm at the center (Figure 2.1). This shape enhances their surface area-to-volume ratio, facilitating efficient gas exchange. Additionally, the RBC membrane is highly flexible, composed of a viscoelastic shell with an outer lipid bilayer supported by an inner network of cytoskeletal proteins. This structure allows RBCs to deform easily, enabling them to squeeze through capillaries as narrow as 5 µm [11–13].

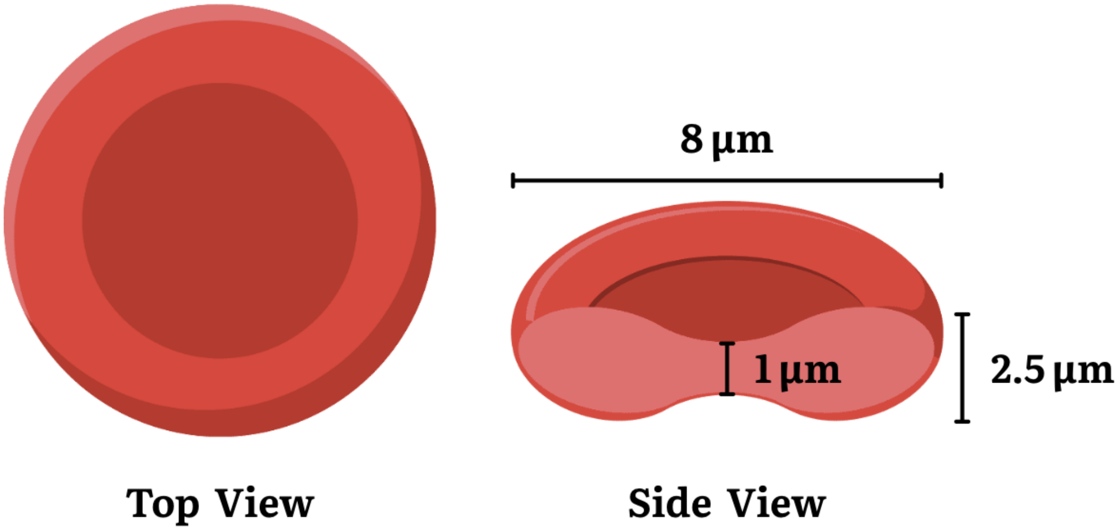

Figure 2.1: Top and side views of a typical human red blood cell (RBC). The biconcave disc has an average diameter of approximately 8 μm, a maximum thickness of 2.5 μm at the rim, and a minimum thickness of 1 μm at the center. This geometry enhances RBC deformability and surface-area-to-volume ratio, facilitating gas exchange and passage through narrow microvessels. Schematic created using Canva Pro.

2.1.2 Plasma

Plasma is a pale-yellow fluid composed primarily of water (around 90%) and serves as the medium for transporting cells, nutrients, hormones, and waste products throughout the body. Plasma plays a critical role in maintaining blood pressure, volume, and pH balance. Beyond water, plasma contains essential proteins such as albumin, globulins, and fibrinogen. Albumin helps regulate osmotic pressure, preventing fluid loss from blood vessels, while globulins participate in immune functions. Fibrinogen, meanwhile, is a key factor in blood clotting, transforming into fibrin during injury to form clots and prevent excessive blood loss [11]. In terms of rheology, plasma exhibits Newtonian behavior, meaning its viscosity remains constant across varying shear rates, unlike whole blood, which displays non-Newtonian properties due to the presence of RBCs and other cellular components [12]. Plasma has a density of about 1.035 g/cm^3 and a viscosity ranging from 0.011 to 0.016 P, slightly higher than water's viscosity of 0.01 P. This increase is due to plasma proteins that contribute to its flow resistance. Although plasma's rheological behavior may vary slightly with protein concentration and shear rates, it is generally treated as a Newtonian fluid at physiological conditions, maintaining a viscosity of around 1.2 cP at body temperature (37°C) [11, 13].

2.1.3 Hematocrit

Hematocrit (Ht) is the volume fraction of blood occupied by RBCs and is expressed as a percentage:

$$Ht = \frac{V_{\text{RBC}}}{V_{\text{blood}}} \times 100 \tag{2.1}$$

where V_{RBC} is the volume of RBCs and V_{blood} is the total blood volume. Normal Ht values typically range between 40–45% in healthy adults. Ht plays a crucial role in determining blood viscosity; higher Ht levels increase viscosity, thereby increasing flow resistance, particularly in microvascular networks [11]. The Ht in the microvascular has been reported to vary from less than 20% to 50% of that in the larger vessels in tissues [14]. *In vitro* studies often employ reduced Ht levels to simulate microcirculatory conditions and facilitate optical imaging in experimental setups [15, 16].

2.2 Microcirculation

Microcirculation comprises the smallest blood vessels—capillaries, arterioles, and venules—where essential exchanges of nutrients, gases, and waste occur between blood and tissues. Vessels in this network, typically 4–100 µm in diameter, play a key role in regulating blood flow and pressure, contributing to roughly 80% of the pressure drop from the aorta to the vena cava [1]. In microcirculation, blood flow often behaves as a non-Newtonian fluid because its viscosity changes with the shear rate. Despite this non-Newtonian behavior, the apparent viscosity of blood is often characterized using the Poiseuille equation, which describes Newtonian, laminar flow in cylindrical vessels, given by:

$$Q = \frac{\Delta P \cdot \pi \cdot r^4}{8 \cdot \mu \cdot L}$$

where Q is the flow rate, ΔP the pressure difference, r the vessel radius, μ the viscosity, and L the vessel length [17]. By rearranging this equation, microvascular resistance, largely regulated by arterioles, can be derived as follows:

$$Rf = \frac{8 \cdot \mu \cdot L}{\pi \cdot r^4}$$

This equation highlights that resistance is highly sensitive to vessel radius; even slight decreases in diameter cause a large increase in resistance, impacting blood distribution to tissues and systemic blood pressure.

2.3 Aggregation

Aggregation refers to the tendency of RBCs to cluster together, particularly under low shear stress, forming structures that resemble stacks of coins, known as rouleaux. This property is significant because of the high density of RBCs in blood (around 5 million cells per mm^3). Aggregation is a reversible process, meaning that as shear forces increase, the rouleaux can break apart [18]. RBC aggregation is influenced by the molecules present in the surrounding plasma. Certain macromolecules, like fibrinogen, encourage RBCs to stick together by creating attractive forces between them [19]. RBCs' tendency to clump together is also connected to specific health conditions, where increased aggregation is often seen, such as in diabetes, heart disease, and hypertension [11]. Studies have shown that this aggregation effect can be mimicked in lab experiments by adding polymers like dextran. In contrast, when RBCs are placed in simple saline solutions without these macromolecules, aggregation is greatly reduced [11, 15, 18, 20]. Figure 2.2 demonstrates a figure adapted from Brust et al. (2013) [19] showcasing RBCs in a (a) buffer solution versus in (b) dextran to promote aggregation and the rouleaux effect.

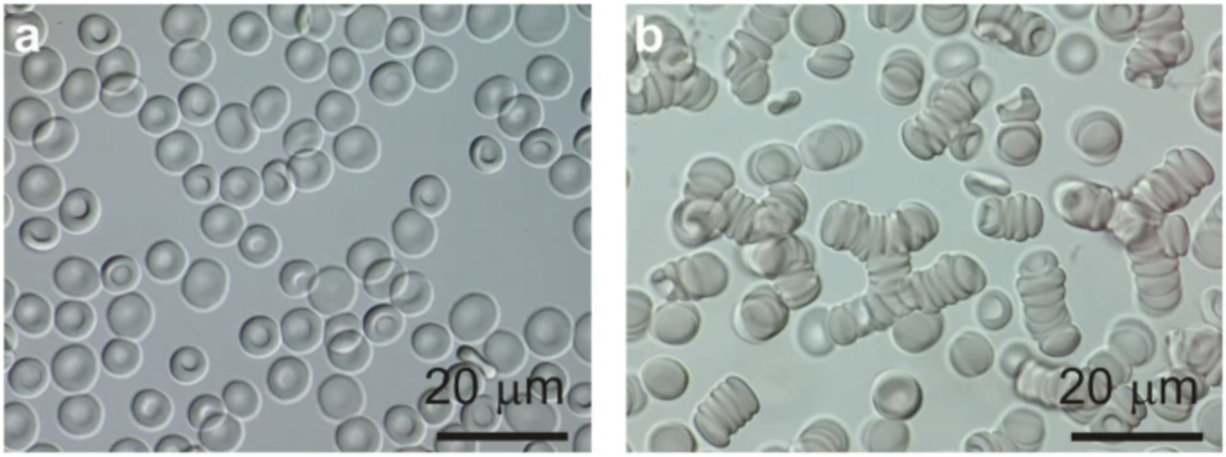

Figure 2.2: An image of single RBCs (a) in a buffer solution (b) in rouleaux in a 20 mg/ml dextran solution in a Petri dish. Reproduced from Brust et al. (2014).

2.4 Cell-Free Layer Formation

The CFL is a plasma-rich region near the walls of blood vessels where the concentration of RBCs is significantly reduced. The viscosity of fluid in the CFL region is similar to that of plasma, which is significantly lower than the effective viscosity in the tube center, where RBCs are concentrated. As a result, the CFL acts as a lubrication layer, facilitating the flow of the RBC core. The thickness of this layer directly influences blood flow resistance [4, 21]. Figure 2.3 illustrates blood flow in a microchannel, highlighting the velocity profile, shear rate distribution, and CFL formation. In an idealized Newtonian case under laminar conditions, velocity follows a Poiseuille (parabolic) profile, with maximum velocity at the center and zero at the walls due to the no-slip condition. However, blood is non-Newtonian, and RBCs influence viscosity and introduce shear-dependent effects, leading to deviations from this simplified profile, especially in high-Ht regions. The shear rate ($\dot{\gamma}$) quantifies how rapidly adjacent blood layers slide past one another and is highest near the vessel walls [17]. Wall shear stress or τ_w, is the tangential force per unit area exerted by a fluid on the inner surface of the vessel wall due to viscous forces [17].

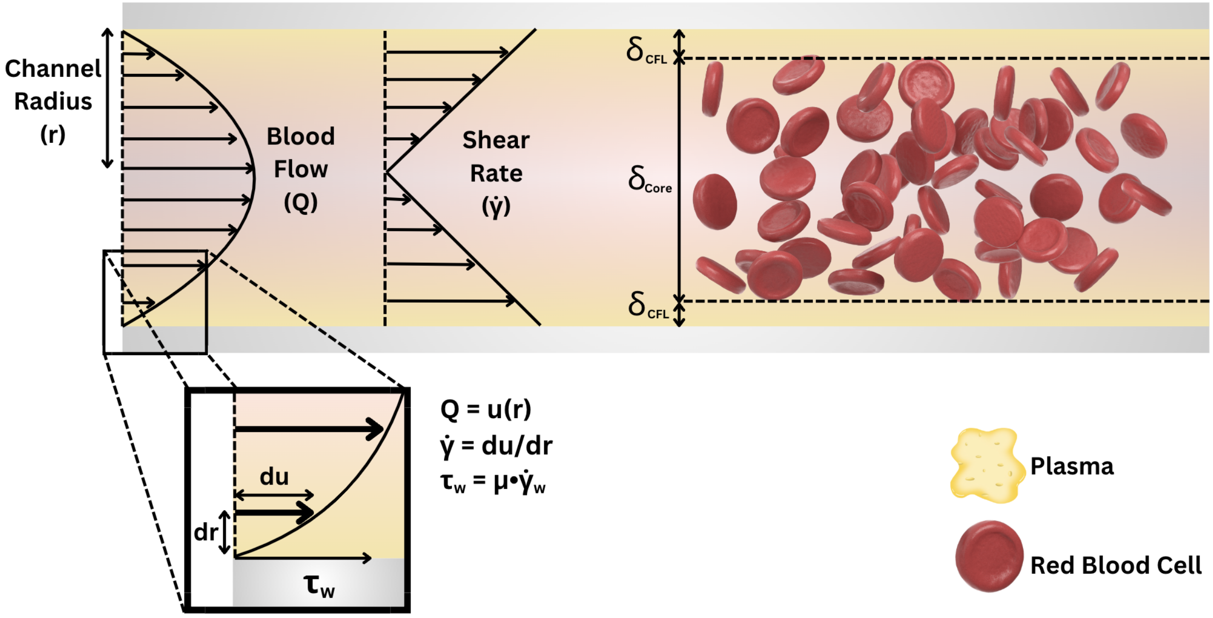

Figure 2.3: Schematic representation of blood flow in a microchannel, illustrating key hemodynamic parameters that contribute to CFL formation. In an idealized Newtonian case, the velocity profile follows a parabolic distribution, with maximum velocity at the center and zero at the walls due to the no-slip condition. Shear rate ($\dot{\gamma}$) is defined as the velocity gradient perpendicular to the flow direction, given by $\dot{\gamma} = \frac{du}{dr}$, where u is the velocity of blood flow and r is the radial position within the vessel. Wall shear stress is given by $\tau_w = \mu\dot{\gamma}_w$, where μ is the fluid viscosity and $\dot{\gamma}_w$ is the shear rate at the wall. The CFL, denoted as δ_{CFL}, is a plasma-rich region near the walls, while the RBC-rich core, δ_{Core}, forms at the center. Schematic created with Canva Pro.

The formation of the CFL are governed by a combination of *in vitro* and *in vivo* mechanisms. *In vitro* studies, including experimental and computational simulations, highlight the role of hydrodynamic lift forces, cell-cell interactions, and shear-induced RBC migration [4]. Hydrodynamic lift forces push cells away from the vessel walls [22, 23], while cell-to-cell interactions, such as inter-RBC collisions, play a role in RBC aggregation [24–26]. In contrast, *in vivo* investigations emphasize the role of the endothelial glycocalyx as a biochemical and physical barrier that further separates RBCs from the vessel wall. This dense polymeric layer, estimated to be 0.4–0.5 µm thick, plays a key role in CFL regulation and microvascular flow resistance [8, 27]. The following subsections first examine the more established theories of CFL governing factors, followed by emerging theories that explain this phenomenon.

2.4.1 Established Theories of CFL Influencing Factors

Over the past few decades, research has demonstrated that the thickness of the cell-free layer (CFL) is primarily influenced by vessel diameter (D), hematocrit (Ht), and shear rate ($\dot{\gamma}$). Early experimental and computational studies focused on characterizing how these parameters affect CFL formation, aiming to establish generalizable trends across different flow conditions. Table 2.1 summarizes the key findings, highlighting the effects of D, Ht, and $\dot{\gamma}$ on CFL formation. These studies focus primarily on using round microchannels and human blood, providing a suitable comparison to the experiments of this study. However, the literature remains divided on what impacts CFL behavior, with some studies attributing it primarily to vessel diameter through the well-known Fåhraeus–Lindqvist effect [5], while others suggest that Ht and shear forces play an equally, if not more, significant role

[7, 8].

1. Diameter Impact The Fåhræus–Lindqvist effect describes how blood viscosity decreases as vessel diameter decreases, due to RBC migration toward the center, leaving behind a plasma-rich CFL near the walls. This effect was first demonstrated by Fåhræus and Lindqvist (1931), who observed that CFL thickness increases as vessel diameter decreases, with blood viscosity in small microvessels (40 µm) approaching plasma viscosity [5].

Pries et al. (1992) further investigated this phenomenon, finding that in microchannels between 9–40 µm, CFL thickness increased with channel diameter. Figure 2.4 presents the relative apparent viscosity of blood as a function of tube diameter for different hematocrit levels, as reported by Pries et al. (1992) [8]. The data illustrate a biphasic trend: viscosity initially decreases in small vessels due to the Fåhræus-Lindqvist effect, where the presence of a CFL lowers viscosity. However, as vessel diameter increases, viscosity begins to rise while the CFL occupies a smaller fraction of the cross-section, reducing its ability to lower viscosity. In larger vessels, apparent viscosity eventually plateaus, suggesting that while blood remains a complex suspension, its viscosity becomes less sensitive to vessel diameter [8].

However, Katanov et al. (2015) challenged this biphasic trend in their simulations, reporting that CFL thickness increased with increasing vessel diameter in the range of 10–100 µm. This suggests that RBC redistribution within the vessel cross-section plays a significant role in CFL behavior, rather than vessel diameter alone [4]. These conflicting results highlight that CFL formation is influenced by additional interactions, such as RBC aggregation and wall-induced migration, rather than being solely dictated by vessel size.

2. Hematocrit Impact Another key determinant of CFL formation is Ht. Multiple studies confirm that higher Ht leads to a thinner CFL, as the increased RBC concentration reduces the plasma-rich region near the walls [7–9]. Figure 2.4, referenced earlier, also illustrates that these effects are Ht-dependent, with higher Ht levels leading to greater viscosity in all tube sizes. Moreover, Reinke et al. (1986) [28] found that RBC migration to the tube center is a result from aggregation of cells at low shear rates. Therefore, the CFL must also decrease with increasing hematocrit. Vessel geometry also has been shown to have an influence when Cerdeira et al. (2009) found that as Ht increases, the reduction in CFL thickness is more significant in circular microchannels than in rectangular ones [29]. Maeda et al. (1996) provided additional *in vivo* evidence, showing that as Ht increases, the reduction in CFL thickness is more pronounced in elastic (compliant) vessels compared to stiffened (rigid) vessels [30]. In summary, it is safe to say that Ht is a key determinant of CFL thickness. Extensive research has consistently demonstrated a clear trend: as Ht increases, CFL thickness decreases.

3. Shear Rate Impact The role of shear rate ($\dot{\gamma}$) in CFL formation is still debated, with conflicting findings across studies. Some experiments suggest that higher $\dot{\gamma}$ reduces CFL thickness, as RBCs are forced closer to the vessel walls [2]. Fedosov et al. (2010) [2] examined the relationship between shear rate and CFL in simulated microvessels, using mean shear rate ($\dot{\gamma} = \bar{v}/D$) as a measure, where $\bar{v}$ is the mean flow velocity and D is the tube diameter. The results show that CFL thickness decreases slightly with increasing shear

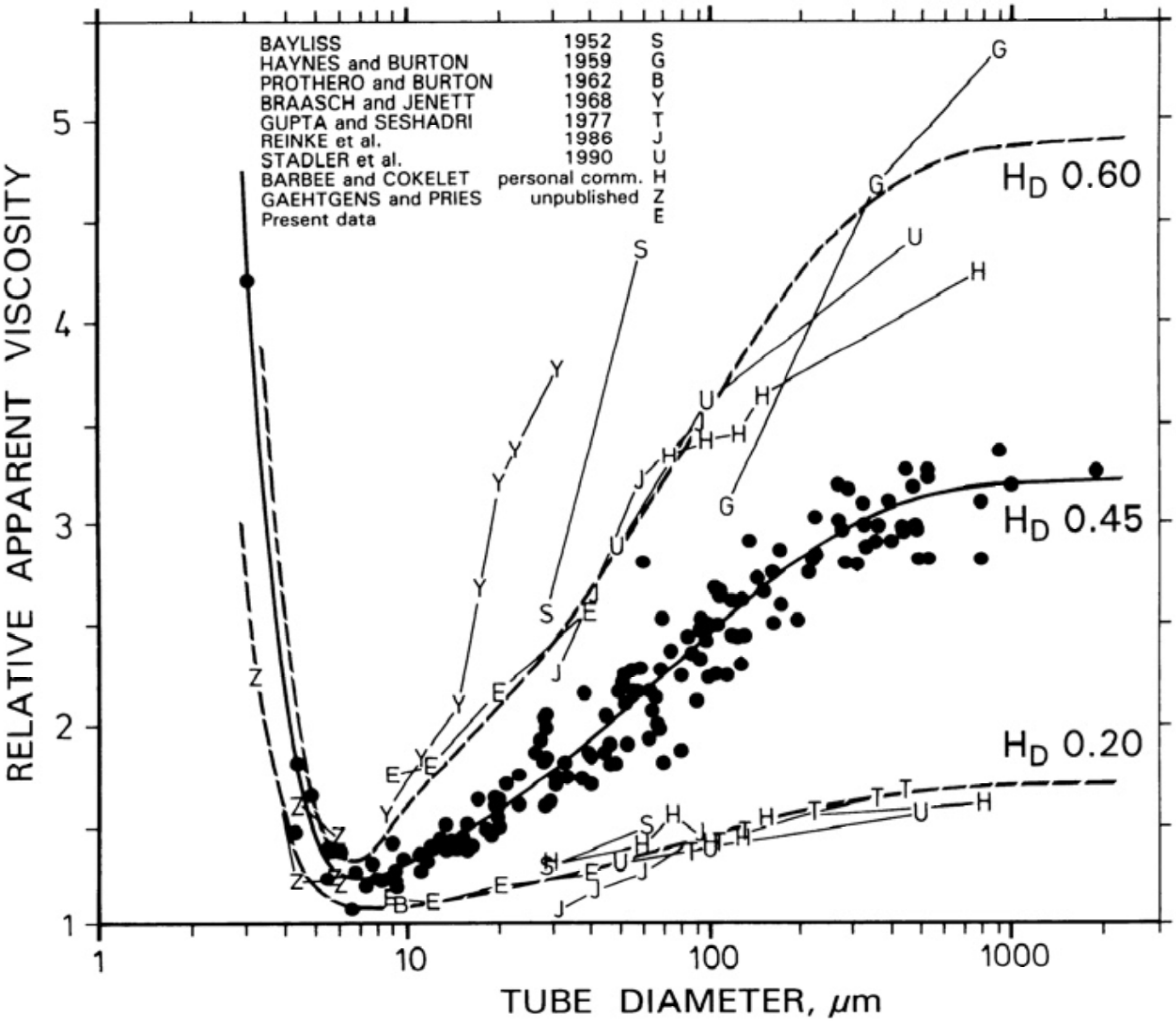

Figure 2.4: Relative apparent viscosity of blood as a function of tube diameter for different Hts ($H_D = 0.20, 0.45, 0.60$) from Pries et al. (1992) [8]. The data highlights how viscosity decreases in small tubes before increasing again at capillary scales (<7 µm). Experimental data from previous studies are overlaid, showing agreement with theoretical predictions.

rate or, equivalently, flow rate. This is attributed to intensified hydrodynamic interactions among RBCs, which expand the RBC core [2]. However, Bugliarello and Sevilla (1970) found no direct correlation between CFL and shear rate, concluding that shear effects are inconsistent across different vessel sizes [9]. In contrast, Katanov et al. (2015) used a pseudo-shear rate definition, given by $\dot{\gamma} = Q/(R^2 D)$, and observed a positive relationship between shear rate and CFL thickness. Higher $\dot{\gamma}$ lead to a thicker CFL, contradicting prior experimental findings [4]. Maeda et al. (1996) [30] estimated shear rate using a wall shear rate approximation based on Poiseuille flow assumptions. This *in vivo* study further complicates our understanding, showing that CFL increases with shear rate, but more significantly in elastic microvessels than in stiffened ones. They observed that hardened microvessels exhibited a significantly thinner CFL and higher flow resistance ($1.38\times$) than elastic microvessels, reinforcing the role of vessel compliance in microcirculatory flow [30].

Although numerous studies have explored the influence of shear rate over the years, no clear consensus has emerged. This underscores the importance of conducting experiments with precisely controlled channel sizes, Ht levels, and flow conditions to better understand its role in CFL formation. Additionally, direct measurement of local shear rate, rather than relying on bulk or pseudo-shear rate estimations, is crucial for accurately capturing the microscale dynamics of CFL behavior.

Table 2.1: Summary of literature on governing factors of cell-free layer (δ) formation

Reference	**Study Type**	**Microchannel Type, Dimensions (μm)**	**Blood Type, Hematocrit**	**Diameter (D) Impact on δ**	**Hematocrit (Ht) Impact on δ**	**Shear Rate ($\dot{\gamma}$) Impact on δ**
Fåhraeus & Lindqvist (1931)	*in vitro*	Circular, 3–1000	Human blood	$D\downarrow$, $\delta\uparrow$	Ht $\uparrow$, $\delta\downarrow$, viscosity $\uparrow$	Not measured
Pries et al. (1992)	*in vitro*	Circular Glass Capillary, 9–40	Human blood, 5–89%	$D\uparrow$, $\delta\uparrow$	Ht $\uparrow$, $\delta\downarrow$	Not measured
Reinke et al. (1986)	*in vitro*	Cylindrical, 29–94	Human blood, 45%	$D\downarrow$, $\delta\uparrow$	Ht $\uparrow$, $\delta\downarrow$	Not measured; Suggests $\dot{\gamma}\uparrow$, $\delta\downarrow$
Bugliarello & Sevilla (1970)	*in vitro*	Circular Glass Capillary, 40–70	Human blood, 5-40%	$D\downarrow$, $\delta\uparrow$	Ht $\uparrow$, $\delta\downarrow$ (Fåhraeus effect)	Not directly dependent; high $\dot{\gamma}$ stabilizes δ
Cerdeira et al. (2009)	*in vitro*	Circular PDMS, 73±2	Human blood, 3–37%	δ larger in circular than rectangular channels	Ht $\uparrow$, $\delta\downarrow$ (4× reduction from 3% to 37%)	Not measured
Fedosov et al. (2010)	Simulation	Circular, 10–40	Simulated, 15–45%	$D\downarrow$, $\delta\uparrow$	Ht $\uparrow$, $\delta\downarrow$	$\dot{\gamma}\uparrow$, $\delta\downarrow$
Katanov et al. (2015)	Simulation	Cylindrical, 10–100	Simulated, 15–45%	$D\uparrow$, $\delta\uparrow$	Ht $\uparrow$, $\delta\downarrow$	$\dot{\gamma}\uparrow$, $\delta\uparrow$
Maeda et al. (1996)	In vivo	Rabbit mesentery, 10–40	Human blood, 16%	$D\uparrow$, $\delta\uparrow$	Ht $\uparrow$, $\delta\downarrow$ (stronger effect in elastic vessels)	$\dot{\gamma}\uparrow$, $\delta\uparrow$ (greater in elastic than hardened vessels)

2.4.2 Emerging Theories of CFL Influencing Factors

Building upon these well-established theories, more complicated models have emerged, incorporating additional physical forces and interactions that refine our understanding of CFL behavior. Recent studies suggest that cell-wall interactions, cell-cell interactions, and shear rate gradients play significant roles in RBC migration, operating alongside vessel diameter and Ht effects. Together, these new perspectives build upon early models, providing a more comprehensive view of CFL formation that accounts for these interactions between RBCs.

1. Cell-wall Forces Cell-wall, RBC-wall, or Hydrodynamic lift forces arise due to asymmetric flow stress distributions, pushing RBCs away from vessel walls and toward the vessel core. This effect is particularly pronounced in microvascular environments, where confinement enhances RBC-wall proximity. Coupier et al. [23] investigated the role of hydrodynamic lift forces in RBC migration using mesoscopic simulations. They demonstrated that highly deformable RBCs migrate efficiently toward the vessel core, promoting a clearly defined CFL. Conversely, rigid RBCs, such as those associated with sickle cell disease or diabetes, show impaired migration and diminished CFL formation. Furthermore, the endothelial glycocalyx, a polymeric layer lining vessel walls, modulates these lift forces significantly. It acts as a hydrodynamic barrier, buffering RBC-wall interactions and reinforcing the CFL [21].

2. Cell-Cell Interactions and Shear-Induced Diffusion The formation of the CFL is governed by the interplay between cell-wall interactions, cell-cell interactions, and shear-induced diffusion, with factors such as hematocrit, shear rate, and vessel size influencing which mechanism dominates [24]. As RBCs migrate away from the walls, they experience frequent cell-cell collisions that cause lateral dispersion, a process known as shear-induced diffusion. At higher hematocrits, increased cell-cell interactions lead to more frequent RBC collisions. In contrast, at lower hematocrits, RBC-wall interactions become more dominant as there are fewer cell-cell collisions to redistribute RBCs [25]. Shear rate also plays a critical role, as higher shear rates increase shear-induced diffusion, further disrupting RBC aggregation and influencing CFL thickness. Vessel size modulates these effects, with smaller vessels enhancing RBC-wall interactions due to geometric confinement, while larger vessels allow for greater shear-induced dispersion. Thus, CFL formation depends on the relative contributions of these forces, which shift depending on flow conditions, hematocrit, and vessel diameter [24, 31]. Figure 2.5 illustrates this force balance, highlighting cell-wall interactions (cw) and cell-cell interactions (cc).

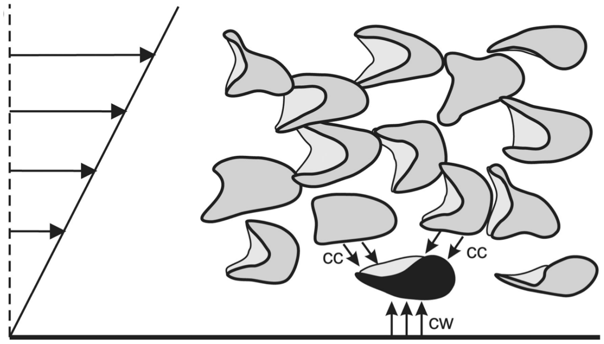

Figure 2.5: Schematic diagram of the force balance between cell-cell (cc) and cell-wall (cw) interactions. Reproduced from [31].

3. Gradient of Shear Rate Shear-induced diffusion, as described in the previous section, is closely linked to the gradient of shear rate ($\nabla\dot{\gamma}$), which quantifies spatial variations in shear stress within the vessel. RBC collisions, driven by these local shear gradients, contribute to their redistribution and ultimately influence CFL formation. Unlike bulk shear rate, which describes the overall deformation rate of the fluid, $\nabla\dot{\gamma}$ captures localized variations that further regulate RBC migration. Shear-induced migration, first described by Leighton and Acrivos (1987) [26], explains how particles in suspensions move from regions of high shear gradients to areas of lower shear stress. This movement, resulting from irreversible cell-to-cell interactions and diffusive migration, has been shown to significantly impact local viscosity and phase separation, both of which contribute to the CFL. Recent advances have extended these concepts to non-Brownian suspensions, highlighting the critical roles of solid effective stress and fluid-particle interactions [32]. Numerical simulations of microvascular flows consistently suggest that regions with pronounced shear rate gradients strongly promote RBC migration toward vessel cores. These simulations underline that RBC displacement relies on local shear rate variations [33]. Experimental evidence from colloidal suspensions further confirms that spatial variations in shear rate significantly affect particle migration, especially within complex geometries or constricted channels [34]. However, these critical insights have predominantly emerged from non-biological suspensions, and direct experimental validation using blood in circular microchannels remains limited. This represents a significant gap in the literature.

2.5 Blood Flow Modeling in Microcirculation

Accurately modeling blood flow in microcirculation is essential due to its non-Newtonian behavior, where viscosity varies with shear rate. Various models have been proposed to describe blood rheology, ranging from simple Newtonian approximations to more complex non-Newtonian formulations. The following subsections discuss key models used in blood flow analysis, highlighting their strengths and limitations.

2.5.1 NEWTONIAN MODEL

The Newtonian Model assumes a *constant viscosity*, meaning that the fluid's resistance to flow does not change with shear rate. This leads to a *linear relationship* between shear stress and shear rate. For a Newtonian fluid flowing through a cylindrical vessel, the velocity profile follows a parabolic distribution [17]:

$$u(r) = \frac{\Delta P}{4\mu L}\left(R^2 - r^2\right), \tag{2.2}$$

where:

- ΔP is the pressure drop along the length of the vessel,
- μ is the constant viscosity of the fluid,
- L is the vessel length,
- R is the vessel radius,
- r is the radial position from the center of the vessel.

The corresponding shear rate, which quantifies the velocity gradient perpendicular to flow, is given by:

$$\dot{\gamma}(r) = -\frac{\Delta P}{2\mu L}r. \tag{2.3}$$

This equation shows that the shear rate varies linearly with the radial position, reaching its maximum at the vessel wall ($r = R$) and decreasing to zero at the centerline ($r = 0$).

Although the Newtonian Model is widely used in large arteries where shear rates are relatively high and blood behaves approximately Newtonian, it fails to accurately describe microcirculatory flow. Blood is a shear-thinning fluid, meaning its viscosity decreases with increasing shear rate [17]. In microvessels, where shear rates vary significantly, the assumption of constant viscosity results in:

- **Overestimation of viscosity** at high shear rates, where blood flows more easily.
- **Underestimation of viscosity at low shear rates**, where RBC aggregation increases resistance.
- **Neglecting CFL formation**, which significantly influences flow resistance and RBC distribution [17].

Because of these limitations, more advanced non-Newtonian models are required to accurately capture blood's rheological properties in microcirculation.

2.5.2 Power Law Model

To address the limitations of the Newtonian Model, the Power Law Model accounts for *shear-dependent viscosity*, making it particularly useful for modeling shear-thinning fluids like blood [17]. The Power Law Model defines the relationship between shear stress and shear rate as:

$$\tau = K_p \dot{\gamma}^{n_p}, \tag{2.4}$$

where:

- K_p is the *consistency index*, representing the core viscosity,
- n_p is the *flow behavior index*, which characterizes the degree of shear-thinning.

For a Power Law fluid flowing through a cylindrical vessel, the velocity profile is given by:

$$u(r) = \left(\frac{\Delta P}{2K_p L} \right)^{\frac{1}{n_p}} \cdot \frac{n_p}{n_p + 1} \left(R^{\frac{n_p+1}{n_p}} - r^{\frac{n_p+1}{n_p}} \right), \tag{2.5}$$

where:

- ΔP is the pressure drop along the vessel,
- L is the vessel length,
- R is the vessel radius,
- r is the radial position.

The corresponding shear rate is:

$$\dot{\gamma}(r) = - \left(\frac{\Delta P}{2K_p L} \right)^{\frac{1}{n_p}} r^{\frac{1}{n_p}}. \tag{2.6}$$

The Power Law Model effectively captures blood's *shear-thinning behavior* at moderate shear rates, where blood viscosity decreases as shear rate increases. However, it has several limitations:

- **Fails at extreme shear rates:** The model does not account for the viscosity plateau observed at low shear rates, where RBC aggregation increases viscosity, or at high shear rates, where the minimum viscosity is reached.
- **Cannot model CFL effects:** The model does not distinguish between the *cell-rich core* (non-Newtonian) and the *plasma-rich CFL* (Newtonian), making it less accurate in microcirculatory conditions.

Despite these limitations, the Power Law Model remains a widely used non-Newtonian model due to its simplicity and effectiveness in capturing shear-thinning behavior in large and medium-sized vessels. However, for accurate modeling of microcirculatory blood flow, more advanced models, such as the Carreau Model, are often preferred [17].

2.5.3 Carreau Model

The *Carreau Model* refines the Power Law Model by accounting for viscosity variations over a *wider range of shear rates*, asymptotically approaching constant values at both low and high shear rates. This makes it particularly effective in modeling blood's non-Newtonian behavior across different flow conditions [17].

The viscosity function is given by:

$$\mu_c(\dot{\gamma}) = \mu_\infty + (\mu_0 - \mu_\infty) \left[1 + (\lambda_c \dot{\gamma})^2\right]^{(n_c-1)/2}, \tag{2.7}$$

where:

- μ_0 is the viscosity at zero shear rate (low flow conditions),
- μ_∞ is the viscosity at infinite shear rate (high flow conditions),
- λ_c is a time constant, representing the transition between low and high shear rate behaviors,
- n_c is the flow behavior index, controlling the degree of shear-thinning.

The corresponding shear stress for a Carreau fluid is expressed as:

$$\tau = \mu(\dot{\gamma}) \cdot \dot{\gamma} \tag{2.8}$$

Unlike the Power Law Model, the Carreau Model correctly predicts viscosity plateaus at both low and high shear rates, accurately reflecting blood's behavior across all flow conditions. At low shear rates, blood behaves more like a Newtonian fluid, while at high shear rates, it follows a shear-thinning behavior. The Carreau Model provides a continuous function that smoothly transitions between these two regimes. However, despite its advantages, the Carreau Model has some limitations [17]:

- **Lacks explicit microstructural interpretation:** While the Carreau Model effectively captures shear-thinning behavior, it does not explicitly account for underlying RBC dynamics such as aggregation or deformation.
- **Does not explicitly model the CFL:** While the model accurately captures viscosity variations, it does not account for the presence of a CFL near the vessel walls.

Despite these limitations, the Carreau Model remains one of the most widely used non-Newtonian models for blood flow, offering a good balance between accuracy and computational efficiency.

2.5.4 DOUBLE-PARAMETER POWER FIT

To improve velocity profiling in microcirculatory flow, a double-parameter power (DPP) Fit was introduced by Koutsiaris et al. (2009) [35]. Unlike traditional rheological models that derive velocity from fluid properties such as viscosity, this approach is a purely empirical fitting model designed to match experimentally observed velocity distributions.

This model introduces two shape factors:

- k_1 – Controls the bluntness of the RBC-rich core velocity profile.
- k_2 – Determines the steepness of the shear gradient near the vessel wall.

The velocity profile is expressed as:

$$u(r) = u_{\max}\left(1 - k_1\left(\frac{r}{R}\right)^2\right)\left(1 - \left(\frac{r}{R}\right)^{k_2}\right), \tag{2.9}$$

where:

- u_{max} is the maximum velocity at the vessel center,
- R is the vessel radius,

- r is the radial position from the vessel center.

The corresponding shear rate, which represents the velocity gradient perpendicular to flow, is given by:

$$\dot{\gamma}(r) = \left|\frac{du}{dr}\right| = \left|\frac{u_{\max}}{R}\left(-2k_1\frac{r}{R}\left[1-\left(\frac{r}{R}\right)^{k_2}\right] - k_2\left(\frac{r}{R}\right)^{k_2-1}\left[1-k_1\left(\frac{r}{R}\right)^{2}\right]\right)\right| \tag{2.10}$$

Unlike traditional non-Newtonian models, this model does not attempt to extract rheological properties such as viscosity. Instead, it is designed to provide an accurate empirical fit to measured velocity profiles. By adjusting k_1 and k_2, the model can match a wide range of experimental velocity profiles. This approach better represents velocity differences in the cell-rich core and near the CFL. However, there are notable limitations:

- **Lacks direct physical interpretation:** Since the model does not rely on viscosity or other rheological properties, it does not provide insights into blood's microstructural behavior.
- **Limited applicability to varying physiological conditions:** The shape factors k_1 and k_2 must be determined experimentally for each case, limiting its predictive capability outside known datasets.
- **Does not explicitly model the CFL thickness:** While the model captures velocity variation near the CFL, it does not incorporate CFL thickness explicitly.

Despite these limitations, the DPP Fit is a valuable tool for microvascular flow analysis, particularly when experimental velocity profiles are available. It provides an efficient alternative for modeling RBC distribution in vessels where classical models fail to capture well-fitted velocity profile [15, 35].

2.5.5 Comparing Models with Blood Viscosity and Shear Rate

Figure 2.6 presents a log-log plot of the predicted viscosity of blood as a function of shear rate, comparing three commonly used rheological models: the Carreau model, the Power Law model, and the Newtonian approximation, as reported by Fenech et al. (2018) [17]. The Carreau model provides a smooth transition between the Newtonian plateau at low shear rates and the shear-thinning behavior at high shear rates. The Power Law model, although simpler, captures the shear-thinning trend but lacks a Newtonian plateau at low shear rates. In contrast, the Newtonian model assumes a constant viscosity ($\mu = 0.0035$ Pa.s), which does not account for the shear-dependent nature of blood flow. This comparison highlights how the choice of model impacts the predicted flow behavior, particularly in microcirculatory applications where shear rates vary widely [17].

2.6 Conclusion

The existing literature provides valuable insights into CFL formation, yet significant knowledge gaps persist, particularly regarding the precise influence of vessel diameter, Ht, and

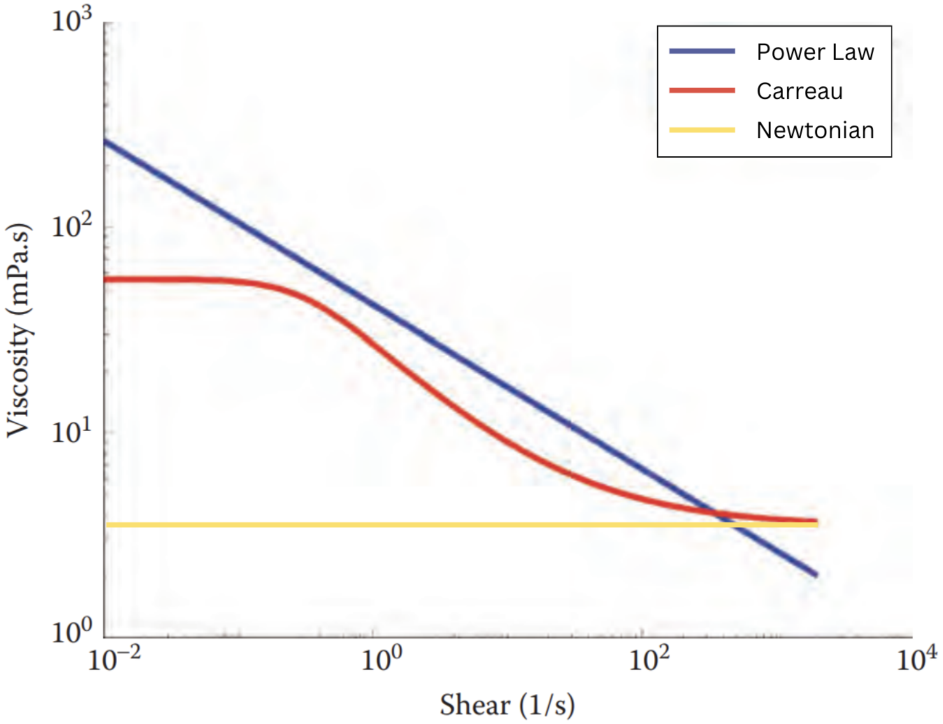

Figure 2.6: Log-log plot of predicted viscosity of blood by Carreau ($\mu_\infty = 0.0035$ Pa.s, $\mu_0 = 0.056$ Pa.s, $\lambda = 3.313$ s, and $n = 0.3568$ at shear rate 400 1/s [36]), Power Law Model ($K = 0.042$ Pa.s^n and $n = 0.6$), and Newtonian Model ($\mu = 0.0035$, as a function of the shear rate. Adapted from [17].

shear rate gradients on CFL dynamics. While numerous studies have examined RBC migration and shear-induced diffusion, inconsistencies remain due to variations in experimental methodologies and modeling approaches. We hypothesize that the gradient of shear rate plays a critical role in regulating RBC migration within microvascular flows by interacting with hydrodynamic lift forces and shear-induced diffusion. To address these gaps, this study will systematically characterize the local velocity profile in capillary microchannels of varying diameters, flow rates, suspension mediums, and Ht levels, providing a controlled framework to assess their impact on CFL formation. Current blood flow models struggle to accurately capture the transition from Newtonian to non-Newtonian behavior. Therefore, a key objective of this study is to develop and validate a theoretical framework that more precisely represents CFL dynamics under physiological conditions. Ultimately, this work aims to identify the primary mechanisms governing CFL formation, resolving contradictions in the literature and advancing the accuracy of microvascular flow modeling.

Chapter 3

Methodology and Materials

This chapter presents the methodology and materials used to model and investigate CFL characteristics within microchannels. Using a high-speed camera (HSC), micro-particle image velocimetry (µPIV), and precision flow control, this study uses advanced instrumentation to analyze velocity fields under controlled conditions. Details on microchannel fabrication, fluid preparation, experimental setups, and mathematical analysis of velocity profiles are provided to ensure a comprehensive understanding of the experimental approach.

3.1 Microchannel Fabrication

The microchannel fabrication method is developed by Chartrand et al. (2023) [37]. Round borosilicate glass capillaries (VitroCom, MA, USA) with inner diameters of 25 µm and 50 µm are chosen to simulate microvessels. Glass is chosen to eliminate the influence of vessel compliance, ensuring that flow and pressure measurements reflect only the properties of blood. Each capillary, initially 30 cm in length, is cut into 3.5 cm sections using a Dremel tool and a diamond bit attachment. The outer diameter (OD) of the glass channels is 3 mm. These channels are mounted on 1 mm-thick glass slides using UV-cured Norland Optical Adhesive 81 (Norland Products Inc., NJ, USA), with curing completed under the IntelliRay 6000 Shuttered UV Floodlight (Uvitron International, MA, USA) at 50% for 30 seconds. Due to the large OD of the channels, significant light refraction occurs as the laser passes through, hindering clear imaging with the µPIV system. Since borosilicate glass has a refractive index of 1.473, the channels are submerged in a 99% glycerol pool with a refractive index of 1.4716. This immersion made the outer glass nearly invisible and left only the inner channel visible, reducing light refraction and enhancing image clarity with the µPIV system. This invisibly effect due to glycerol submersion on can be seen in Figure 3.1. To contain the glycerol around the microchannel and prevent spills, an enclosure, designed by [37], is created using SolidWorks and 3D-printed using the Elegoo Mars 2 Mono LCD MSLA 3D Printer (Elegoo, Shenzhen, China) with plant-based UV transparent resin. The enclosure had four walls, each with 3.2 mm diameter holes for the glass capillary, ensuring a tight fit to prevent leaks. The enclosure is mounted on a glass slide with optical glue. After pouring glycerol into the enclosure to the brim, a 22 x 22 mm glass cover slip (Fisher Scientific, MA, USA) is gently slid over the enclosure's top, minimizing air bubble formation. Optical glue is applied once more to seal the joints between the cover slip and enclosure, securing the assembly and preventing leaks, as shown in Figure 3.2. Lastly, to improve bio-compatibility, a PLL-PEG solution is injected into each channel and left for at least one hour. Afterward, the channels are rinsed with deionized water (DI), leaving a PLL-PEG coating to prevent RBCs to the glass surface

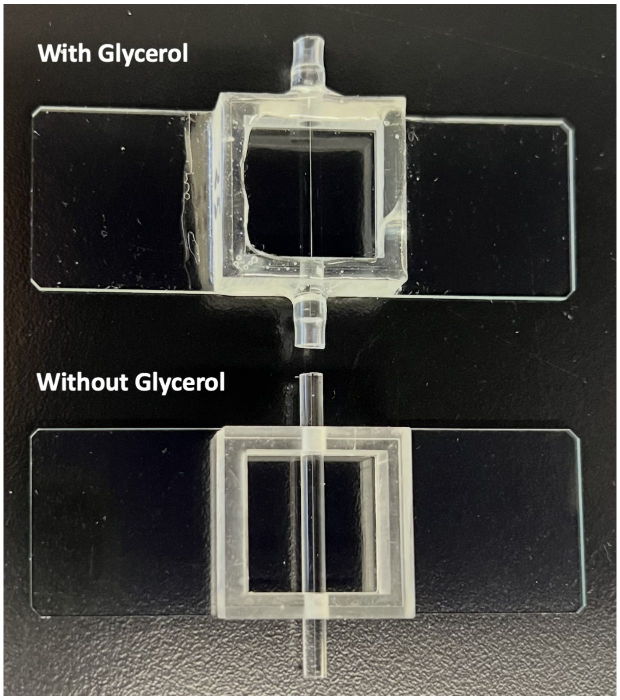

Figure 3.1: Fabricated Microchannel with glycerol (top) and without Glycerol (bottom) submersion of glass capillary.

[37].

3.2 Fluid Preparation

For the study, fresh blood samples are collected and prepared to complete measurements. Human blood is collected from healthy individuals with approval of the ethics committee at the University of Ottawa (Ethics File No. H-03-19-3441) and is collected at the Dynacare Laboratory and Health Services Centre with the help of accredited professionals. The blood sample is collected using 4 mL tubes which are coated with ethylenediaminetetraacetic acid

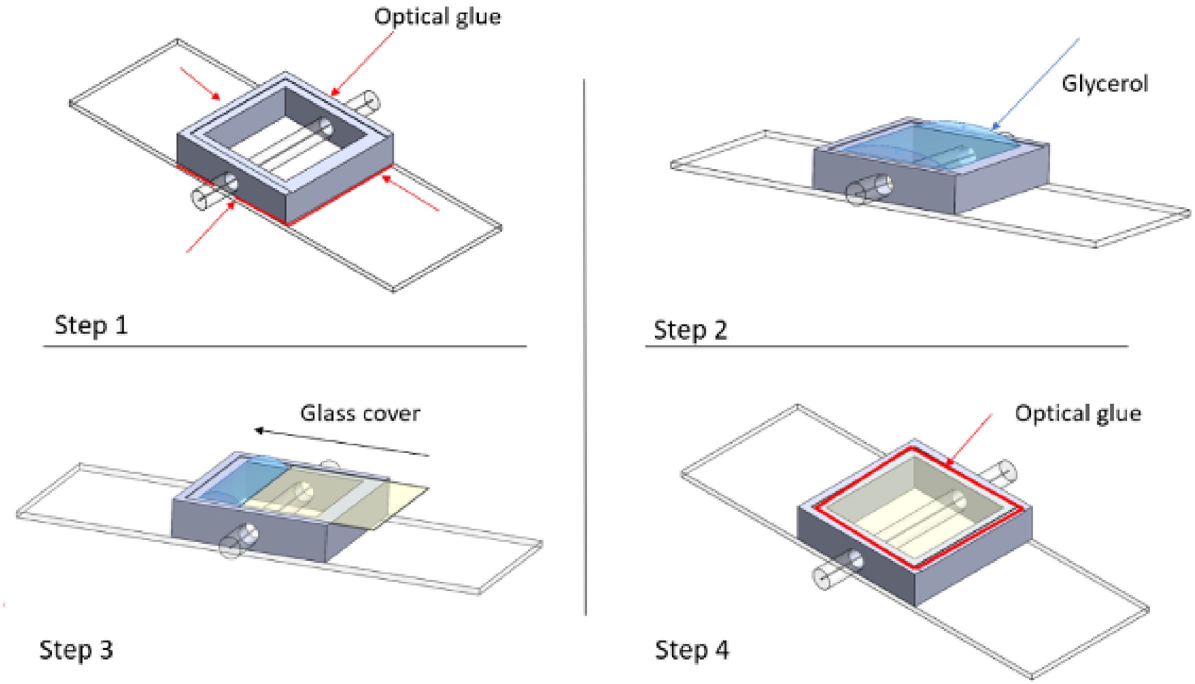

Figure 3.2: Assembly steps for mounting the components onto a glass slide: (1) Position the 3D-printed enclosure on the glass slide and secure it with optical glue. (2) Fill the enclosure with glycerol until it is nearly overflowing. (3) Carefully slide a glass cover over the top of the enclosure. (4) Apply optical glue once more to secure the glass cover in place. Reproduced from [37].

(EDTA) to prevent coagulation of the whole blood during transportation. The typical total collection volume is approximately 12 ml per individual donation, and this is to ensure that there is enough sample to complete a full experiment and therefore reduce variations of measurements due to variability between blood donors. Various fluid suspensions are prepared to investigate aggregation effects, consisting of healthy human blood with Ht levels adjusted to 5%, 10%, 15%, and 20%.

3.2.1 PBS Suspension

Initial measurements are conducted using RBCs suspended in phosphate buffered saline (PBS) to prevent aggregation. Blood samples are collected and centrifuged at 500 xg for 10 minutes. This initial centrifugation separates the buffy coat (containing WBCs and platelets) and plasma from the RBCs, both of which are discarded. Removing the buffy coat helps prevent coagulation, while plasma removal minimizes cell aggregation. Before the second and third centrifugation, filtered PBS (0.2 µm, Nylon, Non-Sterile, Fisher Scientific, Ireland) is added to the RBCs, followed by gentle agitation to re-suspend the cells and ensure thorough removal of any residual WBCs, platelets, or plasma.

After the final wash, the PBS is removed, leaving isolated RBCs ready to be re-suspended in PBS at specific Ht levels (5% to 20%). To stabilize the suspension and prevent sedimentation, the saline solution is prepared with 31.5% Iodixanol (OptiPrep®) (Sigma Aldrich, Ref. D1556) and 68.5% PBS, along with 0.9 mg of glucose per mL of PBS solution. Glucose serves as an energy source to support RBC metabolic activity and viability, reducing the risk of degradation or lysis *in vitro* [38]. OptiPrep® acts as a density stabilizer, reducing sedimentation of RBCs by balancing the density difference between the cells and suspending fluid [39].

3.2.2 Plasma Suspension

To investigate RBC aggregation, experiments are conducted with RBCs re-suspended in their native plasma. Initially, blood samples are centrifuged to separate and remove the plasma and buffy coat, followed by three PBS washes. The first centrifugation is performed at 700 xg for 10 minutes to maximize plasma extraction, while subsequent spins are done at 500 xg for 10 minutes. The extracted plasma is stored, and its density is modified by adding 315 µL of dried OptiPrep® per mL of plasma. OptiPrep® is dried in a plastic container at 60°C for 2 days, then cooled to room temperature and thoroughly mixed with the plasma by shaking for 1 hour. The RBCs are then suspended in this adjusted plasma to achieve the target Ht levels.

3.2.3 Fluorescent Tracer Particles

The fluorescent tracer particles (FluoroMax, Thermo Scientific, MA, USA), essential for µPIV measurements, have a particle diameter of 0.87 µm and a density of 1.06 g/cm^3. To enable µPIV analysis, specific amounts of fluorescent tracer particles are added to both PBS- and plasma-suspended RBC samples. For samples with 5% and 10% Ht, 30 µL/mL of particles were added; for 15% Ht, 45 µL/mL; and for 20% Ht, 60 µL/mL. Increasing particle concentration at higher Ht levels is necessary to maintain clear visibility in µPIV imaging, as denser RBC suspensions can obscure particle detection.

3.2.4 Hematocrit Verification

To verify and adjust Ht levels before experimentation, we first perform an initial validation using the CritSpin Micro-Hematocrit Centrifuge and Crit Spin test tubes (CritSpin, Thermo Fisher Scientific Inc., China). A portion of the blood sample, prepared in a saline (PBS) solution, is loaded into the test tubes and centrifuged. After centrifugation, the packed cell volume (PCV) is measured to determine the initial Ht level. If the measured Ht was within the desired range, the same RBC-to-PBS proportion is used to prepare the final solution. However, if the Ht is too low (e.g., 80% PCV instead of 100%), the ratio of RBCs to PBS is adjusted accordingly to achieve the target concentration. The final solution is prepared by carefully mixing RBCs and PBS in controlled ratios; for example, to create a 1 mL solution with a 5% Ht, 50 µL of packed RBCs is combined with 950 µL of PBS. The adjusted sample is not centrifuged again, as the appropriate ratio is determined from the initial validation. This process ensures accurate Ht levels before proceeding with further experiments. It is important to note that OptiPrep should not be used in the CritSpin centrifuge, as its high density and viscosity may interfere with centrifugation, leading to inaccurate readings or potential damage to the equipment.

Figure 3.3: Crit Spin micro-hematocrit tubes displaying red blood cell suspensions at various hematocrit (Ht) levels for validation. From top to bottom, the tubes represent 5%, 10%, 15%, and 20% Ht. The packed cell volume in each tube confirms the accuracy of the prepared Ht concentrations for subsequent experiments.

3.3 EXPERIMENTAL SETUP AND MEASUREMENTS

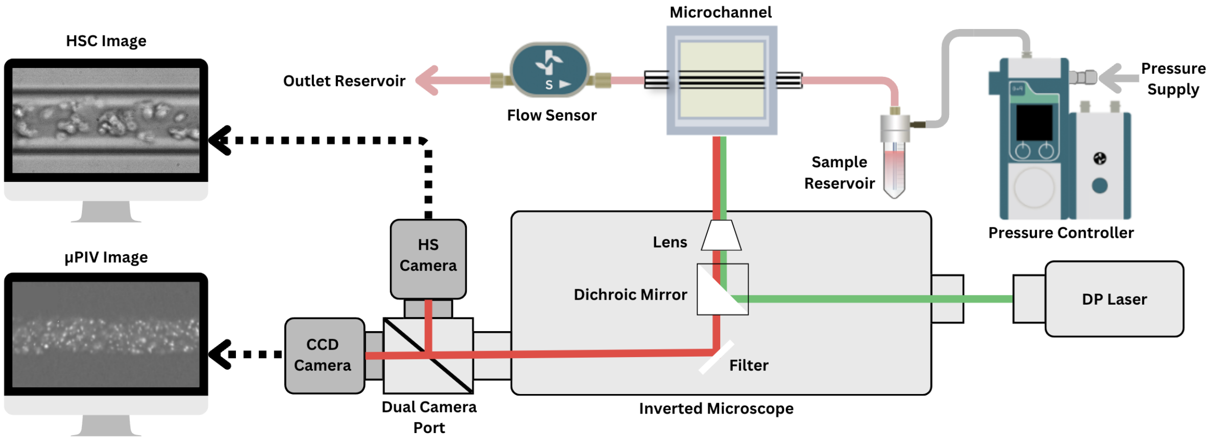

Figure 3.4: Schematic of the experimental setup for simultaneous measurement of velocity profiles and cell-free layer (CFL) thickness. A pressure-driven flow system regulates flow through a microchannel using a pressure controller and flow sensor. CFL images are captured with a high-speed camera (HSC) using a 20x objective, while velocity fields are obtained using a micro-particle image velocimetry (μPIV) system with Charged Couple Device (CCD). A dual-camera port and filter cube direct light appropriately between the μPIV and HSC pathways. System control and synchronization are managed via LabView and OxyGEN software. Schematic created using Canva Pro.

The experimental setup, shown in Figure 3.4, outlines the μPIV system (LaVision Flow-Master MITAS) for capturing velocity profiles and a HSC for CFL image acquisition. To allow fluid to flow through the microchannel, a pressure-driven flow system, Flow EZ pressure controller (Fluigent, France), is used. It is connected to a Flow Unit sensor, model S (Fluigent, France) to precisely regulate and monitor the flow rate. The Flow EZ pressure controller with the pressure link allows the system to precisely modulate the flow rate by adjusting the applied pressure. To manage and fine-tune the pressure settings, the Fluigent OxyGEN software (Fluigent, France) is used. This software provides an intuitive interface for setting, monitoring, and adjusting the pressure applied by the Flow EZ controller in real time. During the experiment, the OxyGEN software logs the pressure and flow rate data. This data is recorded in real time and exported as .csv files. Tubing connects the Flow EZ pressure controller (Fluigent, France) to the sample reservoir, which induces fluid flow into the microchannel. The sample fluid is placed in an airtight metal tube cap for microfluidics, specifically the P-CAP (Fluident, France), which is designed for pressurizing standard laboratory vials, including 1.5 mL and 2 mL Eppendorf tubes (Eppendorf, Germany). These metal tube caps provide a secure, leak-proof seal that allows the vials to be pressurized without risk of sample loss or contamination.

To capture images of the RBC inside the channel for our CFL measurement, the HSC uses a 20x objective lens (LD Plan-Neofluar, Zeiss, Germany). For each flow rate setting, the high-speed camera captures a set of 200 .png images, with each image measuring 2040 pixels by 1080 pixels in dimension. The HSC is controlled using a LabView software (National Instruments, USA) developed by Erfan Niazi. For each flow rate, 200 images are taken at a rate of approximately 100 fps and with a 0.1 ms exposure time.

Simultaneously to each HSC acquisition, velocity profiles are obtained from the µPIV system that consists of an inverted MITAS fluorescent microscope (LaVision Gmbh, Germany). The images are taken using a charged coupled device (CCD) camera (LaVision, Germany) with a Nd: YAG laser source (New Wave Research, USA) which emits a wavelength of 532 nm that excites the fluorescent tracer particles (Fluoro-Max, Thermofisher, USA). The laser timing is controlled using a programmable triggering unit that synchronize the timing of the laser trigger with the CCD camera. The laser line passes through a filter cube which consists of a dichroic mirror and filter. The dichroic mirror directs the laser line to the device, but also only allows the wavelength of the returning emitted light from the fluorescent particles to pass through while filtering any other wavelength of light. The emitted light from the tracer particles is then routed to a dual-camera port that allows for the selection of the CCD camera used for µPIV or the high-speed camera (Graftek Imaging, Inc., USA) used for the CFL measurement. For further information regarding µPIV background, limitations, and correlation techniques, refer to A.1.

3.3.1 Flow Rate Measurements

In our study, we simulate a microcirculatory environment by using microchannels with diameters of 25 µm and 50 µm. These small channels serve as a model for capillary-like conditions, allowing us to achieve wall shear rates comparable to those found in physiological capillaries. Using the viscosity of blood, approximated as 3.5 cP, and assuming blood behaves as a Newtonian fluid under these conditions, the range of flow rates can be calculated for each channel size using the wall shear rate ($\dot{\gamma}_w$) equation [17]:

$$\dot{\gamma}_w = \frac{4Q\mu}{\pi R^3}$$

where Q is the flow rate, μ is the viscosity of blood, and R is the radius of the channel.

Rearranging to solve for Q in terms of WSR gives:

$$Q = \frac{\dot{\gamma}_w \cdot \pi R^3}{4\mu}$$

The physiological parameters for the human circulatory system provide key insights into capillary vessel characteristics, particularly in terms of vessel diameter, mean flow velocity, and wall shear rate. Capillaries typically have diameters ranging from 5 to 10 µm but can reach up to 40 µm, with mean flow velocities between 100 and 500 µm/s and wall shear rates spanning 400 to 1600 s^{-1} [40]. During the design planning phase, we were able to determine the flow rate range for our study:

- For the 25 µm channel, the calculated flow rate range was 0.0589 to 0.118 µl/min.
- For the 50 µm channel, the calculated flow rate range was 0.295 to 1.47 µl/min.

3.3.2 Image Post-Processing

This section outlines the post-processing techniques used to determine CFL thickness from HSC image acquisition, as well as the velocity profiling and cross-correlation methods used to generate the velocity profile figures.

CFL Aquisition

The optical CFL thickness (δ_o) is determined using images from the HSC. Figure 3.5 shows the raw images captured with the HSC for a 50 µm diameter channel, suspended in PBS at a pressure flow setting of 20 mBar across varying Ht. These images are imported into a MATLAB application designed for image processing to obtain the CFL thickness, developed by Fenech et al. (2023) [20]. The MATLAB application interface shown in Figure 3.6 outlines the steps for how to use the GUI to extract CFL information like the RBC core thickness or CFL thickness. For this study, the RBC core is detected using the gradient-based spatiotemporal processing technique, `GradXYT`, which applies intensity gradients across spatial (X, Y) and temporal (T) dimensions. By computing the local variation of pixel intensity over time, the method is the best for distinguishing between the core and the surrounding plasma. It can segment the core even in cases of low image contrast or varying illumination conditions. Once the core is identified, the δ_o is determined based on the ratio of the detected RBC core width (δ_{core}) to the total channel diameter (D), as follows:

$$\delta_o = \frac{D - \delta_{\text{core}}}{2} \tag{3.1}$$

By measuring the RBC core and using the known channel diameter, the CFL can be calculated more precisely, ensuring a more reliable estimation than direct CFL extraction, which is more sensitive to image contrast limitations or identifying the exact boundaries of the channel.

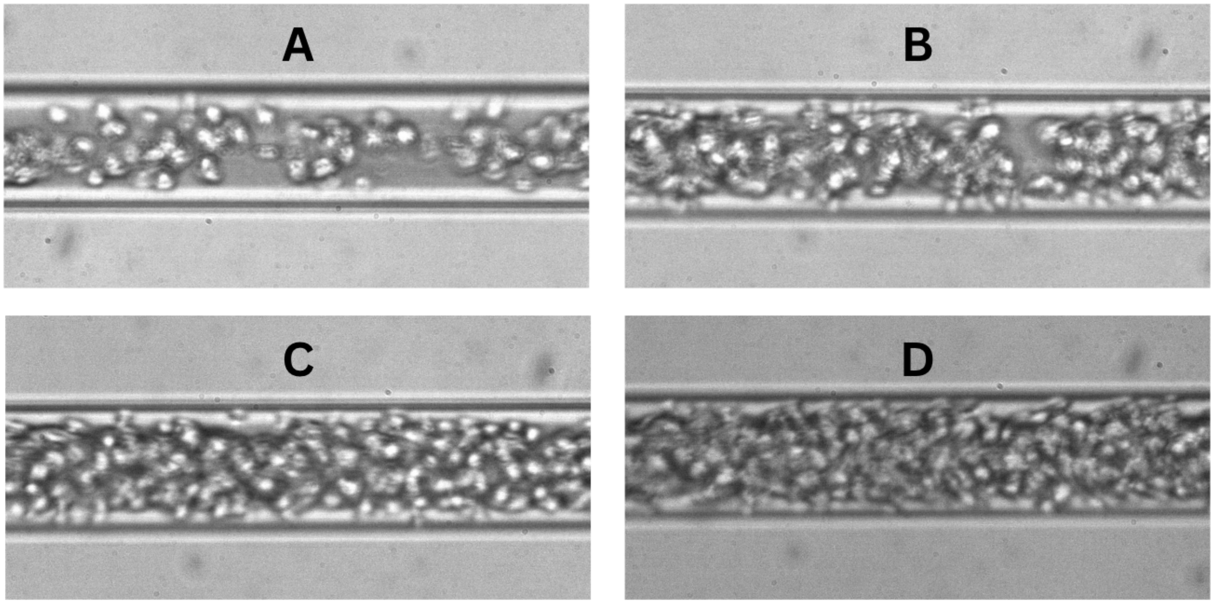

Figure 3.5: High-speed camera (HSC) images captured for a 50 µm diameter circular microchannel with red blood cells suspended in PBS at a pressure setting of 20 mBar. The four panels correspond to increasing hematocrit (Ht) levels: (A) 5%, (B) 10%, (C) 15%, and (D) 20%. These images are used as input for a custom MATLAB application (Fenech et al., 2023) to extract the optical CFL thickness (δ_o). The RBC core is segmented using the gradient-based spatiotemporal filter `GradXYT`, and δ_o is calculated from the detected core width relative to the total channel diameter.

Velocity Profile Aquisition

To locate the center plane, a series of velocity field measurements is taken as the stage moves incrementally along the z-axis, controlled by the Mitas stage controller. The center plane is identified when the measured velocity reaches a peak and then begins to decrease as the measurement plane shifts. The center is also identified visually by trying to achieve the most high-definition view of the fluorescent particles in live flow. Once the center plane

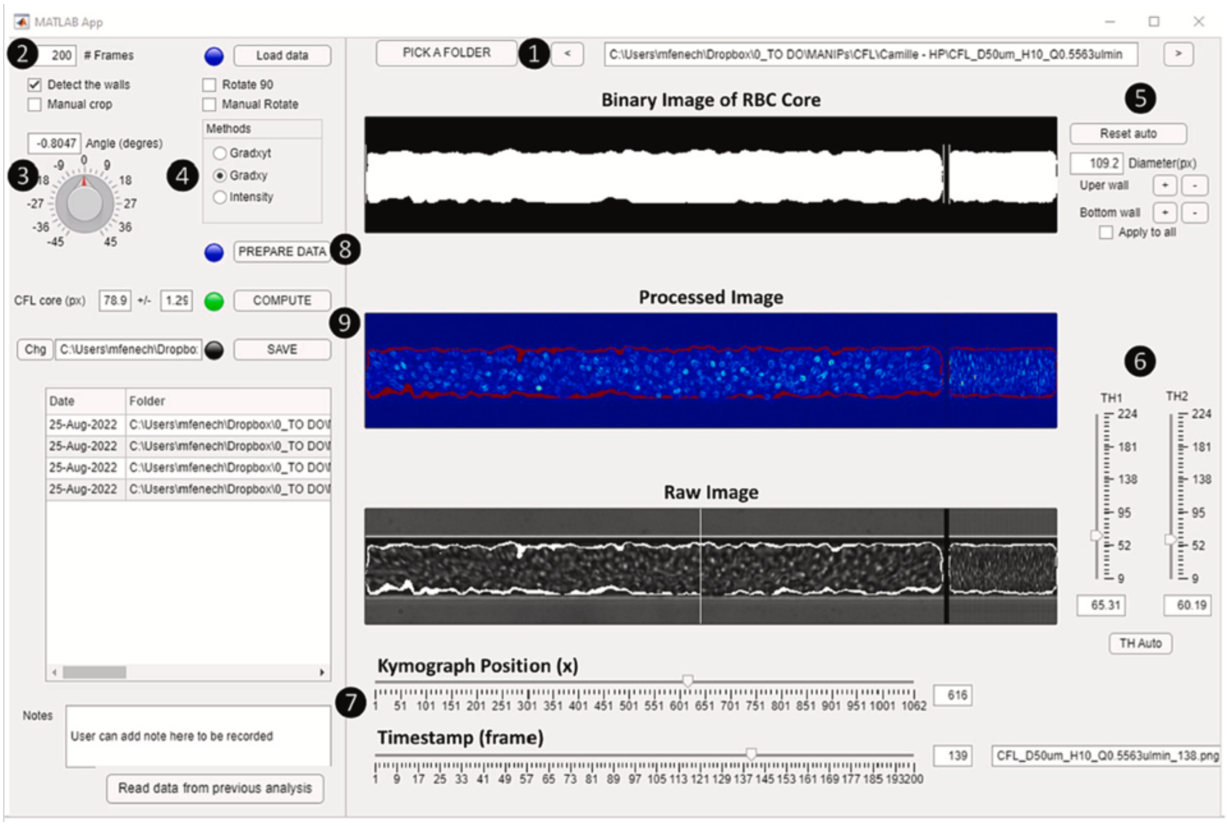

200 # Frames

☑ Detect the walls

☐ Manual crop

☐ Rotate 90

☐ Manual Rotate

-0.8047 Angle (degres)

Methods

○ Gradxyt

● Gradxy

○ Intensity

CFL core (px) 78.9 +/- 1.29

Chg C:\Users\mfenech\Dropbo:

C:\Users\mfenech\Dropbox\0_TO DO\MANIPs\CFL\Camille - HP\CFL_D50um_H10_Q0.5563ulmin

109.2 Diameter(px)

☐ Apply to all

TH1 65.31

TH2 60.19

Date	Folder
25-Aug-2022	C:\Users\mfenech\Dropbox\0_TO DO\
25-Aug-2022	C:\Users\mfenech\Dropbox\0_TO DO\
25-Aug-2022	C:\Users\mfenech\Dropbox\0_TO DO\
25-Aug-2022	C:\Users\mfenech\Dropbox\0_TO DO\

Notes: User can add note here to be recorded

Kymograph Position (x) 616

Timestamp (frame) 139 CFL_D50um_H10_Q0.5563ulmin_138.png

Figure 3.6: Graphical user interface (GUI) on Matlab for CFL thickness acquisition, developed by Fenech et al. (2023) [20]. Users can select a folder of images (Step 1) and specify the number of frames to load (Step 2). A channel rotation knob (Step 3) adjusts orientation, ensuring horizontal alignment. Three image processing methods enhance visualization (Step 4): - gradient (spatial edges), - gradient (spatiotemporal changes), and intensity (brightness-based segmentation). Manual adjustments refine channel wall positions, diameter (Step 5), and RBC core detection thresholds (Step 6). Scrolling bars allow navigation along the -axis for kymograph positioning (Step 7) and frame-by-frame inspection. Once settings are finalized, users click “Prepare Data” (Step 8) to apply configurations across all frames, then “Compute” (Step 9) to process and save RBC core detection results.

is located, the next step is to optimize the laser pulse timing for the specific flow rate. The time interval between consecutive laser pulses in micro-particle image velocimetry (dt) must be adjusted to achieve effective cross-correlation. Ideally, the fluorescent particles should travel *at least* 5-10 pixels between paired images, which depends on their speed. The region of interest for this optimization is the entirety of the microchannel in view.

With the center plane and optimized dt established, velocity field measurements are conducted. For each flow rate, 100 pairs of images are recorded. The interrogation window starts at 64×64 pixels and then reduces to 24×24 pixels with 87% overlap to ensure sufficient particle presence. The correlation windows are oval-shaped with a 4:1 aspect ratio, aligned with the flow direction to enhance vector resolution. To calculate the particle displacement between paired images, the Nguyen cross-correlation algorithm [41] is used, as discussed in Appendix A.1. The cross-correlation results are averaged across the paired images and along the channel length to produce an averaged 2D velocity profile in the flow direction. To improve the accuracy of the 2D velocity profile, the standard deviation of the velocity measurements at each point is calculated. This standard deviation serves as an indicator of measurement reliability. When the standard deviation at a specific position is zero or near zero, it confirms that the corresponding point represents a true velocity measurement within the channel. Conversely, if the standard deviation at a point is significantly greater than zero, it suggests the presence of noise or other fluctuations, indicating that this measurement is outside the channel. These high-variance points are therefore disregarded in the analysis. Figure 3.7 provides a visual of the velocity acquisition process.

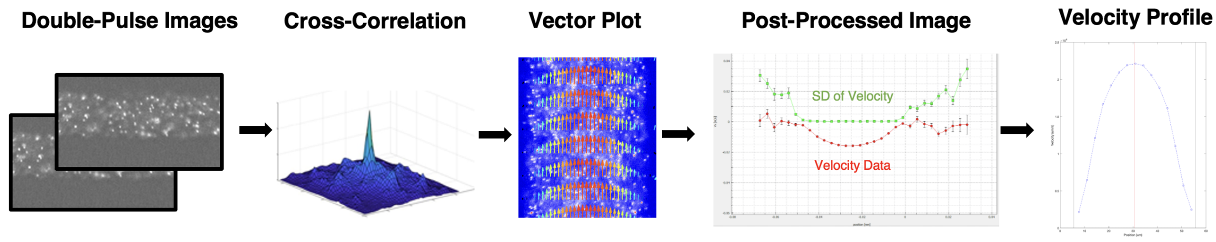

Figure 3.7: µPIV Velocity Profile Acquisition Workflow. Step-by-step process used to extract velocity profiles from microfluidic blood flow experiments using µPIV. (1) Double-pulse images: Sequential images captured using a high-speed camera with fluorescent tracer particles suspended in the flow. (2) Cross-correlation: Nguyen correlation algorithm [41] is applied to determine the displacement of tracer particles between image pairs. (3) Vector plot: Velocity vectors are generated based on particle displacement, visualizing flow direction and magnitude. (4) Post-processed image: The velocity field is refined by averaging multiple image pairs with velocity data (red) and standard deviation (green) plotted. Where SD is zero indicates true velocity measurements within the channel (5) Velocity profile: Truncated and extracted velocity profile is displayed, showing the parabolic distribution typical of microchannel flow, with a peak at the center line (red line).

3.4 Mathematical Analysis of Velocity Profiles

This section introduces our developed Core-Plasma Model, which differentiates the RBC-rich core from the surrounding plasma region. It also outlines the MATLAB-based framework used to analyze μPIV velocity data, extracting key parameters such as velocity profiles, shear rates, viscosity, and CFL thickness. The framework automates data extraction, velocity alignment, numerical differentiation, and model fittings to characterize blood flow, incorporating the Newtonian, Power Law, Carreau, and Double-Parameter Power Fit described in section 2.5. Additionally, an alternative approach for CFL thickness determination is introduced using hydrodynamic shear rate at discontinuity analysis.

3.4.1 Our Developed Blood Model: Core-Plasma

Building upon existing blood flow models discussed in section 2.5, we developed a Core-Plasma Model that incorporates both Newtonian and non-Newtonian properties to more accurately represent blood flow in small-diameter vessels. This two-phase model accounts for the distinct behavior of the plasma-rich CFL and the RBC-rich core. The CFL follows Newtonian fluid dynamics with plasma viscosity μ_p, while the RBC-rich core is modeled as a non-Newtonian power-law fluid.

The flow domain is separated into two regions:

- A **Newtonian CFL layer** ($R - \delta \leq r \leq R$), where blood behaves as a Newtonian fluid with viscosity μ_p, representing the plasma-rich CFL.
- A **Non-Newtonian core** ($0 \leq r < R - \delta$), where blood is modeled as a power-law fluid with consistency index K_{cp} and flow index n_{cp}.

We assume steady, incompressible, laminar, fully developed, and axisymmetric flow in a cylindrical tube, and neglect body forces. A complete derivation of the governing equations and velocity profiles is provided in Appendix A.3.

Velocity Profile – Newtonian CFL ($R - \delta \leq r \leq R$)

In the CFL, blood behaves as a Newtonian fluid. Solving the simplified Navier–Stokes equation with the no-slip condition at $r = R$ and continuity of shear stress at $r = R - \delta$, we obtain:

$$u(r) = \frac{\Delta P}{4\mu_p L}(r^2 - R^2)$$

Velocity Profile – Non-Newtonian Core ($0 \leq r < R - \delta$)

In the core, blood is modeled as a power-law fluid with $\tau_{rz} = K_{cp}\left(\frac{du}{dr}\right)^{n_{cp}}$. Applying the symmetry condition at $r = 0$ and continuity of velocity at $r = R - \delta$, the velocity is:

$$u(r) = \left(\frac{\Delta P}{2K_{cp}L}\right)^{\frac{1}{n_{cp}}} \frac{n_{cp}}{n_{cp}+1}\left[r^{\frac{n_{cp}+1}{n_{cp}}} - (R-\delta)^{\frac{n_{cp}+1}{n_{cp}}}\right] \quad + \frac{\Delta P}{4\mu_p L}\left[(R-\delta)^2 - R^2\right]$$

Final Core-Plasma Model:

$$u(r) = \begin{cases} \frac{\Delta P}{4\mu_p L}(r^2 - R^2), & r \geq (R-\delta) \\ \left(\frac{\Delta P}{2K_{cp}L}\right)^{\frac{1}{n_{cp}}} \frac{n_{cp}}{n_{cp}+1}\left[r^{\frac{n_{cp}+1}{n_{cp}}} - (R-\delta)^{\frac{n_{cp}+1}{n_{cp}}}\right] \quad + \frac{\Delta P}{4\mu_p L}\left[(R-\delta)^2 - R^2\right], & r < (R-\delta) \end{cases} \tag{3.2}$$

where:

- ΔP is the pressure drop,
- μ_p is the Newtonian viscosity of plasma,
- L is the vessel length,
- r is the radial distance from the channel center,

- R is the total vessel radius,
- CFL is the CFL thickness,
- K_{cp} and n_{cp} are the consistency and flow indices governing non-Newtonian behavior.

A velocity distribution, shown in Figure 3.8, illustrates an example of the Core-Plasma Model overlaid on experimental data, highlighting distinct regions in the RBC-rich core and the surrounding CFL.

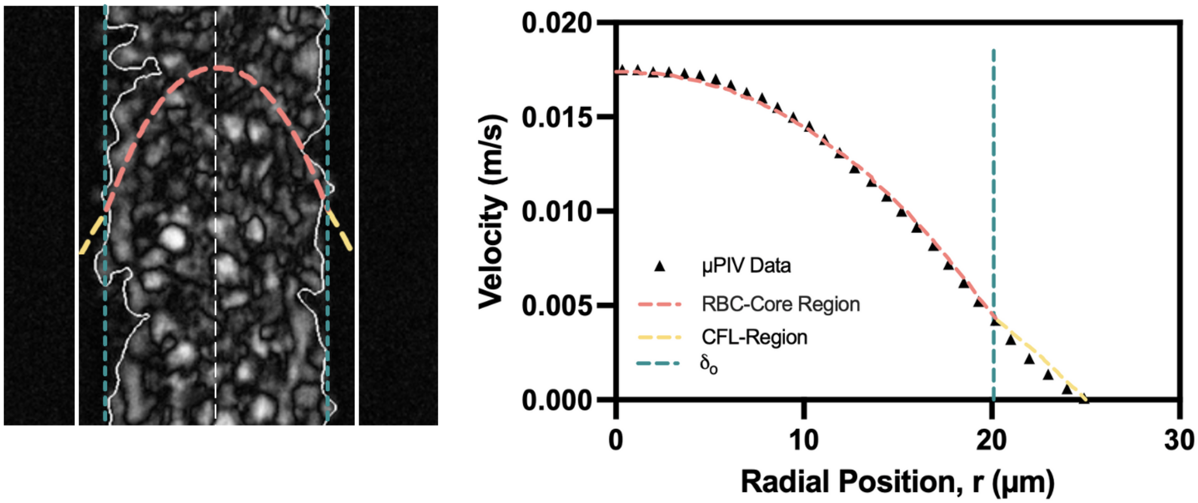

Figure 3.8: Visualization of the Core-Plasma Model for a 15% hematocrit suspension in plasma flowing through a 50 μm microchannel under 180 mbar pressure. The left panel shows a high-speed image of RBC distribution at high-contrast with overlaid core and CFL boundaries. The right panel plots the velocity profile extracted from micro-particle image velocimetry (μPIV data), with segmented fits for the RBC core (red dashed) and CFL region (yellow dashed). The vertical dashed line indicates the optical cell-free layer thickness (δ_o).

Shear Rate Profiles The corresponding shear rate $\dot{\gamma}(r)$ in both regions is given by:

$$\dot{\gamma}(r) = \begin{cases} -\frac{\Delta P}{2\mu_p L} r, & \text{if } r \geq (R-\delta) \quad \text{(CFL region)} \\ -\left(\frac{\Delta P}{2K_{cp}L}\right)^{\frac{1}{n_{cp}}} r^{\frac{1}{n_{cp}}}, & \text{if } r < (R-\delta) \quad \text{(RBC core)} \end{cases} \tag{3.3}$$

The gradient of shear rate, which captures spatial variations in shear stress, is given by:

$$\nabla\dot{\gamma} = \frac{d\dot{\gamma}}{dr} = \begin{cases} \frac{\Delta P}{2\mu_p L}, & \text{if } r \geq (R-\delta) \\ \frac{1}{n_{cp}} \left(\frac{\Delta P}{2K_{cp}L}\right)^{\frac{1}{n_{cp}}} r^{(1/n_{cp})-1}, & \text{if } r < (R-\delta) \end{cases} \tag{3.4}$$

Flow Rate Calculations The volumetric flow rate Q is obtained by integrating the velocity profile across the cross-section:

$$Q = 2\pi \int_0^R u(r) r \, dr \tag{3.5}$$

Splitting this into the Newtonian CFL and the non-Newtonian core regions:

$$Q_{CFL} = 2\pi \int_{R-\delta}^{R} \frac{\Delta P}{4\mu_p L}(r^2 - R^2) r \, dr \tag{3.6}$$

$$Q_{Core} = 2\pi \int_0^{R-\delta} u(r) r \, dr \tag{3.7}$$

Explicit integrations of these terms yield expressions for the total flow rate, reflecting the contributions of both layers.

Model Advantages and Limitations Unlike previous models, this approach explicitly accounts for the plasma layer near the vessel wall, improving predictions of shear stress distribution and flow resistance. It provides a more realistic representation of RBC aggregation and deformation in the vessel core. However, it assumes a distinct boundary between the core and CFL, whereas in reality, there is a gradual transition. Additionally, accurate CFL thickness measurements are required for precise flow predictions.

3.4.2 DETERMINING SHEAR RATE, SHEAR RATE GRADIENT, AND SHEAR STRESS

The shear rate is identified by locating the boundary between the CFL and the RBC core, where a discontinuity occurs. This discontinuity is marked by an abrupt change in shear rate ($\dot{\gamma}$), reflecting the distinct rheological properties of the plasma-rich CFL, which behaves more like a Newtonian fluid, and the RBC-dense core, which exhibits non-Newtonian characteristics. The shear rate profile is approximated by two slopes: one originating at the vessel center ($r = 0$) and extending towards an unknown intersection point (ip), and another slope up to the vessel wall ($r = R$). The goal is to determine the intersection point, so we can identify the hydrodynamic CFL (δ_h). Mathematically, the shear rate ($\dot{\gamma}$) is expressed as:

$$\dot{\gamma}_1(r) = m_1 r, \quad 0 \leq r < r_{\text{ip}} \tag{3.8}$$

$$\dot{\gamma}_2(r) = m_2(r - r_{\text{ip}}) + m_1 r_{\text{ip}}, \quad r_{\text{ip}} \leq r \leq R \tag{3.9}$$

where:

- m_1 is the slope of the first linear region (RBC core),
- m_2 is the slope of the second region (CFL),
- r_{ip} is the shear rate at discontinuity point, representing the hydrodynamic RBC core boundary.

To determine r_{ip}, we minimize the squared error between the measured shear rate data and the piecewise linear model:

$$J(m_1, m_2, r_{\text{ip}}) = \sum_{i=1}^{N} \left(\dot{\gamma}_i - \hat{\dot{\gamma}}(r_i)\right)^2 + \max(0, r_{\text{ip}} - R), \tag{3.10}$$

where $\hat{\dot{\gamma}}(r_i)$ represents the fitted shear rate values and the additional term ensures that the transition point remains within the physical boundary $r_{\text{ip}} \leq R$. Once r_{ip} is optimized, the hydrodynamic CFL thickness is computed as:

$$\delta_h = R - r_{\text{ip}}. \tag{3.11}$$

Shear Rate at Discontinuity: The shear rate at the discontinuity ($\dot{\gamma}_{\text{d}}$) quantifies the rate of deformation at the boundary between the RBC core and the CFL. It is defined as:

$$\dot{\gamma} = \left.\frac{du}{dr}\right|_{r_{\mathrm{ip}}} \tag{3.12}$$

This value represents the final shear rate within the RBC core before transitioning into the CFL, marking the point where the flow dynamics shift from a non-Newtonian to a Newtonian regime.

Gradient of Shear Rate: The gradient of the shear rate is given by:

$$\nabla\dot{\gamma} = \left.\frac{d\dot{\gamma}}{dr}\right|_{0-r_{\mathrm{ip}}} \tag{3.13}$$

Shear Stress: The shear stress is given by:

$$\tau = \left.\mu_{app}\dot{\gamma}\right|_{r_{\mathrm{ip}}} \tag{3.14}$$

Figure 3.9 presents a representative shear rate profile, illustrating how linear fits differentiate the RBC core and CFL regions. The plots correspond to half of the microchannel width.

3.4.3 Determining Local Viscosity Using the Carreau Model

To characterize the local viscosity $\mu_c(\dot{\gamma})$ of blood under varying shear rates, we applied the Carreau model to the experimental velocity data extracted from μPIV measurements.

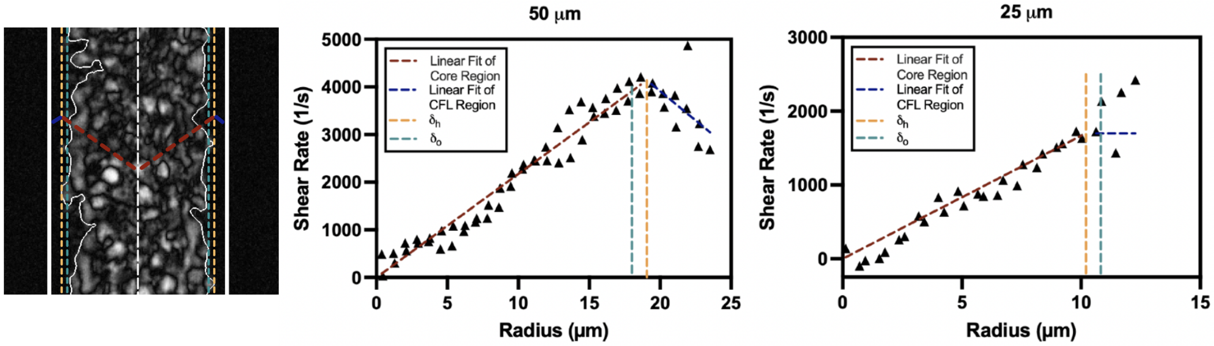

Figure 3.9: Schematic and corresponding shear rate profiles of a 15% hematocrit suspension in plasma flowing through 50 µm (center) and 25 µm (right) microchannels under an applied pressure of 180 mbar. The left panel shows a representative high-speed image of RBC distribution at a high-contrast, with overlaid markers indicating the core and CFL boundaries. The center and right graphs display shear rate as a function of radial position, with linear fits for the core (red dashed line) and CFL (blue dashed line) regions. Vertical dashed lines denote the hydrodynamic (δ_h) and optical (δ_o) CFL thickness.

The methodology involved the following steps:

Shear Rate Computation. The first step in determining local viscosity is computing the shear rate $\dot{\gamma}$ at each velocity data point. Given the velocity profile $u(r)$, the local shear rate was determined at each radial position using:

$$\dot{\gamma}(r) = \left| \frac{du}{dr} \right|, \tag{3.15}$$

Carreau Model Parameterization. The shear rate values at each velocity data point are then used in the Carreau viscosity equation:

$$\mu_c(\dot{\gamma}) = \mu_\infty + (\mu_0 - \mu_\infty) \left[1 + (\lambda_c \dot{\gamma})^2 \right]^{(n_c - 1)/2}, \tag{3.16}$$

where μ_0, μ_∞, λ_c, and n_c are model parameters initialized based on values reported by Mehri et al. (2018) for hematocrit levels of 5-15% and refined through optimization. The initialization will be explained in more detail in the next section.

Local Viscosity Plot. All local viscosity values are compiled and plotted across the full range of velocity data.

3.4.4 MATLAB Framework

A MATLAB framework is developed to automate the extraction, processing, and analysis of experimental velocity data, facilitating the computation of key parameters such as shear rate, viscosity, and hydrodynamic CFL thickness.

Automated Data Extraction and Naming Convention. The framework begins with an automated data extraction function, `RoundExtractInfo`, which systematically retrieves velocity profile datasets from μPIV measurements. This function enforces consistency in data acquisition by structuring each dataset into a standardized format for subsequent analysis. A structured file-naming convention is implemented to encode experimental conditions, allowing automated parsing of the following parameters:

- u: Velocity measurements from μPIV
- r: Radial distance from the channel center
- R: Channel radius

- Q_{exp}: Measured flow rate
- P_{exp}: Measured pressure
- δ_o: Optical cell-free layer thickness
- L: Channel length

Model and Fit Computation Table 3.1 provides a structured overview of the computational models and fitting methods used in the MATLAB framework. It outlines how we extracted key rheological and fitting parameters, which we will explore further in this study. The table is designed to track the progression from initial conditions to final computed values, ensuring a clear understanding of how each parameter is derived. At the start, initialized parameters provide the initial condition for optimization functions. These values come from experimental measurements or literature data. The experimental pressure gradient, PG_{exp}, is obtained by dividing the applied pressure by the length of the channel. The $\mathrm{PG}_{\mathrm{exp}}$ and Poiseuille viscosity calculations are frequent initialized parameters. Since pressure drop within the tubing is found to be negligible (see Appendix A.4), $\mathrm{PG}_{\mathrm{exp}}$ is used as an initial estimation of fluid properties. Next, fixed parameters are constants that remain unchanged during calculations. These are based on experimentally determined values that directly feed into the models, such as the channel radius (R). Finally, the computed output parameters are extracted from each fit or model.

Graphical and Data Output. The MATLAB framework generates a series of graphical outputs to visualize velocity profiles, shear rate distributions, and viscosity variations

Table 3.1: Summary of models and computational methods with initialized, fixed, and output parameters used in the MATLAB framework. *Average values from Mehri et al. (2018) for 5-15% Ht [16].

Calculation Reference	Initialized Parameter	Fixed Parameter	Output Parameter
Experimental $\mathrm{PG}_{\mathrm{exp}} = \frac{P_{\mathrm{exp}}}{L}$	-	P_{exp}, L	$\mathrm{PG}_{\mathrm{exp}}$
Poiseuille (2.2) $\mu_{app} = \frac{P_{\mathrm{exp}} \pi R^4}{8 L Q_{\mathrm{exp}}}$	-	P_{exp}, L, R, Q_{exp}	μ_{app}
Newtonian (2.5.1)	$\mathrm{PG}_{\mathrm{exp}}$, μ_{app}	R	$\mathrm{PG}_{\mathrm{exp}}$, μ_{app}
Power Law (2.5.2)	$\mathrm{PG}_{\mathrm{exp}}$	R	$\mathrm{PG}_{\mathrm{exp}}$, n_p, K_p
Double-Parameter Power Fit (2.5.4)	u_{max}	R	u_{max}, k_1, k_2
Carreau (2.5.3)	μ_0 (0.0730 mPa-s)* μ_∞ (0.00195 mPa-s)* λ_c (3.31 s)*	-	μ_0, μ_∞, λ_c, n_c, $\mu_c(\dot{\gamma})$
Core-Plasma (3.4.1)	$\mathrm{PG}_{\mathrm{exp}}$, , μ_{app} (Assume $\mu_p = \mu_{app}$)	R, δ_o	PG_{cp}, K_{cp}, n_{cp}
Shear Discontinuity (3.4.2)	$\mathrm{IP} = R - \delta_o$ $\dot{\gamma}_1(r) = \frac{u_{\mathrm{max}}}{\mathrm{ip}}$ $\dot{\gamma}_2(r) = 0$	R, δ_o	r_{ip}, δ_h, $\dot{\gamma}$, $\nabla\dot{\gamma}$, τ

across different models. Additionally, all computed parameters and model fits are systematically logged in structured text files for reproducibility and further analysis. A dedicated `Results_Log.txt` file records key computational results and output parameters.

3.5 Statistical Analysis Methods

Statistical analyses are conducted using GraphPad Prism, a software widely used for data visualization and statistical testing in scientific research. The statistical tests applied in this study include Root Mean Square (RMS) error calculations, ordinary one-way ANOVA, simple linear regression, and significance testing based on a 95% confidence level.

ROOT MEAN SQUARE (RMS) ERROR

The root mean square (RMS) error quantifies the deviation between experimental data and model predictions, providing a measure of model accuracy. It is calculated as:

$$\text{RMS Error} = \sqrt{\frac{1}{N}\sum_{i=1}^{N}(y_i^{\text{exp}} - y_i^{\text{model}})^2} \tag{3.17}$$

where y_i^{exp} represents the experimentally measured values, y_i^{model} are the corresponding theoretical predictions, and N is the total number of data points. A lower RMS error indicates a better fit between the model and experimental data, while a higher RMS error suggests greater discrepancies.

ORDINARY ONE-WAY ANOVA WITH SIDAK MULTIPLE COMPARISONS

Ordinary one-way Analysis of Variance (ANOVA) is used to determine whether there were statistically significant differences between multiple experimental groups. ANOVA tests the null hypothesis that all group means are equal by comparing the variance within groups to the variance between groups, yielding a p-value that indicates the probability of observing the data if the null hypothesis were true. If a significant difference is detected ($\mathbf{p < 0.05}$), Sidak's multiple comparison test is applied as a post hoc analysis to identify which specific groups differed from each other.

The significance levels are denoted as:

- $\mathbf{p < 0.05}$ (*) – Significant difference

- $\mathbf{p < 0.01}$ (**) – Strong significant difference
- $\mathbf{p < 0.001}$ (***) – Highly significant difference
- $\mathbf{p < 0.0001}$ (****) – Extremely significant difference

SIMPLE LINEAR REGRESSION

To analyze trends between experimental variables, simple linear regression is applied using GraphPad Prism. The linear regression model follows:

$$y = mx + b \tag{3.18}$$

where m is the slope of the regression line, representing the rate of change, and b is the y-intercept. The goodness-of-fit is evaluated using the coefficient of determination (R^2), which quantifies how well the independent variable explains the variance in the dependent variable. Higher R^2 values indicate stronger correlations. Additionally, a p-value is obtained from the regression analysis to assess whether an increasing or decreasing trend was statistically significant.

CHAPTER 4

COMPARATIVE ANALYSIS OF BLOOD FLOW MODELS

4.1 RESULTS

This section presents the experimental and computational findings, focusing on velocity profiles, non-Newtonian parameters, and CFL measurements. The velocity profiles are compared across different rheological and fitting models to evaluate their performance in capturing experimental data. Additionally, the non-Newtonian parameters derived from model fittings are reported, highlighting the flow characteristics of blood in microchannels. Finally, optical and hydrodynamic methods for CFL measurement are compared to identify the method that best captures CFL thickness. For each velocity profile, a flow rate measurement is taken for each applied pressure. For reference, the results for the measured flow rates tested for each channel size and suspension, across a series of applied pressures (20 to 200 mBar) can be found in Appendix A.2 .

4.1.1 Velocity Profiles and Model Performance

Figures 4.1 and 4.2 present examples of the velocity and shear rate distributions for a 15% Ht suspension in plasma within 50 μm and 25 μm microchannels under 180 mbar pressure. The velocity profiles (Figures 4.1A, 4.2A) exhibit a slightly blunted, parabolic shape, with μPIV data aligning closely with theoretical fits. In the present cases, the CFL boundaries, δ_o and δ_h, are clearly defined and show close agreement, with a thinner CFL is observed in the 25 µm channel. To evaluate the accuracy of each Model against the experimental data, the root mean square (RMS) error is calculated, detailed in Section 3.5. According to the figure, the velocity RMS (Figures 4.1C, 4.2C) remain low in the core but increases at the CFL boundary. The shear rate is also evaluated (Figures 4.1B, 4.2B), showing a distinct discontinuity at the CFL-core interface, particularly in the 50 μm channel. The shear rate RMS (Figures 4.1D, 4.2D) shows more error near the CFL boundary for both channel sizes, but its particularly evident in the 25 μm channel.

A summary of the velocity RMS and shear rate RMS is presented in Figure 4.3. Overall, the Double-Parameter Power Fit (Two Parameters) demonstrates the lowest error across all conditions, having the best performance. Among the rheological models, the Core-Plasma Model exhibits the best agreement with experimental data, particularly in the 50 μm channel. In contrast, the Carreau Model performs the worst, while the Newtonian and Power Law Models displays intermediate accuracy, showing comparable results across all conditions. Notably, difference between models are more pronounced in the 50 μm channel compared to the 25 μm channel.

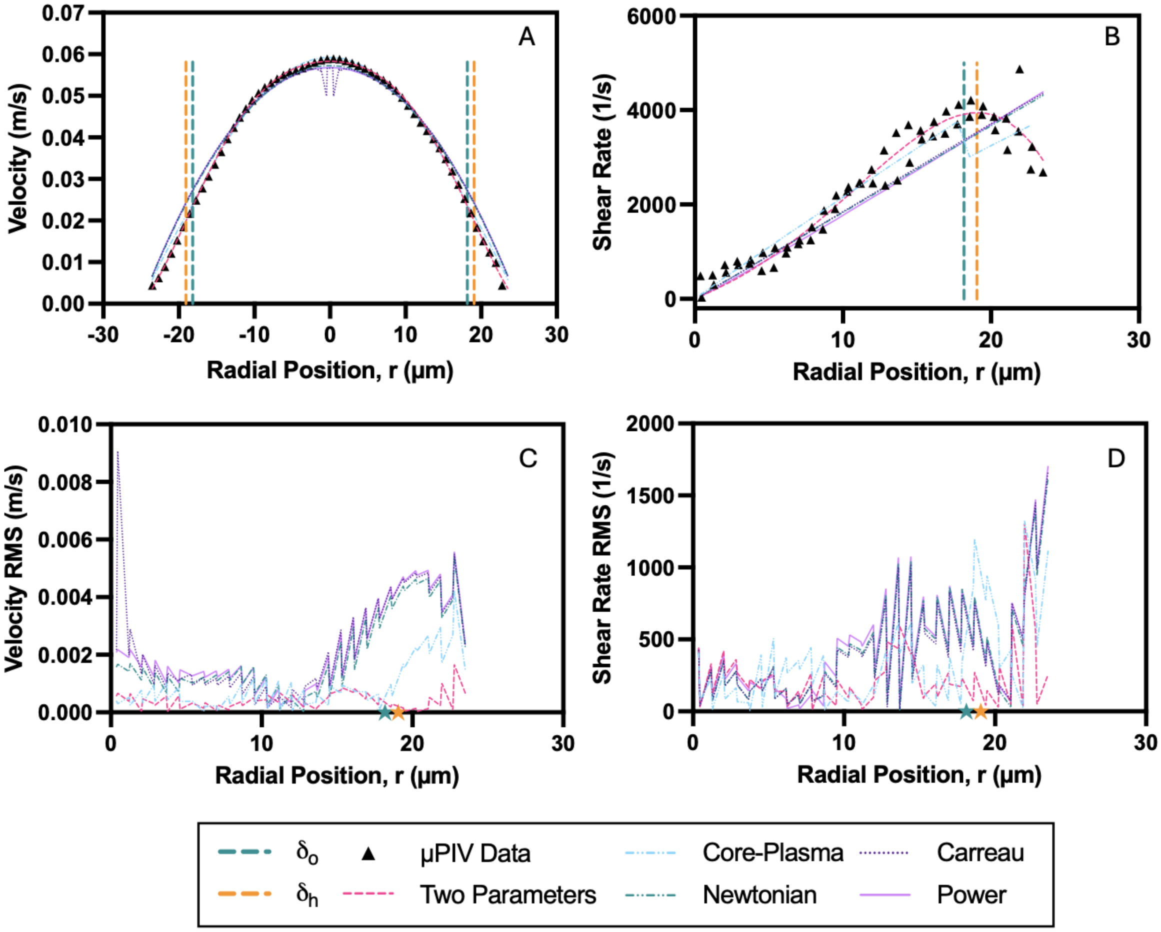

Figure 4.1: Flow dynamics of a 15% hematocrit suspension in plasma within a 50 µm microchannel under an applied pressure of 180 mbar. (A) Velocity profile normalized to the channel position, showing experimental μPIV data and Model fits. (B) Shear rate distribution with μPIV data overlaid against various Models. (C) Velocity RMS along the radial position of channel. (D) Shear rate RMS along the radial position of channel.

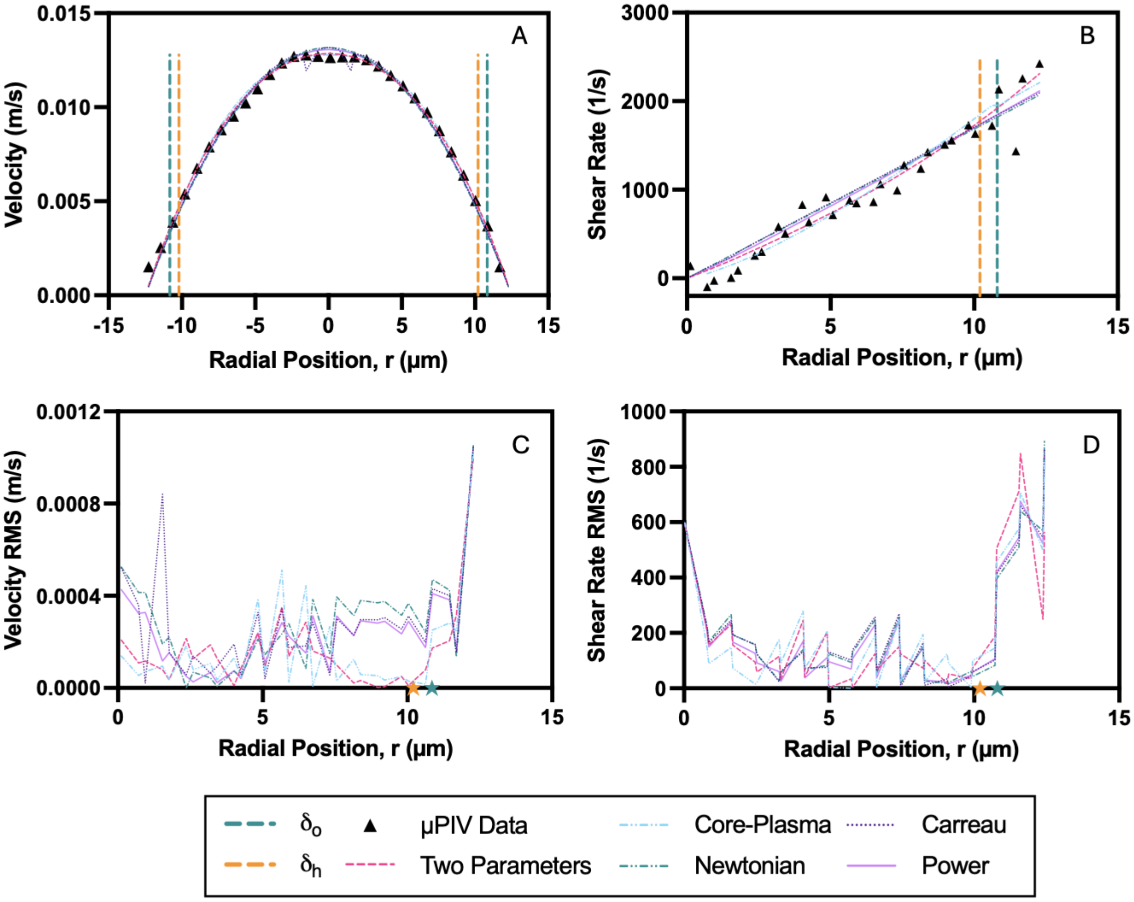

Figure 4.2: Flow dynamics of a 15% Ht suspension in Plasma within a 25 µm microchannel under an applied pressure of 180 mbar. (A) Velocity profile normalized to the channel position, showing experimental μPIV data and Model fits. (B) Shear rate distribution with μPIV data overlaid against various Models. (C) Velocity RMS along the radial position of channel. (D) Shear rate RMS along the radial position of channel.

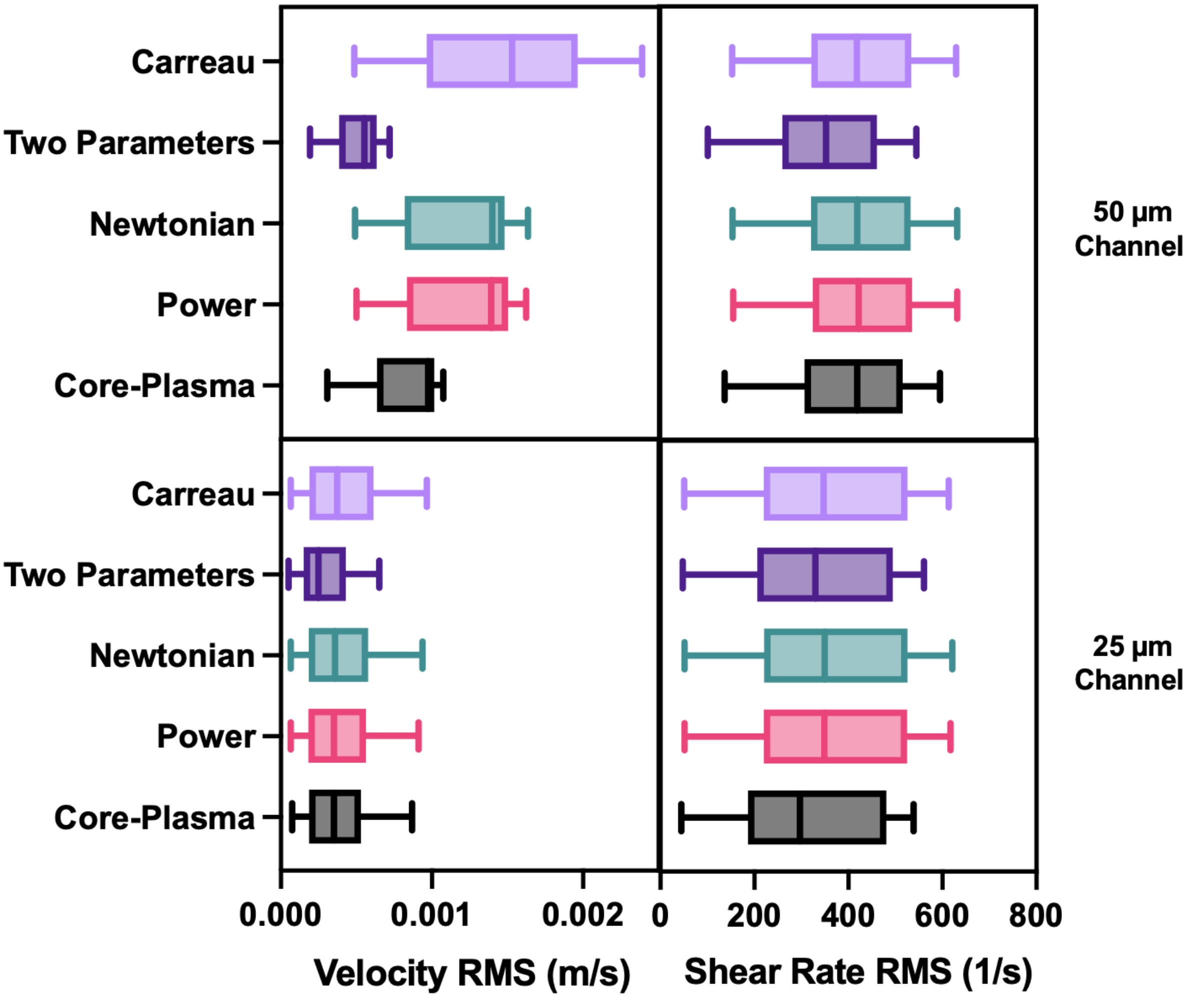

Figure 4.3: Comparison of RMS velocity (left) and RMS shear rate (right) values across various Model types (Carreau, Two Parameters, Newtonian, Power, and Core-Plasma) for blood suspensions at different hematocrit levels (5%, 10%, 15%, 20%) in both PBS and plasma suspensions. Data is shown for two channel sizes: 50 µm (top columns) and 25 µm (bottom columns). Box plots represent the spread of the data across all conditions, highlighting variations in flow behavior and model predictions.

4.1.2 Characterization of Non-Newtonian Parameters

Table 4.1 summarizes the non-Newtonian parameters obtained from various Models, comparing them to literature values to assess their accuracy and relevance to microvascular blood flow. These values represent an average across channel sizes (50 µm, 25 µm), Ht levels (5%, 10%, 15%, 20%), and suspensions (PBS, plasma). While some of our results align with literature, differences arise due to variations in experimental conditions, such as channel geometry, Ht range, and flow regimes.

The **Poiseuille-derived** apparent viscosity ($\mu_{app} = 1.81$ mPa·s) falls within the physiological range ($1.50 - 2.00$ mPa·s) reported by Wells et al. (1962) [42], who measured bulk blood viscosity in cylindrical tubes across a range of shear rates, confirming that our overall flow resistance is consistent with prior studies.

The **Carreau Model** parameters exhibit strong agreement with Mehri et al. (2018) [16], particularly in the infinite-shear viscosity ($\mu_\infty = 1.68$ mPa·s) and time constant ($\lambda_c = 3.31$ s), indicating that the model captures the shear-thinning nature of blood. However, the zero-shear viscosity ($\mu_0 = 9.9$ mPa·s) in our experiments is lower than the literature values. Mehri et al. (2018) conducted experiments in rectangular microchannels (width 100 µm, height 50 µm) at Ht levels of 5–15%, which differ from our microchannel dimensions and higher Ht range.

The **Power Law Model** deviates more significantly from literature, with a lower consistency index ($K_p = 2.75$ Pa·s^n) and a higher flow behavior index ($n_p = 0.938$) compared to Mehri et al. (2018) [16]. This discrepancy suggests that the Power Law Model struggles to capture blood's viscosity transition across different shear rates. While Mehri et al. (2018) applied the Power Law Model to blood flow in relatively large microchannels, our study focuses on highly confined geometries.

The **Double-Parameter Power (DPP) Fit** results in shape factors of $k_1 = 0.293$ and $k_2 = 2.81$, aligning with Pitts et al. (2013), who studied blood flow in rectangular PDMS channels (40 × 110 µm dimension) [15]. The relatively low k_1 suggest that the velocity profile is less blunt near the axis, while the high k_2 suggests that the velocity gradient near the wall is steeper, meaning the flow remains relatively blunt near the wall.

As for the developed, **Core-Plasma Model**, the consistency index of $K_{cp} = 3.91$ Pa·s^n and a flow behavior index of $n_{cp} = 1.08$ suggests that this Model predicts a nearly Newtonian core.

Overall, these differences highlight how variations in channel geometry, Ht concentration, and measurement techniques influence model predictions. This section provides an overview of all collected data to ensure that our measurements align with physiological expectations. The following subsections will analyze how Ht, suspension type, and channel size influence these non-Newtonian parameters.

Apparent Viscosity

Figure 4.4 presents the Poiseuille-derived apparent viscosity (μ_{app}) as a function of experimental pressure gradient (PG_{exp}) for blood suspensions in PBS and plasma, across different Ht levels and channel sizes (50 μm and 25 μm). A log-log fitting approach is used

Table 4.1: Summary of Non-Newtonian parameters across varying channel sizes and hematocrit with comparison to the literature

Model	**Parameter (Symbol, Unit)**	**Present Results**	**Literature Results**
Experimental-Poiseuille	Pressure Gradient (PG_{exp}, Pa/m)	3.18×10^5	–
	Apparent Viscosity (μ_{app}, mPa·s)	1.81	1.50 – 2.00 [42]
Carreau Model	Zero-shear Viscosity (μ_0, mPa·s)	9.87	26.9 – 118.6 [16]
	Infinite-shear Viscosity (μ_∞, mPa·s)	1.68	1.6 – 2.3 [16]
	Time Constant (λ_c, s)	3.31	3.312 – 3.313 [16, 43]
	Flow Behaviour Index (n_c)	0.386	0.353 – 0.369 [16]
Core-Plasma Model	Consistency Index (K_{cp}, Pa·s^n)	3.91	–
	Flow Behaviour Index (n_{cp})	1.08	–
Power Law Model	Consistency Index (K_p, Pa·s^n)	2.75	9.9 – 62.2 [16]
	Flow Behaviour Index (n_p)	0.938	0.156 – 0.603 [16]
Double-Parameter Power Fit	Core Bluntness Shape Factor (k_1)	0.293	0 – 0.95 [15]
	Wall Bluntness Shape Factor (k_2)	2.81	1.74 – 3.66 [15]

to capture the nonlinear shear-thinning behavior of blood [16].

The results indicate that, overall, PBS suspensions (blue) exhibit higher apparent viscosity than plasma suspensions (yellow). Moreover, the best-fit log-log regression model confirms a negative slope across all conditions, indicating that apparent viscosity decreases as the pressure gradient increases. This trend is consistent for both the 50 μm and 25 μm channels, though differences in magnitude are observed. In the 50 μm channel, the slope values range from -0.08776 (5% PBS) to -0.2233 (20% Plasma), with plasma suspensions exhibiting steeper declines compared to PBS suspensions. A similar pattern is observed in the 25 μm channel, where the slopes range from -0.0573 (5% PBS) to -0.2329 (20% Plasma).

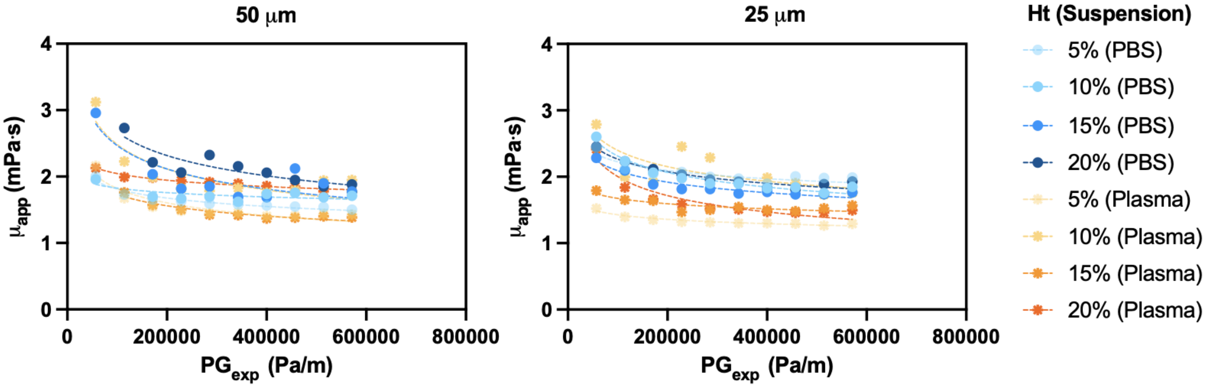

Figure 4.4: Apparent viscosity derived from Poiseuille as a function of experimental pressure gradient for a 50 µm (left) and 25 µm (right) microchannel. Data varies with Ht and suspension. Log-Log fitting is used for visualization.

CARREAU MODEL

The local viscosity using the Carreau Model (Methods, section 3.4.3) is shown in Figure 4.5

as a function of the local shear rate. It shows an example for a 15% Ht suspension in plasma under an applied pressure of 180 mbar within a 50 μm and 25 μm channel. The data follows the characteristic shear-thinning behavior predicted by the Carreau Model (section 2.5.3), where viscosity decreases as shear rate increases. The 50 μm channel exhibits a more gradual decline in viscosity over a broader range of shear rates, while the 25 μm channel reaches the plateau viscosity more quickly. In both channels, a rapid drop in viscosity is observed at low shear rates, followed by a plateau at higher shear rates, indicating a transition from the zero-shear to infinite-shear viscosity regime.

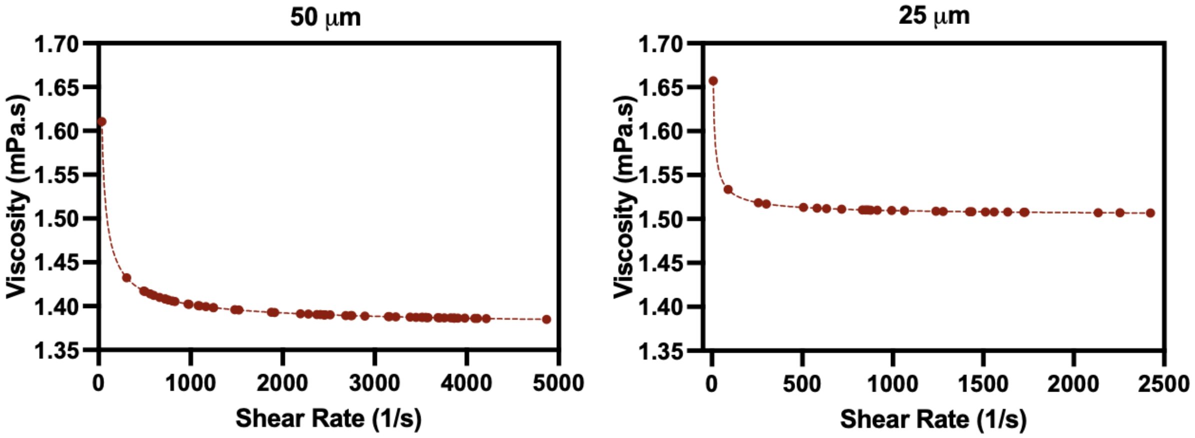

Figure 4.5: Local viscosity from the Carreau Model compared to local shear rate for a 50 µm (left) and 25 µm (right) microchannel. For 15% Ht suspension in Plasma under an applied pressure of 180 mbar. Fitted with Carreau Model with their respective Carreau parameters.

Taking a deeper dive into these regimes, Figure 4.6 presents the zero-shear viscosity (μ_0) trends as a function of experimental pressure gradient (PG_{exp}) across different Ht and suspensions in 50 μm and 25 μm microchannels. Simple linear regression is used to visually see the relationship between μ_0 and PG_{exp}. The statistical significance of the slope is evaluated using p-values to determine whether the increase in μ_0 is significantly different from zero. In the 50 μm channel, a significant increasing trend in μ_0 is found for 10% PBS ($p = 0.00460$), 5% plasma ($p = 0.0444$), and 20% plasma ($p = 0.00380$). In contrast, in the 25 μm channel, significant increases are observed only for 5% PBS ($p = 0.0376$) and 5% plasma ($p = 0.0366$), suggesting that the dependency of μ_0 on PG_{exp} is more prominent in the larger microchannel. Ht variations also influences the μ_0 trends, with lower Hts (5% and 10%) showing more statistically significant increases in both channels.

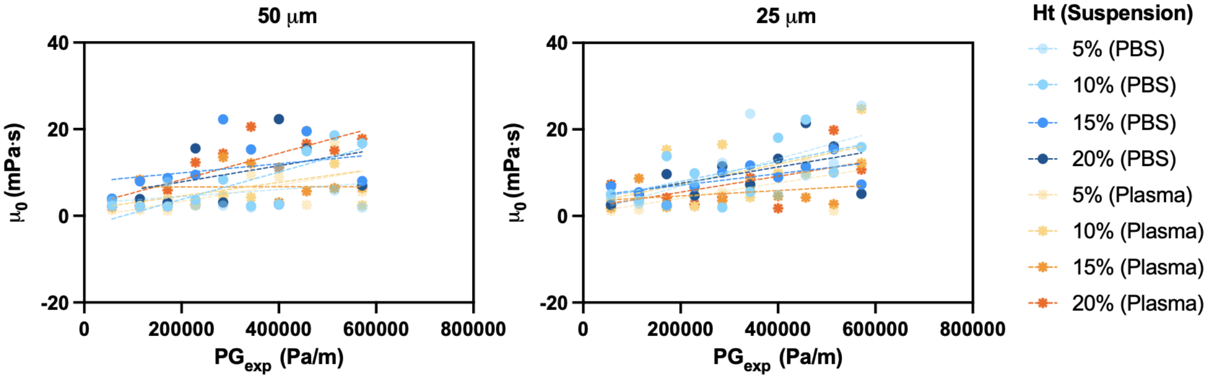

Figure 4.6: Comparison of Carreau Model's zero viscosity (μ_0) trends across different Ht and suspensions in 50 μm (left) and 25 μm (right) channels. Model against pressure gradient (PG_{exp}) and fitted using simple linear regression for visualization.

As for the infinite-shear trends, Figure 4.7 presents the infinite-shear viscosity (μ_∞) as a function of experimental pressure gradient (PG_{exp}) for the same conditions. In the 50 μm channel, a significant decreasing trend in μ_∞ is observed for 5% PBS ($p = 0.00340$), 10% PBS ($p = 0.0398$), 5% plasma ($p = 0.0163$), 15% plasma ($p = 0.0090$), and 20% plasma ($p = 0.0122$). In contrast, in the 25 μm channel, all suspensions exhibit a statistically significant decrease in μ_∞, with the most pronounced effect observed for 5% PBS

($p = 0.0022$). Comparing channel sizes, the 25 μm microchannel shows a more uniform decrease in μ_∞ across all conditions. Suspension type also plays a critical role, with plasma suspensions consistently showing more pronounced decreases in μ_∞ than PBS, particularly in the 50 μm channel at higher Hts.

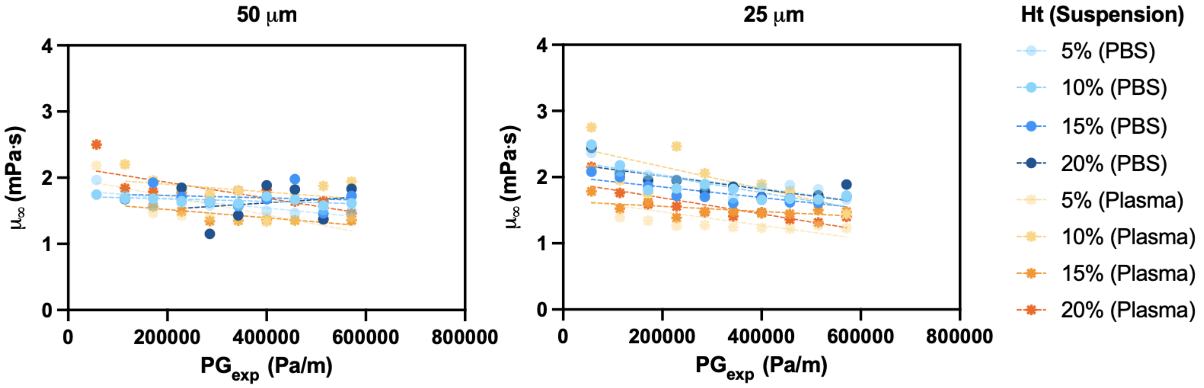

Figure 4.7: Comparison of Carreau Model's infinite viscosity (μ_∞) trends across different Ht and suspensions in 50 μm (left) and 25 μm (right) channels. Modeled against pressure gradient (PG_{exp}) and fitted using simple linear regression for visualization.

POWER LAW

Figure 4.8 presents the trends in the consistency index (K_p) and flow behavior index (n_p) for different Ht and suspensions across 50 μm and 25 μm microchannels. Simple linear regression is used to evaluate the significance of observed trends. The flow behavior index n_p exhibits an increasing trend across most conditions. In the 50 μm channel, this effect is significant for 5% PBS ($p = 0.0025$), 5% plasma ($p < 0.0001$), and 15% plasma ($p = 0.0494$). In the 25 μm channel, n_p increases significantly across most conditions, with the strongest trend observed for 15% PBS ($p = 0.00010$). Conversely, For the consistency index K_p, a decreasing trend is observed across some conditions. In the 50 μm channel, significant decreases are found for 5% PBS ($p = 0.00080$) and 5% plasma ($p = 0.0035$). In the 25 μm channel, significant reductions in K_p are noted for 10% plasma ($p = 0.00070$) and 20% plasma ($p = 0.00810$), suggesting that higher Ht plasma suspensions exhibit more pronounced effects in smaller channels.

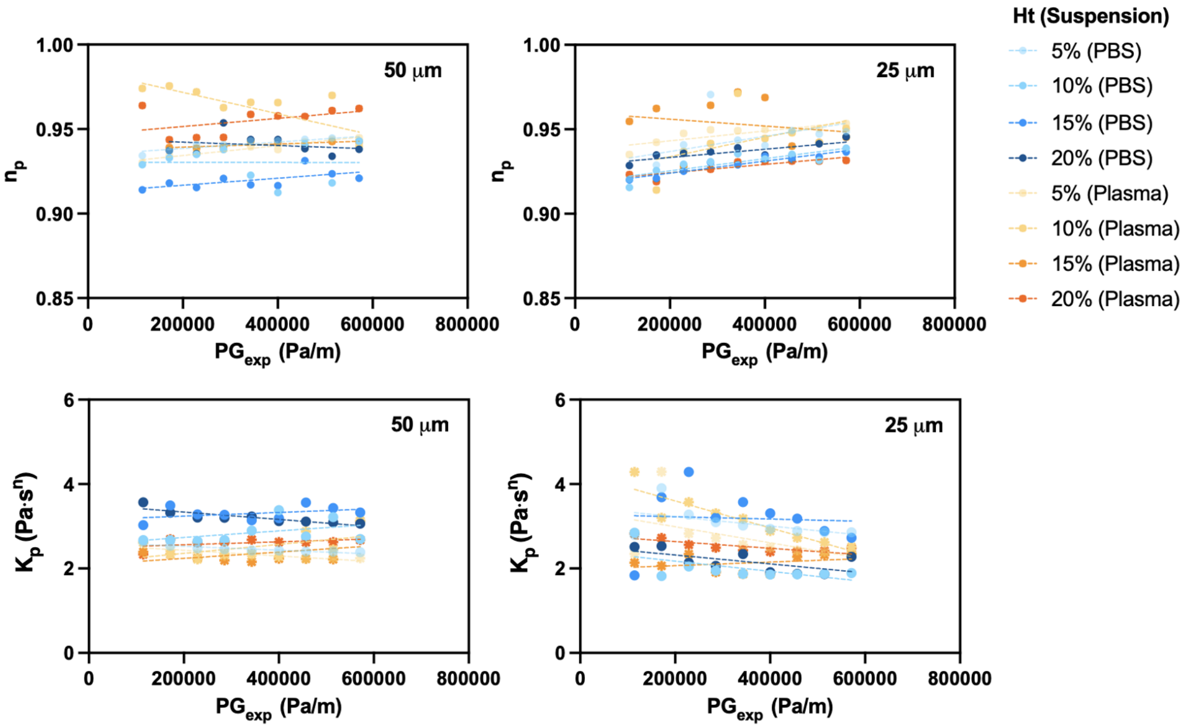

Figure 4.8: Power Law Model parameters across varying hematocrit levels (Ht), suspensions, and channel sizes. (Top panel) Flow behavior index n_p as a function of the experimental pressure gradient (PG_{exp}) for the 50 µm and 25 µm channels, respectively. (Bottom panel) Consistency index K_p as a function of PG_{exp} for the 50 µm and 25 µm channels, respectively. Simple linear regressions are applied for visualization.

DOUBLE-PARAMETER POWER FIT

The parameters k_1 and k_2 exhibit distinct trends across different channel sizes and suspensions. In the 50 µm channel, k_1 demonstrates an overall decreasing trend with increasing pressure gradient, with significant reductions observed for PBS at 5% and 10% Ht ($p = 0.0172$ and 0.00040, respectively) and plasma at 10% Ht ($p = 0.00020$). Conversely, in the 25 µm channel, k_1 shows an increasing trend, particularly significant for PBS at 20% Ht ($p = 0.0120$) and plasma at 5% and 20% Ht ($p = 0.00020$ and 0.0378, respectively). The wall bluntness parameter, k_2, exhibits a stable or slightly decreasing trend in the 50 µm channel, with a significant decrease for PBS at 10% Ht ($p = 0.00880$) and plasma at 10%, 15%, and 20% Ht ($p = 0.00140$, 0.0313, and 0.00140, respectively). In the 25 µm channel, k_2 follows a stronger decreasing trend, with significant changes for PBS at 20% Ht ($p = 0.00380$) and plasma at 5% and 20% Ht ($p = 0.00050$ and 0.0177, respectively). The larger k_1 values in PBS compared to plasma suggest a more pronounced core bluntness in non-aggregating suspensions. The opposite effect can be seen for k_2 , most clearly in the 25 µm channel, where plasma generally exceeds PBS.

Core-Plasma

Figure 4.10 presents the trends of the Core-Plasma Model parameters, namely the consistency index (K_{cp}) and the flow behavior index (n_{cp}), as a function of the computed pressure gradient (PG_{cp}). In both channel sizes, overall, the K_{cp} and n_{cp} show no significant trend. Statistical analysis from the simple linear regressions indicates that most trends are not statistically significant (ns, $p > 0.05$), except for specific cases in plasma suspensions. For the 50 μm channel, K_{cp} did not show significant variations, except for 20% Ht in plasma

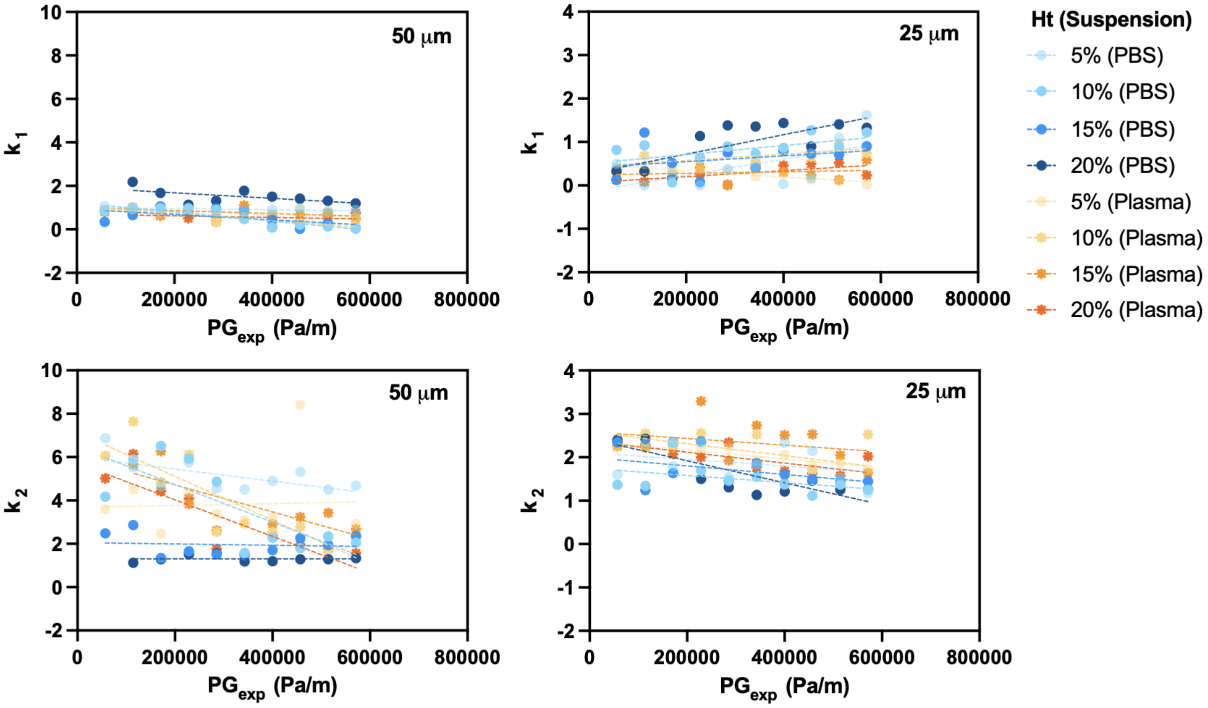

Figure 4.9: Variation of the Double-Parameter Power (DPP) Fit parameters k_1 (core bluntness) and k_2 (wall bluntness) with experimental pressure gradient (PG_{exp}) for RBC suspensions in PBS and plasma. Simple Linear regressions are applied for visualization.

suspensions (p = 0.0185), where a notable decline is observed. Similarly, n_{cp} exhibits ns variations for most cases, with the exception of 20% plasma (p = 0.0179). For the 25 μm channel, K_{cp} and PG_{cp} is statistically significant only for 5% Ht in plasma suspensions (0.0365 and 0.0030), where a slight increase is detected.

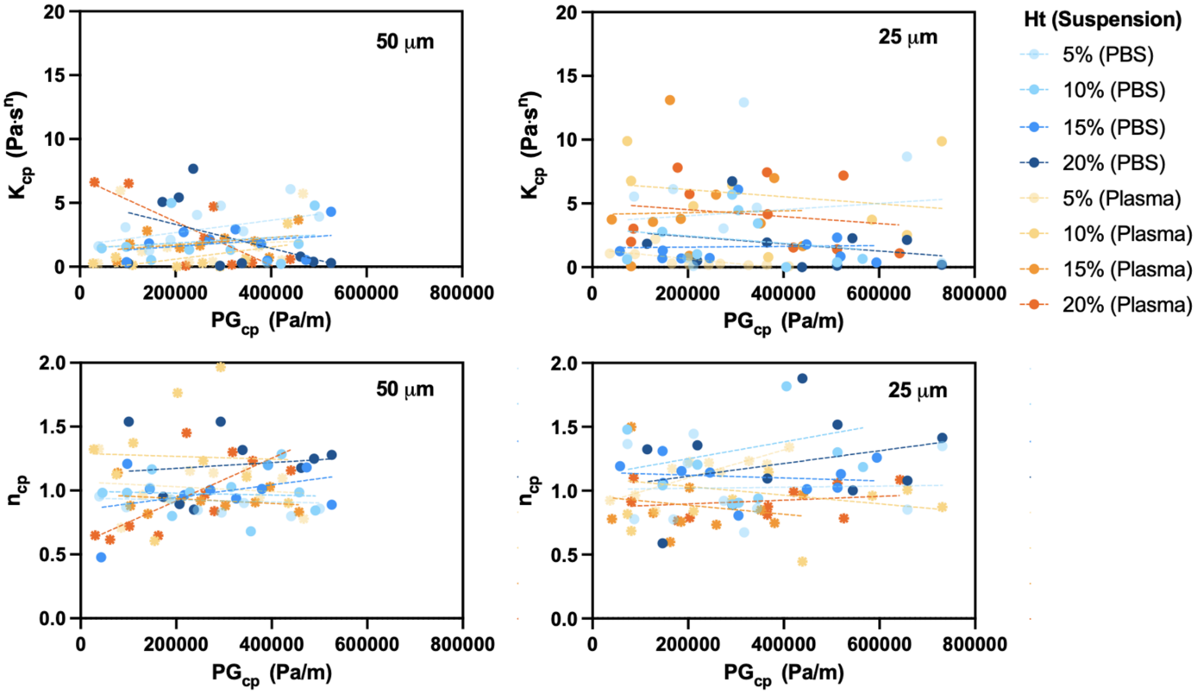

Figure 4.10: Core-Plasma Model parameter trends for consistency index (K_{cp}) and flow behavior index (n_{cp}) as a function of the optimized pressure gradient (PG_{cp}). (Top panel) K_{cp} trends for 50 μm and 25 μm channels, respectively. (Bottom panel) n_{cp} trends for 50 μm and 25 μm channels, respectively. Simple linear regression is applied, with most cases showing no statistical significance.

4.1.3 Comparison of Optical and Hydrodynamic CFL Measurements

The CFL thickness is evaluated using both optical (δ_o) and hydrodynamic (δ_h) methods, revealing a distinct transition between the RBC-dominated core and the near-wall plasma-rich region. The scatter plots in Figure 4.11 demonstrate a general trend where δ_o exceeds δ_h in most cases, particularly in the 50 μm channel, indicating that the optical method tends to measure a thicker CFL than the hydrodynamic approach. Also, the 50 μm channel has fewer data points deviating significantly from the $\delta_o = \delta_h$ equality line.

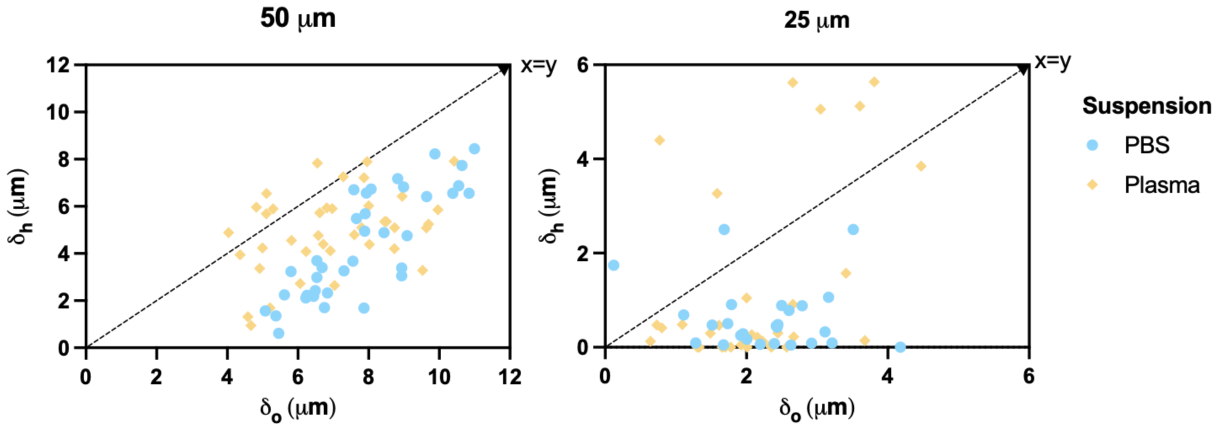

Figure 4.11: Comparison between optical and hydrodynamic cell-free layer (CFL) thicknesses (δ_o and δ_h) in microchannels of 50 μm (left) and 25 μm (right) diameters for RBC suspensions in PBS (blue) and plasma (yellow). The dashed line represents the $x = y$ equality line, indicating where $\delta_o = \delta_h$. Data points above this line suggest a thicker hydrodynamic CFL relative to the optical measurement, whereas points below indicate the opposite.

Figure 4.12 provides a statistical comparison, confirming that δ_o is significantly greater than δ_h across all conditions. A one-way ANOVA with Sidak's multiple comparison test is performed, as described in Section 3.5. In the 50 μm channel, the median δ_o is 7.89 μm (PBS) and 6.91 μm (plasma), while δ_h is 4.76 μm (PBS) and 5.09 μm (plasma). In the 25 μm channel, CFL thickness is significantly lower, with median δ_o values of 1.12 μm (PBS) and 1.15 μm (plasma), while δ_h further decreased to 0.524 μm (PBS) and 0.825 μm (plasma). The p-values indicate strong statistical significance ($p < 0.0001$) for all comparisons, except for the 25 μm plasma condition, which shows a slightly weaker significance ($p = 0.00650$). These results highlight that channel size and suspension type influence CFL measurement, with the 50 μm channel showing greater differences between δ_o and δ_h.

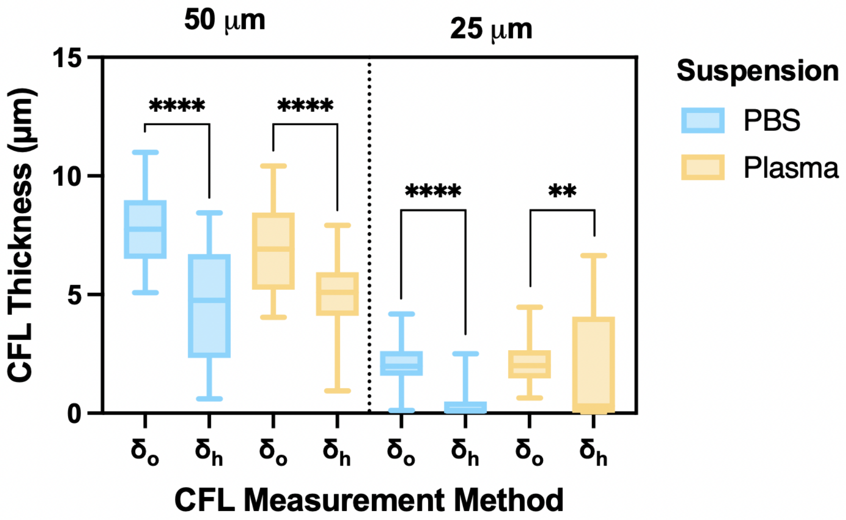

Figure 4.12: Comparing CFL thickness methods, optical(δ_o, teal) and hydrodynamic (δ_h, orange) across varying suspension types (PBS and plasma) in 50 µm (left panel) and 25 µm (right panel) channels. A one-way ANOVA with Sidak's multiple comparison test is performed. Statistical significance is indicated as follows: p-value < 0.01 (**) and < 0.0001 (****).

4.2 Discussion

The discussion section interprets and critically analyzes the findings obtained from various rheological models and fits, focusing particularly on their performance and the behavior of non-Newtonian parameters. Each is assessed in terms of accuracy, strengths, and limitations, particularly regarding their capability to represent blood flow dynamics accurately in microcirculatory environments. Furthermore, a detailed evaluation is presented to determine the most optimal CFL measurement approach.

4.2.1 Strengths and Limitations of Rheological Models and Fits

The **DPP Fit** exhibits the strongest performance in fitting the velocity profiles across both the 25 µm and 50µm channels, effectively capturing bluntness near the axis and core of the channel. Despite its superior fit quality, the DPP Fit is an empirical fitting rather than a rheological model derived from physical laws. This reduces its effectiveness in reliably modeling blood flow behavior under various physiological conditions and different vessel sizes.

Among rheological models, the **Core-Plasma Model** stood out, especially in the 50 µm channel. Its strength lies in explicitly accounting for the phase separation between the RBC-rich core and the near-wall plasma region, which enables it to accurately represent discontinuities in shear rate. However, its advantage diminishes in the 25 µm channel, likely due to the decreased CFL thickness and higher RBC confinement, conditions that blur the clear two-phase separation essential for the optimization of this model.

Intermediate performance is noted for the **Power Law Model** and the simple **Newtonian** approximation, both showing moderate fitting accuracy compared to the DPP Fit and Core-Plasma Model. While the Power Law Model provides reasonable predictions, it inherently simplifies blood flow by using a continuous viscosity without accounting for the effects of the CFL. Similarly, the Newtonian Model, with its assumption of constant viscosity, is predictably less effective in capturing non-Newtonian effects, particularly at low shear rates and high RBC concentrations, but served as a useful baseline for comparison.

In contrast, the **Carreau Model** consistently has poorer performance across both channel sizes. This discrepancy is likely due to the limited shear rate range captured in our Model. As seen in Chapter 2, Figure 2.6, blood viscosity spans several orders of magnitude in response to varying shear rates, from near-zero values to several hundred or even thousands of reciprocal seconds in high-shear regions. However, our experimental setup only represents a narrow segment of this broader shear rate spectrum, particularly in the mid-to-high shear range found inside the channel. Since the Carreau Model is designed to describe viscosity across a much wider range—including both low- and high-shear regimes—it may fail to fully capture the behaviour of blood in our setup.

Overall, for accurately fitting experimental velocity profiles, the DPP Fit is most effective. However, for researchers aiming to extract meaningful rheological parameters and better capture physical behavior of blood flow, the Core-Plasma Model provides the best performance. A more detailed look into the rheological parameters obtained from each Model will be discussed in the next section.

4.2.2 Interpretation of Non-Newtonian Parameters

This section analyzes the extracted parameters from experimental, Carreau, Power Law, DPP Fit, and Core-Plasma Models, comparing their effectiveness in characterizing non-Newtonian blood flow.

Apparent Viscosity Trends

The results from Figure 4.4 indicate that, overall, PBS suspensions exhibit higher apparent viscosity than plasma suspensions. This outcome is counterintuitive, as we would typically expect PBS to yield a lower viscosity and plasma to exhibit a higher viscosity due to red blood cell aggregation, consistent with findings from viscometer studies [8, 28]. However, this discrepancy suggests that an additional factor may be influencing the results. One possible explanation is the role of the CFL, which may be more pronounced in plasma suspensions, leading to an effective reduction in viscosity near the walls. The presence of plasma proteins, such as fibrinogen, promote RBC aggregation in plasma suspensions [11]. Conversely, PBS lacks aggregation-promoting proteins, resulting in a more dispersed RBC configuration which can higher viscosity [16]. Notably, the slopes are steeper in the 50 μm channel compared to the 25 μm channel, indicating that viscosity is more pressure-dependent in larger microchannels. Some studies have shown that the CFL is thicker in larger channels [4, 8], leading to greater shear stress redistribution, which influences how viscosity changes with pressure.

Carreau Model Trends

The results highlight key limitations of the Carreau Model in accurately capturing blood viscosity trends in microchannels. Ideally, μ_0 and μ_∞ should remain constant for a given fluid, independent of pressure-driven flow, yet significant variations are found across different Hts and suspensions, as seen in Figures 4.6 and 4.7. This deviation raises concerns about the Model's applicability in confined microchannel flows, where the shear rate range is much narrower than in bulk rheological studies, as mentioned previously in 4.2.1. Similarly to the apparent viscosity trend, a lower μ_0 and μ_∞ is observed in plasma-based suspensions compared to PBS. This goes back to the theory that RBC aggregation in plasma-suspensions reduces viscosity due to RBC clustering and allows for easier flow alignment, resulting in an overall lower apparent viscosity [16].

Power Law Trends

The Power Law parameters presented in Figure 4.8, in theory, should exhibit minimal variation across different conditions, as it assumes a consistent relationship between shear rate and viscosity without explicit dependence on pressure or channel size. However, our results reveal unexpected variability in the consistency index (K_p) and flow behavior index (n_p), particularly across different Hts and suspensions. This deviation suggests that additional factors, beyond the simple shear-dependent behavior assumed in the Power Law

Model, may be influencing the viscosity trends.

A check is made to determine whether CFL thickness (δ_o) plays a role in the observed variations in the Power Law parameters (K_p and n_p), as shown in Figure 4.13. The plots initially suggested a possible trend, where higher K_p values are associated with smaller δ_o, particularly in the 50 μm channel, while higher n_p values appeared more prominent with larger δ_o. This aligns with the idea that a thicker CFL reduces the effective viscosity in the core region, which could influence the Power Law parameters [16]. However, linear regression analysis found no statistically significant relationship between δ_o and the Power Law parameters when accounting for suspension type and hematocrit. This suggests that CFL thickness alone is not the primary factor driving the observed variations. While the Power Law Model remains a useful approximation for blood rheology, it does not fully account for microstructural factors, which likely contribute to the observed trends.

Double-Parameter Power Fit Trends

Unlike the single-parameter Power Law, the DPP offers the advantage of independently describing the bluntness at the center and near the walls. In the 50 µm channel, the decrease in k_1 (as seen in Figure 4.9) suggests that as shear rate increases, the velocity profile in the center of the channel becomes less blunt, potentially due to aggregates breaking apart. On the other hand, in the 25 µm channel, k_1 increases, meaning that the RBC core becomes more blunt. This could be because the smaller channel confines the RBCs more, promoting aggregation. When the RBCs are more clustered in the center, it can make the velocity profile flatter.

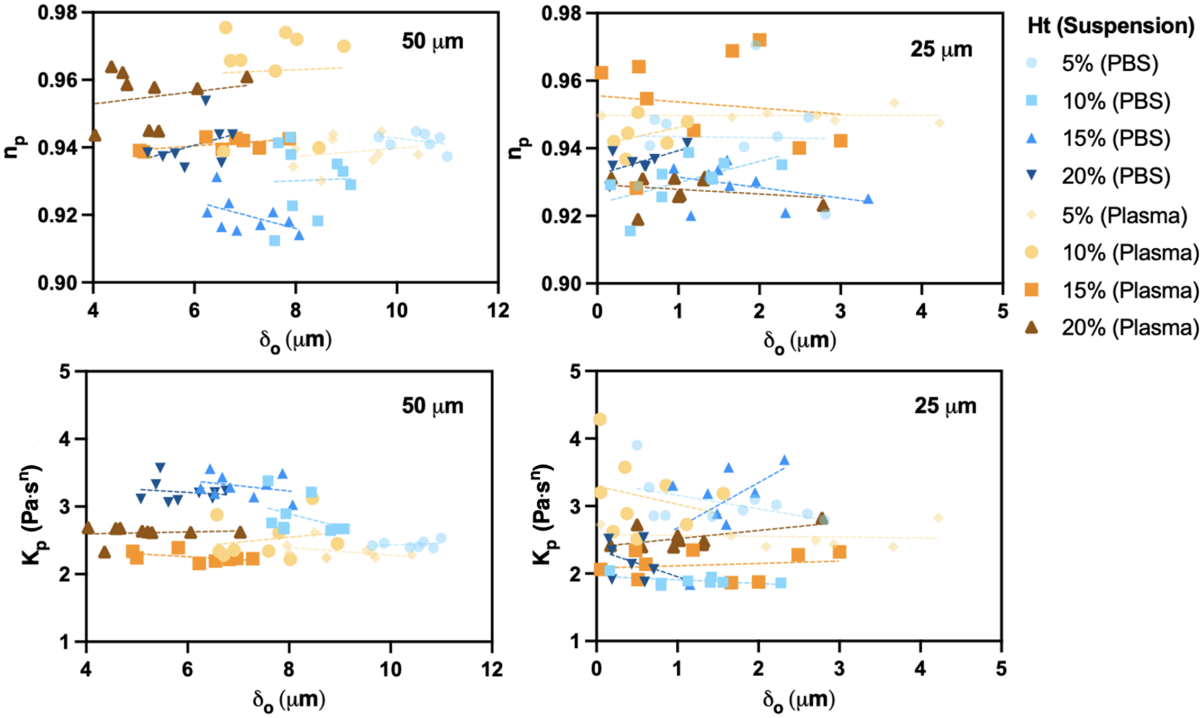

Figure 4.13: Relationship between optical CFL thickness (δ_o) and Power Law Model parameters (K_p and n_p) for microchannels of 50 μm (left) and 25 μm (right) diameter. The top row shows δ_o versus n_p (flow behavior index), while the bottom row shows δ_o versus K_p (consistency index). Data points are categorized by hematocrit (Ht = 5%, 10%, 15%, 20%) and suspension type (PBS or plasma). Fitted using simple linear regression, all indicating no significance (ns).

Regarding k_2, which describes velocity behavior near the walls, both channel sizes show a general decreasing trend, implying that the velocity profile near the walls smooths out as shear rate increases. This effect is more pronounced in plasma suspensions, where RBC aggregation initially results in a blunter near-wall profile that becomes more uniform under increasing shear rate.

Interestingly, these trends in k_1 and k_2 are observed only in some cases, while others are not significant (ns). Given that we would typically expect to see no trend across all cases, this selective significance suggests that the presence of a CFL may influence core and wall bluntness.

Core-Plasma Trends

The Core-Plasma Model distinguishes itself by explicitly modeling the two-phase nature of blood flow—capturing both the RBC-rich core and the plasma-rich CFL near the walls. Interestingly, in Figure 4.10, even though the experimental data had considerable variability, the Core-Plasma Model parameters—consistency index (K_{cp}) and flow behavior index (n_{cp})—show no significance (ns) in both the 50 µm and 25 µm channels. This suggests that these parameters might reflect fundamental characteristics of RBC suspensions, influenced mainly by the intrinsic properties of RBCs and plasma rather than by the channel size. In simpler terms, the model seems to capture a consistent overall behavior of the RBC core and the plasma interaction near the walls, regardless of how confined the vessels are. Although local flow details may differ between channel sizes, the Core-Plasma Model parameters likely represent intrinsic rheological properties of blood rather than specific confinement effects. The little to no statistical significance observed implies that factors beyond just Ht—such as local RBC clustering and variations in shear rate conditions—may also significantly affect these parameters.

It is also important to consider that the imposed pressure gradient (PG_{cp}) in this model is the experimental PG, and the computation adjusts to compensate for the simplified viscosity assumption in the plasma region. Since the viscosity in the plasma-rich CFL is not directly measured but rather assigned based on a simplified assumption, the PG adapts to this imposed condition rather than reflecting the true viscosity distribution. This limitation could introduce deviations between the model and experimental data, particularly in predicting shear-dependent effects near the walls. Future work should focus on obtaining direct measurements of viscosity in plasma to evaluate whether incorporating a more accurate viscosity distribution could further improve the model's predictive performance.

4.2.3 Accuracy and Reliability of CFL Measurements

The comparison between optical (δ_o) and hydrodynamic (δ_h) CFL measurements (Figure 4.11 and Figure 4.12) highlights the advantages and limitations of each method. Optical measurements, obtained through high-speed imaging and image processing, provides a more consistent and reliable representation of CFL thickness across varying conditions. This method has the advantage of allowing visual verification and inspection by an expert, ensuring accuracy and confidence in the result. In contrast, the hydrodynamic method, derived from μPIV velocity profiles, consistently underestimates CFL thickness. This discrepancy is likely due to inherent limitations of μPIV, including depth of correlation effects or out-of-plane motion, all of which reduce accuracy in detecting the sharp velocity gradient at the CFL-core interface (see Appendix A.1 for more detail) [44, 45]. Moreover, the boundary between the plasma and RBCs is not sharply defined; instead, there is a transitional region where cells continuously move in and out. This movement creates a 'blurry' interface that could potentially mislead velocity and viscosity measurements.

While μPIV remains a valuable tool for analyzing velocity fields and shear rate distributions, these findings suggest that hydrodynamic estimations may be less reliable. Although it is interesting to see the clear discontinuity in the data, for the purpose of microvascular flow studies requiring precise CFL quantification, optical measurements should be prioritized for greater accuracy.

Chapter 5

Evaluating Cell-Free Layer Influencing Factors

5.1 Results

This chapter aims to address contradictions in the existing literature concerning the primary mechanisms governing CFL formation. Specifically, the effects of Ht, shear rate gradient, and shear stress on CFL thickness are systematically investigated to identify dominant influencing factors. The aim is to contribute to the development of CFL thickness models. Optical CFL measurements, previously recommended in Section 6.1, will be utilized for this evaluation.

5.1.1 Impact of Hematocrit

The statistical analysis of the optical CFL thickness, δ_o, across different Ht (5%, 10%, 15%, and 20%) and suspension types (PBS and plasma) in both 50 μm and 25 μm microchannels reveals significant variations, as illustrated in Figure 5.1. A one-way ANOVA with Sidak's multiple comparison test is performed, as described in Section 3.5, to assess these differences.

In the 50 μm channel, δ_o in PBS suspensions exhibits a significant decreasing trend with increasing Ht. Significant differences are observed between 5% vs. 10%, 5% vs. 15%, and 5% vs. 20% (all $p < 0.001$), as well as between 10% vs. 15% ($p = 0.00040$), 10% vs. 20% ($p < 0.0001$), and 15% vs. 20% ($p = 0.0113$). This trend suggests a progressive reduction in δ_o with increasing Ht. Plasma suspensions followed a similar pattern, with significant differences observed between 5% vs. 10% ($p = 0.0040$), 5% vs. 15% ($p < 0.0001$), and 5% vs. 20% ($p < 0.0001$). Additional significance is found for 10% vs. 20% ($p = 0.00680$) and 15% vs. 20% ($p < 0.0090$). While the overall significance between Ht levels in plasma suspensions is slightly lower compared to PBS, the decreasing trend in δ_o is still apparent. When comparing the same Ht levels between suspension types, PBS suspensions at 5% Ht exhibits significantly greater δ_o compared to plasma, whereas this difference diminishes at higher Ht levels.

In the 25 μm channel, the reduction in channel diameter further reduces δ_o, as expected. For PBS suspensions, no significant differences are observed between 5% vs. 10%, 5% vs. 15%, and 5% vs. 20% (all $p > 0.05$), though a significant difference is found between 15% vs. 20% ($p = 0.00510$). Plasma suspensions showed significant differences between 5% vs. 10% ($p < 0.0001$) and 5% vs. 20% ($p = 0.00230$), while other comparisons are not statistically significant. Additionally, comparing the same Ht levels between PBS and plasma suspensions in the 25 μm channel reveals no significant differences, suggesting that the influence of suspension medium on δ_o diminishes as channel size decreases.

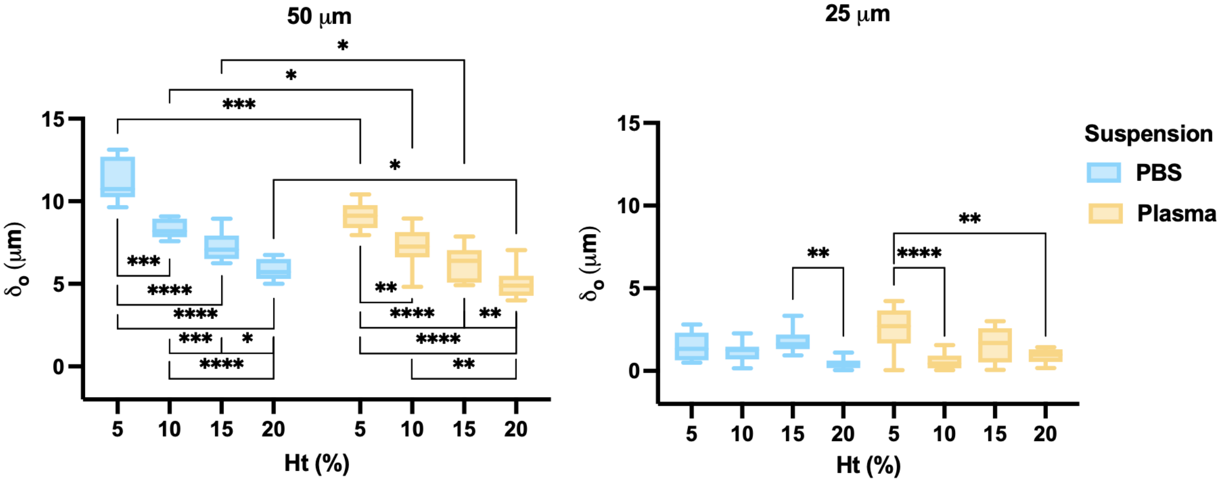

Figure 5.1: Comparison of the optical CFL, δ_o, across different hematocrit (Ht) levels (5%, 10%, 15%, and 20%) for PBS (blue) and plasma (yellow) suspensions in microchannels of 50 μm (left) and 25 μm (right) width. A one-way ANOVA with Sidak's multiple comparison test is performed. Box plots represent the distribution of CFL thickness, with statistical significance indicated by asterisks: * ($p < 0.05$), ** ($p < 0.01$), *** ($p < 0.001$), and **** ($p < 0.0001$). Comparisons with no asterisks indicates no significance.

5.1.2 IMPACT OF GRADIENT OF SHEAR RATE

The shear rate used for this analysis is the shear rate at the discontinuity ($\dot{\gamma}$), which quantifies the rate of deformation at the boundary between the RBC core and the CFL. As defined in Methods section 3.4.2, it is obtained by calculating the velocity gradient at the interface position. This value represents the final shear rate within the RBC core before transitioning into the CFL, marking the shift from a non-Newtonian to a Newtonian regime. To investigate the influence of shear dynamics on δ_o, we analyze its relationship with both shear rate ($\dot{\gamma}$) and shear rate gradient ($\nabla\dot{\gamma}$) across different Ht (10%, 15%, and 20%) and suspension types (PBS and plasma), as shown in Figures 5.2 and 5.3, respectively. 5% is neglected in the analysis for consistently having no significance. A simple linear regression is applied for visualization of the trends.

In the 50 μm PBS suspension, δ_o decreases with increasing shear rate, showing significant correlations at 10% ($p = 0.0206$) and 15% ($p = 0.0134$), while 20% Ht displays a weaker trend ($p = 0.0944$). In contrast, the 50 μm plasma suspension exhibits a positive correlation, with a significant increase in CFL at 15% Ht ($p = 0.0080$), whereas 10% and 20% Ht displayed weaker trends ($p = 0.0854, 0.127$). In the 25 μm PBS channel, no significant correlations are observed for any Ht level ($p > 0.05$), whereas in the 25 μm plasma suspension, a significant positive correlation is found at 15% Ht ($p = 0.0170$).

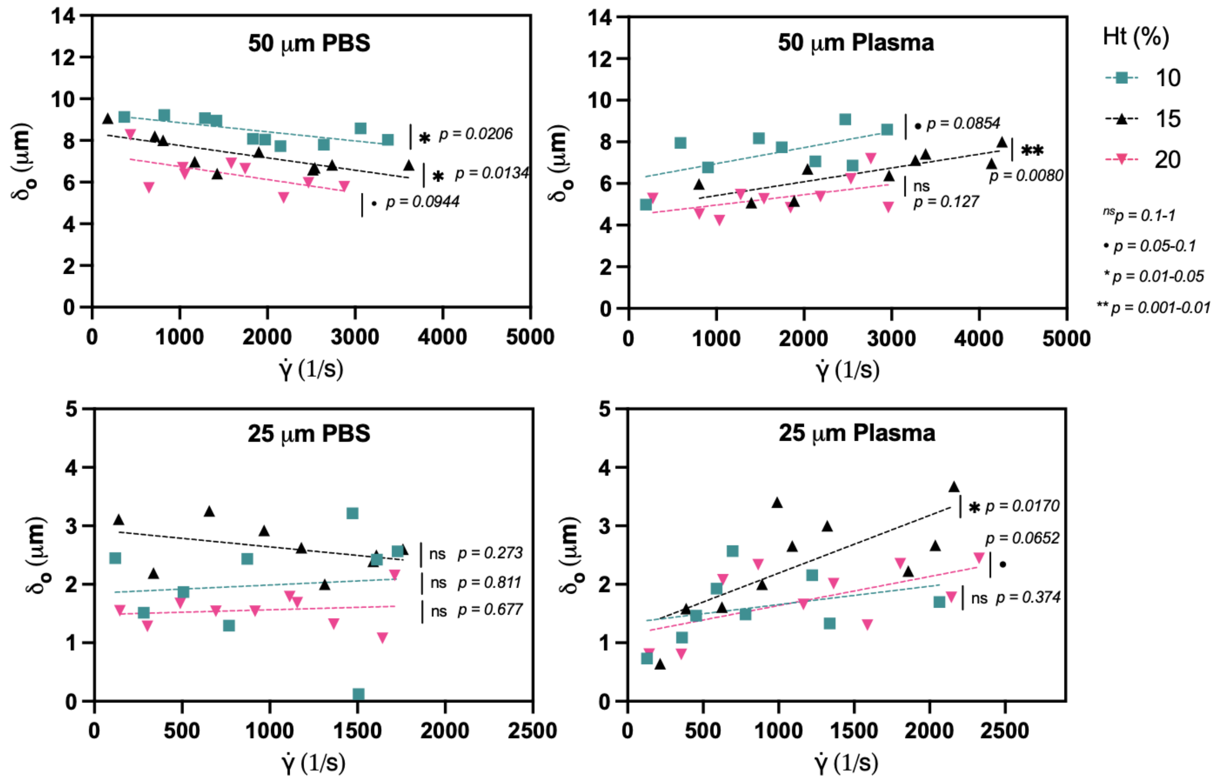

Figure 5.2: Relationship between optical CFL thickness, δ_o, and shear rate at discontinuity ($\dot{\gamma}$, Methods section 3.4.2), for different hematocrit levels (Ht = 10%, 15%, 20%) in PBS (left) and plasma (right) suspensions for microchannels of 50 μm (top) and 25 μm (bottom) widths. Simple linear regressions are performed. Statistical significance levels are indicated: $^{ns}p > 0.05$, $^{\bullet}p = 0.05 - 0.1$, $^{*}p = 0.01 - 0.05$, and $^{**}p = 0.001 - 0.01$.

Similarly to the $\dot{\gamma}$, the $\nabla\dot{\gamma}$ reflects the rate of change in shear stress near the RBC core-CFL boundary (as described in Methods section 3.4.2). When analyzing δ_o versus $\nabla\dot{\gamma}$, the 50 μm PBS suspension again shows a decreasing trend, with significant correlations at 10% ($p = 0.0114$) and 15% ($p = 0.0190$), while the 20% Ht trend is weaker ($p = 0.0943$). In the 50 μm plasma suspension, CFL increases with $\nabla\dot{\gamma}$, with a highly significant correlation at

15% ($p = 0.0026$), while 10% and 20% Ht exhibits moderate trends ($p = 0.0668, 0.0942$). The 25 μm PBS channel shows no significant correlation for δ_o versus $\nabla\dot{\gamma}$ ($p > 0.05$), whereas in the 25 μm plasma suspension, a strong correlation is found at 15% Ht ($p = 0.0013$), with weaker trends at 10% and 20% ($p = 0.0630, 0.344$). Comparing the statistical

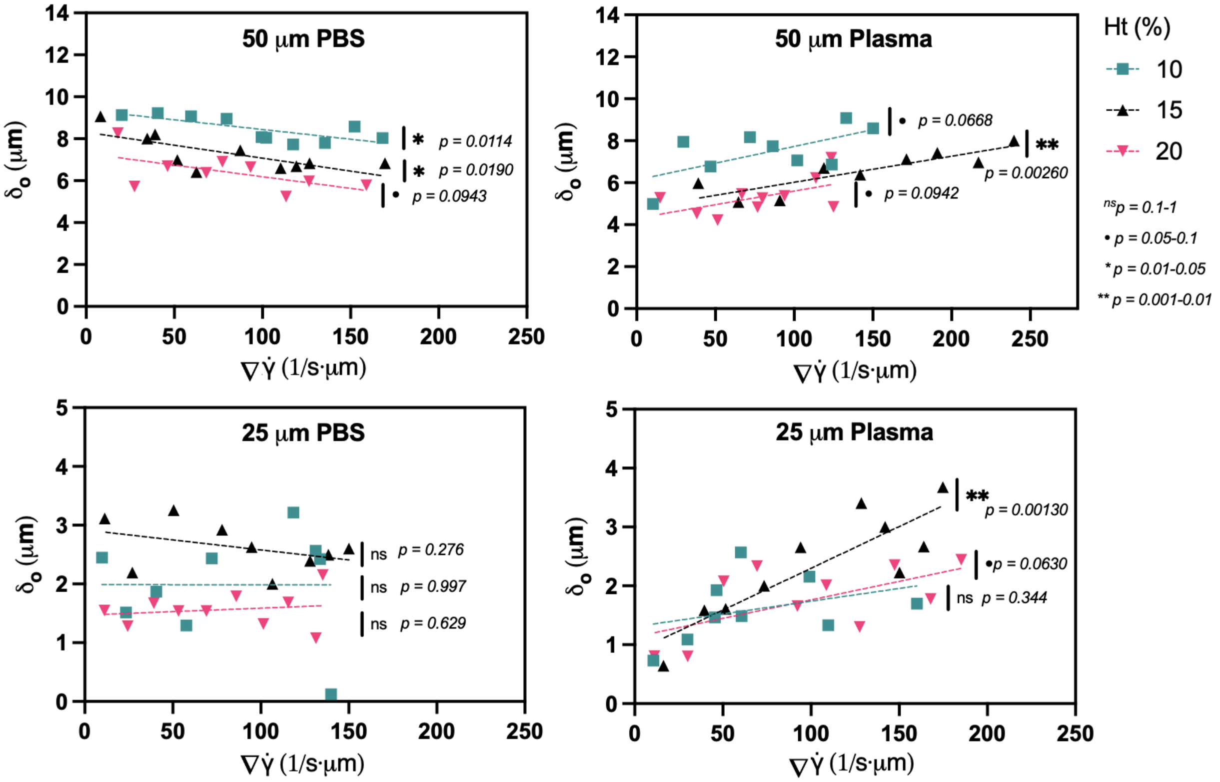

Figure 5.3: Relationship between optical CFL thickness, δ_o, and shear rate gradient ($\nabla\dot{\gamma}$, Methods section 3.4.2), for different hematocrit levels (Ht = 10%, 15%, 20%) in PBS (left) and plasma (right) suspensions for microchannels of 50 μm (top) and 25 μm (bottom) widths. Simple linear regressions are performed. Statistical significance levels are indicated: $^{ns}p > 0.05$, $^{\bullet}p = 0.05-0.1$, $^{*}p = 0.01-0.05$, and $^{**}p = 0.001-0.01$.

significance between δ_o vs. $\dot{\gamma}$ and δ_o vs. $\nabla\dot{\gamma}$, the latter provides stronger correlations overall, particularly in plasma suspensions. This suggests that spatial variations in shear forces play a greater role in δ_o modulation than absolute shear rate, especially in the 50 μm channel. The most significant effects are observed in 15% Ht plasma suspensions in the 50 μm channel, suggesting that moderate Ht levels maximize the influence of shear rate gradients on CFL formation.

5.1.3 IMPACT OF SHEAR STRESS

The shear stress (τ, Methods section 3.4.2) represents the mechanical stress exerted at the transition between the RBC core and the CFL, where the flow shifts from a non-Newtonian to a Newtonian regime. To examine the role of τ in CFL formation, we analyze its relationship with δ_o across different Ht (10%, 15%, and 20%) in both PBS and plasma suspensions for the 50 μm and 25 μm microchannels, as shown in Figure 5.4. 5% is neglected in the analysis for consistently having no significance. A simple linear regression is applied for visualization of the trends.

In the 50 μm PBS suspension, CFL thickness exhibits a negative correlation with τ, where increasing shear stress decreased δ_o. Statistically significant trends are observed at 10% ($p = 0.0187$) and 15% ($p = 0.0133$) Ht, while 20% Ht showed a weaker trend ($p = 0.0594$). In contrast, the 50 μm plasma suspension exhibits a positive correlation between CFL thickness and τ, with a significant trend at 15% Ht ($p = 0.0125$), whereas 10% and 20% Ht show weaker trends ($p = 0.0693, p = 0.141$). These results suggest that in PBS suspensions, increased shear stress leads to RBC dispersion and δ_o thinning, whereas in plasma suspensions, aggregation effects counteract this trend, promoting RBC migration toward the core.

In the 25 μm PBS suspension, CFL thickness shows no statistically significant correlation with shear stress, with all p-values exceeding 0.05 ($p = 0.270, 0.795, 0.694$ for 10%, 15%, and 20% Ht, respectively). In contrast, the 25 μm plasma suspension exhibits a positive correlation between CFL thickness and τ, with a significant trend at 15% Ht ($p = 0.0161$), while 10% and 20% Ht showed weaker trends ($p = 0.0609, 0.269$). Compared to previous analyses of $\dot{\gamma}$ and $\nabla\dot{\gamma}$, shear stress shows weaker statistical significance overall, particularly in PBS suspensions. The strongest trends in plasma suspensions are observed at 15% Ht, similar to $\dot{\gamma}$ and $\nabla\dot{\gamma}$, but with slightly lower statistical significance.

5.2 DISCUSSION

This discussion section evaluates the influence of hematocrit, shear rate gradient, and shear stress on CFL behavior, directly comparing our findings with existing studies in the literature. The analysis highlights areas of agreement and resolves discrepancies with previous research, clarifying the dominant factors driving CFL formation. Finally, the implications of these findings for advancing microcirculatory flow modeling are discussed.

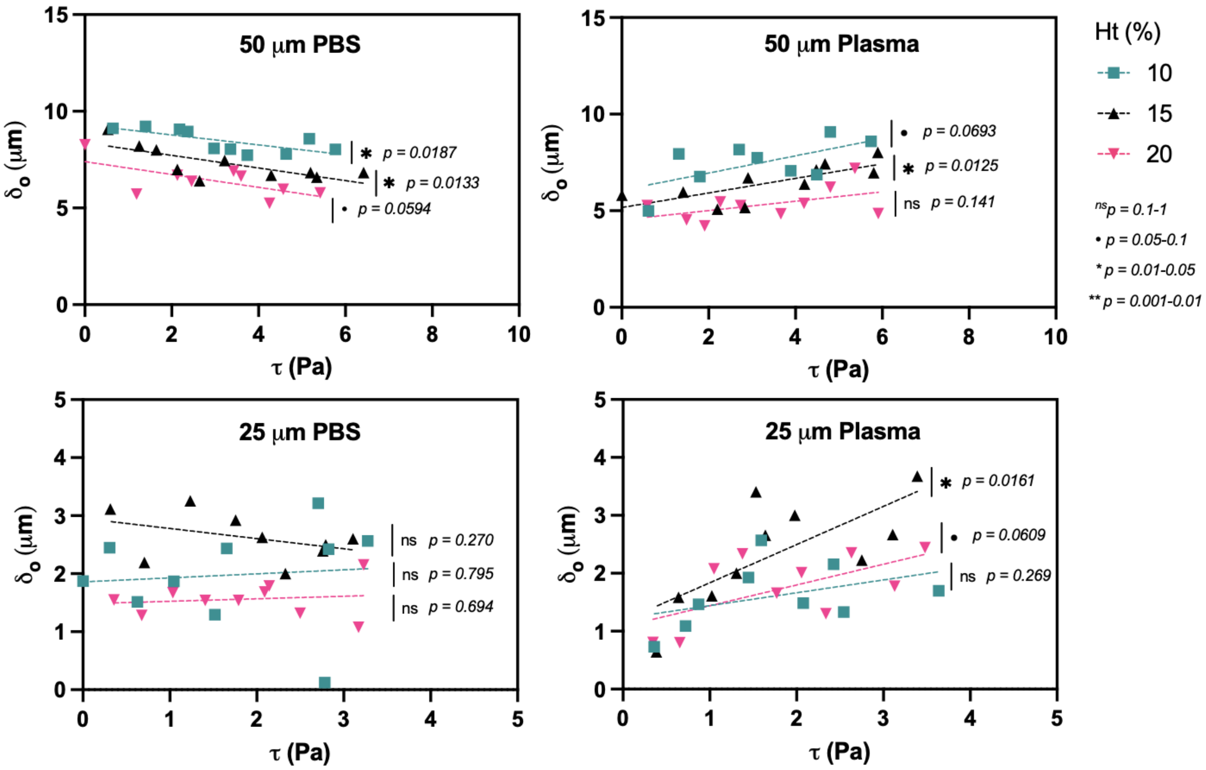

Figure 5.4: Relationship between optical CFL thickness, δ_o, and shear stress (τ, Methods section 3.4.2), for different hematocrit levels (Ht = 10%, 15%, 20%) in PBS (left) and plasma (right) suspensions for microchannels of 50 μm (top) and 25 μm (bottom) widths. Simple linear regressions are performed. Statistical significance levels are indicated: $^{ns}p > 0.05$, $^{\bullet}p = 0.05 - 0.1$, $^{*}p = 0.01 - 0.05$, and $^{**}p = 0.001 - 0.01$.

5.2.1 Hematocrit-Driven CFL Variability

The results of this study align with established literature on CFL formation and reinforce the critical role of hematocrit (Ht) in determining CFL thickness (δ_o). Consistent with the Fåhræus–Lindqvist effect [5], both PBS and plasma suspensions in our experiments exhibit an inverse relationship between δ_o and Ht, confirming prior findings that increasing RBC concentration reduces the plasma-rich region near vessel walls [7, 8]. This trend was observed across both channel sizes but was more pronounced in the 50 μm channel, where RBCs had greater freedom to migrate laterally.

Vessel diameter also plays an important role. The 25 μm channel consistently produced thinner CFLs than the 50 μm channel, in line with reports by Pries et al. (1992) and Cerdeira et al. (2009), who found that geometric confinement in smaller vessels restricts the formation of a distinct CFL [8, 29]. Notably, the 25 μm channel showed less statistical significance in δ_o across Ht levels, suggesting that in highly confined geometries, RBC-wall interactions may limit the impact of hematocrit on CFL thickness.

Our findings are also consistent with the simulations by Katanov et al. (2015), who demonstrated two key trends across vessel diameters from 10 to 100 μm: (i) CFL thickness increases with vessel diameter at fixed Ht, and (ii) CFL thickness decreases with increasing Ht [4]. While their simulations explored hematocrits in the 15–45% range, our study explored a lower regime of 5–20% Ht. At these lower concentrations, we observed more pronounced CFL development—particularly in PBS—likely due to reduced cell-cell interactions and enhanced lateral migration. In contrast, Katanov's higher Ht simulations showed that core crowding at elevated cell concentrations limits migration and suppresses CFL thickness. Together, these findings underscore the importance of examining CFL behavior across a broader hematocrit spectrum, especially under physiologically relevant low-Ht conditions.

5.2.2 Shear Rate Gradient as a Determining Factor

The results of this study indicate that the shear rate gradient ($\nabla\dot{\gamma}$) plays a more significant role in CFL formation than bulk shear rate ($\dot{\gamma}$). Unlike $\dot{\gamma}$, which describes average flow conditions, $\nabla\dot{\gamma}$ captures localized variations in shear that directly influence RBC migration. This observation aligns with previous studies showing that high $\nabla\dot{\gamma}$ near vessel walls generates differential forces that displace RBCs toward the vessel center, thereby promoting CFL formation [26, 33]. In our experiments, δ_o correlates more strongly with $\nabla\dot{\gamma}$ than with $\dot{\gamma}$, especially in plasma suspensions at moderate hematocrit. This reinforces the idea that spatial shear variation, not just bulk flow, governs RBC redistribution—consistent with shear-induced migration theories [26].

While some studies report that high shear rates disrupts RBC clusters and leads to CFL thinning [4], others suggest that moderate shear rates promote aggregation and stabilize CFL formation [6, 7]. Our results support the latter, as we observed that in plasma suspensions, δ_o increased with $\dot{\gamma}$ and $\nabla\dot{\gamma}$, suggesting that at moderate $\nabla\dot{\gamma}$ levels (up to 250 1/s-μm) and $\dot{\gamma}$ levels up to 4200 1/s, aggregation is reinforced rather than disrupted. Since our experiment follows a different *in vitro* approach, the exact aggregation thresholds may differ from prior studies, but the overall mechanisms remain consistent.

The influence of $\nabla\dot{\gamma}$ is further modulated by the suspension medium and interpretation of the results can be made based on previous studies. In PBS, where aggregation is minimal due to the absence of plasma proteins, RBCs remain deformable and hydrodynamic lift is highly effective at low $\nabla\dot{\gamma}$, leading to enhanced CFL formation. As $\nabla\dot{\gamma}$ increases, frequent RBC collisions reduce lift efficiency and promote shear-induced dispersion, which pushes cells toward the wall and reduces CFL thickness [2, 21]. This is reflected in our PBS results, where higher shear gradients result in thinner CFLs.

In contrast, plasma suspensions exhibit protein-mediated aggregation that alters this behaviour and an interpretation can be made on this basis. At low $\nabla\dot{\gamma}$, RBCs form rouleaux that behave like rigid structures, limiting deformability and impairing hydrodynamic lift [6, 7]. As a result, CFL development is suppressed despite low shear gradients. When $\nabla\dot{\gamma}$ increases, these aggregates begin to disaggregate, restoring single-cell deformability. This reactivation of hydrodynamic lift enables RBCs to migrate away from the wall, increasing CFL thickness [4]. This trend appears in our data as well—CFL thickness initially increases in plasma as shear gradient rises, before plateauing or slightly decreasing as dispersion dominates. Together, these results highlight a complex interplay between hydrodynamic lift, aggregation, and shear-induced dispersion—all governed by $\nabla\dot{\gamma}$. Figure 5.5 presents a schematic interpretation of how $\nabla\dot{\gamma}$ influences RBC distribution and CFL formation.

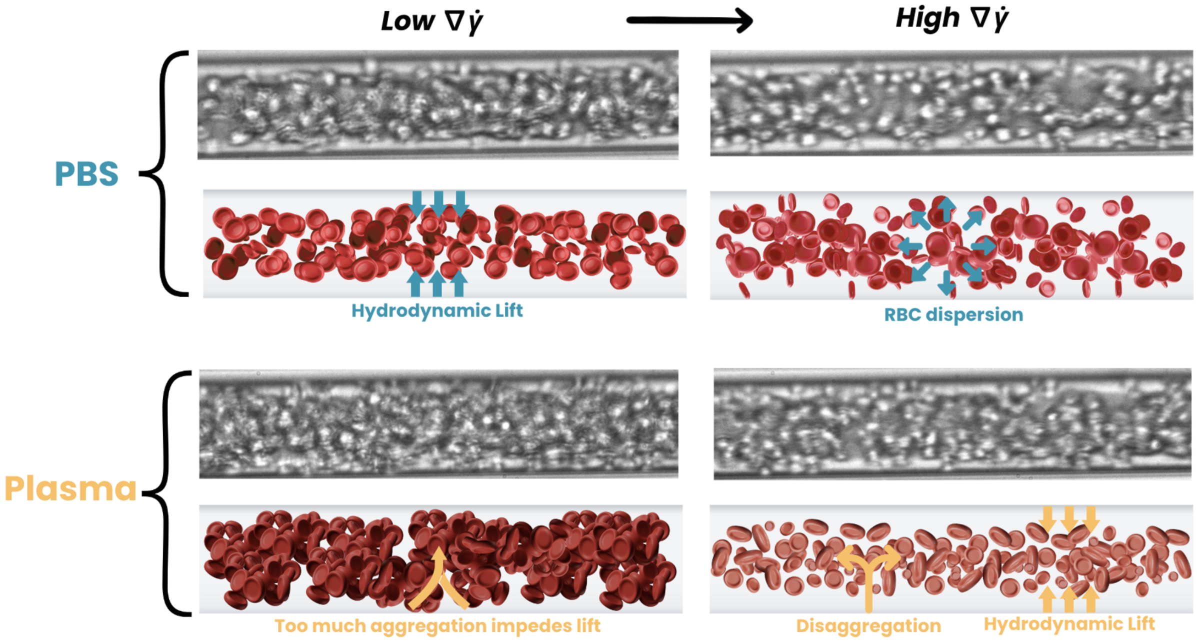

Figure 5.5: Schematic interpretation of the effect of shear rate gradient ($\nabla\dot{\gamma}$) on red blood cell (RBC) distribution and cell-free layer (CFL) formation for 15% hematocrit suspensions in a 50 µm microchannel, under flow pressures of 20 mBar (left) and 200 mBar (right). Top panels correspond to PBS, where in the absence of aggregation, deformable RBCs experience strong hydrodynamic lift at low $\nabla\dot{\gamma}$, leading to enhanced CFL formation. At higher $\nabla\dot{\gamma}$, increased collisions and shear-induced diffusion promote RBC dispersion and reduce CFL thickness. Bottom panels correspond to plasma, where protein-induced aggregation limits lift at low shear gradients by forming rigid rouleaux. As shear gradient increases, these aggregates disaggregate, restoring cell deformability and enabling hydrodynamic lift to drive CFL formation. Overlaid schematics and corresponding microchannel images highlight the distinct behaviors in PBS and plasma. Schematic created using Canva Pro.

5.2.3 Shear Stress, an Insufficient Predictor of CFL

The results of this study indicate that shear stress (τ) is not a primary determinant of CFL formation, as its influence on δ_o is less statistically significant compared to $\dot{\gamma}$ and $\nabla\dot{\gamma}$. In PBS suspensions, δ_o decreases with increasing τ in the 50 μm channel, whereas no significant correlation is observed in the 25 μm channel. Plasma suspensions exhibit a positive correlation between δ_o and τ, particularly at 15% Ht, suggesting that moderate τ enhances RBC aggregation, reinforcing CFL formation. However, compared to $\dot{\gamma}$ and $\nabla\dot{\gamma}$, τ alone did not provide a dominant mechanism for δ_o development, as overall statistical significance is lower across all conditions.

The weaker correlation between CFL and τ aligns with classical theories of shear-induced migration in concentrated suspensions, where particles migrate from regions of high shear rate to regions of low shear due to asymmetric collisions and hydrodynamic interactions [26, 33, 34]. Although these early models were developed for non-Brownian rigid spheres, the underlying principles apply to RBCs, which behave as deformable particles in suspension. In fact, RBCs exhibit even more pronounced migration due to their ability to deform and respond to local flow gradients. These theories have since been extended and validated in RBC-specific studies [2, 24, 25], demonstrating that spatial variations in shear rate—not absolute shear stress—are the dominant driver of RBC redistribution and CFL formation.

5.2.4 Understanding Contradictions in Literature

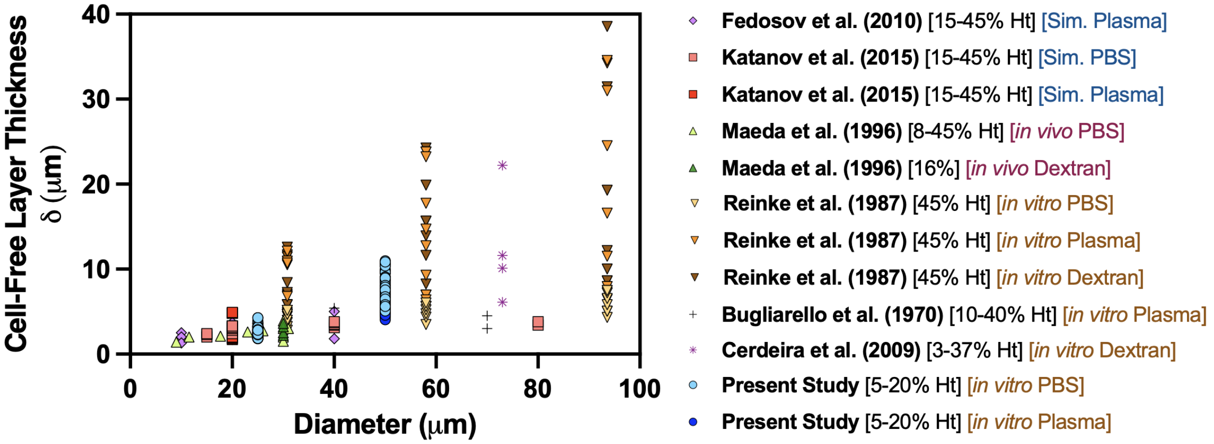

Figure 5.6: Comparison of cell-free layer thickness (δ) as a function of vessel diameter between the present study (5–20% Ht) and selected literature studies. All datasets represent either experimental or simulated blood flow in circular microchannels using human RBCs. Data are color-coded by suspension medium (PBS, plasma, dextran) and labeled with study type (*in vitro*, *in vivo*, or simulation) and hematocrit range [2, 4, 7, 9, 29, 30].

To clarify contradictions in the literature, Figure 5.6 compares cell-free layer (CFL) thickness (δ) across multiple studies that used human blood in circular microchannels. Across most datasets, δ increases with vessel diameter between 10–100 μm, consistent with previously observed trends in Pries et al. (1992) [8]. However, variation in CFL magnitude across studies is substantial, driven by differences in hematocrit, suspension medium, flow conditions, and whether the study was conducted *in vitro*, *in vivo*, or through computational simulation.

Simulations by Fedosov et al. (2010) [2] modeled RBC suspensions in a Newtonian plasma-like fluid using dissipative particle dynamics (DPD). They accounted for deformable

RBCs but did not simulate real protein-induced aggregation. CFL thicknesses reported (2–4 μm for 10–40 μm vessels) were lower than our values. This underestimation may stem from their simplified fluid model, lack of protein interactions, and moderate shear rates (up to 300 s^{-1}) compared to our higher experimental shear range (up to 4200 s^{-1}). Their hematocrit range (15–45%) does not cover the lower Ht regime (5–15%) explored in our study, limiting direct comparison and highlighting the novelty of our data.

In contrast, simulations by Katanov et al. (2015) [4] show closer agreement with our PBS-based values at small diameters. At 25 μm, our CFL thickness aligns well with their 20 μm simulation, likely due to confinement-limited RBC interaction. However, at higher hematocrits and diameters, their CFL values remain lower than ours. This difference can be attributed to their Newtonian solvent assumption (viscosity ratio = 1) and lower pseudo-shear rates (30–350 s^{-1}). In our case, the interpretation is that PBS suspensions at higher shear rate gradients promoted shear-induced dispersion, leading to slightly higher CFLs.

In vivo studies by Maeda et al. (1996) [30], conducted at 16% hematocrit in rabbit mesenteric vessels, evaluated CFL thickness in both elastic (compliant) and hardened (rigid) vessel conditions. Their results showed that CFL thickness was significantly greater in elastic vessels across all diameters tested, with the difference attributed to reduced wall-induced confinement and enhanced RBC migration away from the vessel wall. In contrast, hardened vessels exhibited thinner CFLs due to the lack of compliance and increased confinement. Since our microchannels are made of rigid glass, the comparison is best made with their hardened vessel data—which is what is reflected in Figure 5.6. Notably, our PBS and plasma measurements fall within the same CFL range reported for their rigid condition. This suggests that under strong confinement, differences between suspension media (PBS vs. plasma) become less pronounced, as the ability of RBCs to laterally migrate is limited by the vessel walls.

Among experimental datasets, Reinke et al. (1987) [7] tested RBCs at 45% hematocrit in plasma, PBS, and dextran-based suspensions. They reported CFL thicknesses up to 25 μm in 58 μm channels and 13 μm in 30 μm channels—substantially higher than the values observed in our study. Our results align more closely with their PBS-based data, which lacks protein-induced aggregation. In contrast, their plasma and dextran suspensions followed the classical expectation that aggregation promotes axial migration and thickens the CFL. However, our findings reveal a different trend: in aggregating media, increasing the shear rate gradient reduces CFL thickness. At low gradients, RBCs form stable aggregates that resist lateral migration; at higher gradients, these clusters disaggregate, enhancing hydrodynamic lift and thinning the CFL. This discrepancy is likely due to the different flow regimes. Reinke et al. applied pseudo-shear rates between 0.15 and 100 s^{-1}, with many measurements below 10 s^{-1}—conditions that favor aggregation. In contrast, our experiments reached shear rates up to 4200 s^{-1}, where shear forces are sufficient to disrupt aggregates. These differences in shear environment and larger hematocrit (45%) likely explain why we observed reduced CFL values in plasma.

Bugliarello and Sevilla (1970) [9] also used *in vitro* plasma suspensions but reported notably lower CFL values. This may reflect lower measurement resolution and fewer data points.

Lastly, Cerdeira et al. (2009) [29] used RBCs in dextran-based media (3–37% Ht) within circular PDMS microchannels. Their largest CFL values (25 μm) correspond to the lowest Ht (3%) and largest diameters (80 μm), which are above our experimental range. Despite overlapping Ht values, dextran's strong aggregating potential likely exaggerates CFL thickness, particularly in larger, more compliant channels. Each data point reflects a different Ht, making direct comparisons difficult, but their results emphasize the additive impact of aggregation and vessel size on CFL development.

In conclusion, our findings most closely align with studies conducted under rigid, non-aggregating, high-shear conditions—namely, the hardened vessel data from Maeda and PBS-based simulations by Katanov. Differences with other datasets can be explained by aggregation strength, Ht, and flow regime. These results underscore the importance of jointly controlling hematocrit, suspension medium, vessel compliance, and local shear gradients to accurately characterize CFL behavior.

CHAPTER 6

CONCLUSIONS AND FUTURE WORK

6.1 OPTIMAL MODEL SELECTION FOR MICROVASCULAR BLOOD FLOW

This work presents a detailed comparison of several rheological and fitting models used to describe blood flow in microchannels. Among the evaluated approaches, the Double Power Law (DPP) model emerges as the most accurate purely mathematical fitting model. It consistently provides excellent agreement with experimental velocity profiles across varying microchannel diameters and flow rates. However, because it is not grounded in physiological mechanisms, its predictive value remains limited to empirical settings.

In contrast, the Core-Plasma Model demonstrates strong physical relevance, effectively capturing the essential spatial heterogeneity of microcirculatory flow—namely, the separation between a red blood cell (RBC)-rich core and a plasma-rich cell-free layer (CFL). This model offers meaningful parameters that can be directly related to physiological conditions and vessel geometry, making it well-suited for use in microvascular simulations. It outperforms traditional rheological models, such as the Newtonian and Power Law models, which fail to account for RBC redistribution and spatial transitions in velocity associated with the CFL.

The Carreau model, although commonly applied to blood rheology, performs poorly in microfluidic geometries. Its smooth viscosity transition fails to represent the abrupt shift in velocity observed near the CFL boundary. These findings suggest that despite its popularity, the Carreau model may be fundamentally limited in microchannel flows where confinement effects dominate. The clear underperformance of the Carreau model highlights the need for models that can capture spatial variations in flow, like the Core-Plasma framework.

However, a key limitation of the Core-Plasma Model is its reliance on experimental measurement of CFL thickness (δ), typically obtained through high-speed imaging and manual segmentation. This requirement limits its scalability and general applicability, particularly in computational simulations. Although an alternative method was explored, where the shear rate discontinuity in velocity profiles was used to estimate the hydrodynamic CFL thickness, it proved less effective due to the blurring of the RBC–plasma interface with smaller microchannels, likely caused by imaging limitations. Therefore, an essential next step is to develop a predictive model of CFL thickness that can be embedded into the Core-Plasma Model. Such a coupling would eliminate the dependency on optical measurements and allow for a fully predictive and physiologically grounded flow model. This motivates the second part of this thesis: investigating the governing parameters of CFL formation.

6.2 Unifying Mechanisms Governing CFL Formation

The second major objective of this work is to identify and characterize the primary factors influencing CFL formation. This study confirms that hematocrit (Ht) remains a central determinant of CFL behavior. As Ht increases, the optical CFL thickness (δ_o) decreases, consistent with the well-established Fåhræus–Lindqvist effect [5, 8]. This trend reflects the increased volume fraction of RBCs, which reduces the space available near the vessel wall for a plasma-rich cell-free zone.

Beyond hematocrit, this work provides new insights into the role of shear forces in CFL dynamics. While previous studies report conflicting findings regarding the influence of shear rate ($\dot{\gamma}$) and shear stress (τ), our results demonstrate that the local gradient of shear rate ($\nabla\dot{\gamma}$) is the dominant factor governing CFL formation. By directly measuring local velocity fields and calculating spatial shear gradients, we show that $\nabla\dot{\gamma}$ correlates more strongly with δ_o than either $\dot{\gamma}$ or τ, particularly in plasma suspensions.

The response of CFL thickness to $\nabla\dot{\gamma}$ is strongly media-dependent. Based on existing theories and our experimental observations, we interpret that in plasma, where protein-induced RBC aggregation occurs, δ_o increases with increasing $\nabla\dot{\gamma}$. This behavior is consistent with the idea that local shear gradients promote the disaggregation of rouleaux structures, restore RBC deformability, and reactivate hydrodynamic lift forces that push cells away from the vessel wall. In contrast, under low $\nabla\dot{\gamma}$, aggregated RBCs behave more like rigid bodies, inhibiting lift and suppressing CFL formation.

In PBS, where aggregation is absent, RBCs remain as deformable individual cells. At low $\nabla\dot{\gamma}$, hydrodynamic lift effectively promotes CFL formation. However, as $\nabla\dot{\gamma}$ increases, RBC–RBC collisions intensify, enhancing shear-induced dispersion. This lateral diffusion pushes cells closer to the vessel wall and reduces CFL thickness. Thus, based on these interpretations, the balance between cell-cell and cell-wall interactions appears highly sensitive to local shear rate environments and media composition.

These findings help reconcile longstanding contradictions in the literature. As summarized in Table 2.1, early *in vitro* studies by Fåhræus and Lindqvist (1931) and Pries et al. (1992) emphasize vessel diameter and hematocrit as primary determinants of CFL thickness. More recent simulation studies by Fedosov et al. (2010) and Katanov et al. (2015), however, attribute changes in CFL to variations in flow rate or shear rate. Our results unify these perspectives by demonstrating that $\nabla\dot{\gamma}$ is the critical parameter that modulates both dispersion- and aggregation-related effects. Specifically, they explain why Fedosov et al. report CFL thinning at high shear rates (due to dispersion), while Katanov et al. observe CFL thickening (due to disaggregation and reactivated lift forces).

Furthermore, this study provides experimental validation for emerging theoretical frameworks. Unlike prior studies that rely on bulk or pseudo-shear rate approximations, our approach uses direct image-based velocity measurements in circular microchannels, under controlled *in vitro* conditions. By precisely isolating the effects of hematocrit, flow rate, and medium composition, this work captures microscale dynamics that are often overlooked. These advances mark a significant step forward in refining microcirculatory flow models and enabling physiologically relevant predictions of RBC behavior across a range of hemodynamic conditions.

6.3 Proposal for Future Work

Building on the findings of this study, future work should focus on developing a predictive model for cell-free layer (CFL) thickness that incorporates the gradient of shear rate ($\nabla\dot{\gamma}$), hematocrit (Ht), and suspension-dependent RBC aggregation behavior. Such a model would enable full integration with the Core-Plasma framework, reducing reliance on direct optical measurements. This integration is particularly important for improving the model's applicability in complex microvascular geometries, where spatial heterogeneity in shear rate conditions governs red blood cell (RBC) distribution.

A key open question concerns the behavior of RBC aggregation under high shear rates. While this study confirms that moderate $\nabla\dot{\gamma}$ enhances aggregation in plasma suspensions, it remains unclear whether a critical shear threshold exists at which aggregates begin to disassociate. Future experiments should explore this transition regime to refine current models of shear-induced aggregation and disaggregation, enabling better predictions of non-Newtonian blood rheology under extreme or pathological flow conditions.

Additionally, this study is conducted in rigid microchannels, whereas physiological vessels are elastic. Vessel compliance is known to affect local shear gradients and phase separation. *In vivo* evidence from Maeda et al. (1996) [30] suggests that compliant vessels promote thicker CFLs and lower flow resistance compared to stiffened ones. Future work should explore CFL formation in microchannels with tunable elasticity to determine how vascular compliance modulates $\nabla\dot{\gamma}$, RBC migration, and flow resistance. Incorporating vessel compliance into the Core-Plasma Model would enhance its physiological relevance, especially in disease states where vessel stiffness is altered.

While future modeling efforts aim to reduce dependence on imaging, optical measurement methods should continue to play a central role in validating CFL predictions. High-resolution imaging techniques—such as high-speed microscopy, digital holography, and advanced fluorescent labeling—can offer detailed insight into near-wall plasma layers and RBC distributions. Until robust hydrodynamic estimation of the CFL becomes feasible, these optical approaches remain sufficient for model validation.

Beyond modeling, improved understanding of CFL dynamics has practical implications in biomedical engineering. The CFL plays a critical role in microfluidic transport, acting as a plasma-rich layer that governs solute and drug diffusion near vessel walls. Future research should explore how CFL modulation can be leveraged in drug delivery platforms to enhance therapeutic targeting or in microfluidic diagnostic devices to improve biomarker separation and detection [46]. For instance, devices designed to exploit stable CFL regions may enable plasma extraction without centrifugation, or facilitate localized drug release in vascular beds.

Finally, the insights gained from this work can be extended to pathological conditions such as sickle cell disease, diabetes, and sepsis—where RBC deformability, aggregation, and vessel stiffness are altered. Future studies should investigate how these factors collectively reshape CFL behavior and microvascular resistance. Integrating these mechanisms into advanced blood flow simulators will support the development of personalized medicine tools that are responsive to both physiological variability and disease-specific hemorheology.

APPENDICES

CHAPTER A

SUPPORTING INFORMATION

A.1 MICRO-PARTICLE IMAGE VELOCIMETRY

Micro-Particle Image Velocimetry (µPIV) is an adaptation of macroscopic Particle Image Velocimetry (PIV) designed for velocity measurements in microfluidic flows. The fundamental process of μPIV involves capturing two sequential images of tracer particles at times t and $t + \Delta t$, as shown in Figure A.1. Each image is divided into smaller interrogation windows, where local particle motion is analyzed. A Fast Fourier Transform (FT) is applied to each window to convert spatial information into the frequency domain, followed by cross-correlation to identify the most probable displacement between the two frames. The inverse FT (FT^{-1}) is then used to transform the correlation function back into the spatial domain, where the peak represents the particle displacement. By dividing this displacement by the time delay Δt, velocity vectors are obtained, forming a complete velocity field [47]. A μPIV system consists of several key components that work together to capture and analyze microfluidic flow fields. The microfluidic device serves as the experimental platform, where fluid motion is observed under controlled conditions [47]. To

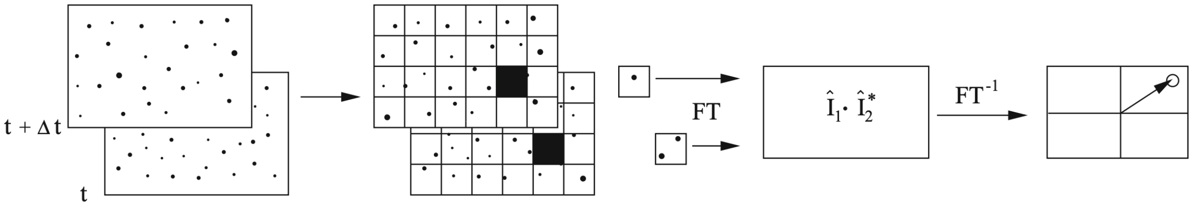

Figure A.1: μPIV analysis of double frame/single exposure recordings of digital cross-correlation method. Adapted from [47].

track flow velocity, tracer particles are suspended in the fluid, typically ranging in size from 200 nm to 2 μm [48]. An inverted microscope equipped with a high numerical aperture objective, often utilizing oil- or air-immersion lenses, is used to focus on the flow field. The system requires a flow driving mechanism, which may be pressure-driven or electrokinetic, depending on the application. A high-speed camera records images of the moving tracer particles, while an illumination source, such as a pulsed laser or continuous light, provides the necessary contrast for visualization. To enhance the signal-to-noise ratio, optical filters are used to isolate the fluorescence emission from tracer particles, ensuring high-contrast images suitable for cross-correlation analysis [47].

A.1.1 Limitations of µPIV

Despite its significant advantages in microscale fluid flow analysis, µPIV presents several inherent limitations that must be considered in experimental design and data interpretation. Microfluidic systems often operate in a viscosity-dominated regime where the Reynolds number is significantly less than one ($Re \ll 1$). Due to this, one major limitation of µPIV

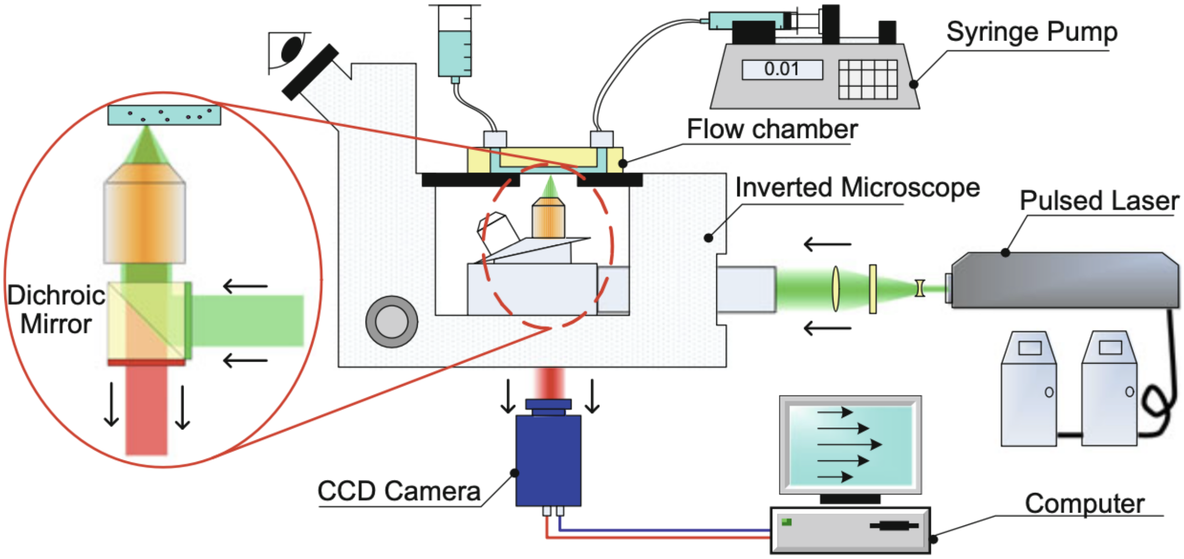

Figure A.2: Schematic of a typical 2D, planar µPIV system. A pulsed laser is used to illuminate fluorescent particles and a Charged Couple Device (CCD) camera is used to record the particle images. Adapted from [47].

is the effect of **Brownian motion** on tracer particles. At the microscale, thermal fluctuations induce random displacements in small tracer particles, which can introduce noise in velocity measurements, particularly at low flow velocities. Selecting appropriate tracer particles is critical to ensure accurate velocity measurements. The particles should be small enough to follow the flow faithfully but large enough to minimize Brownian motion effects [47, 49].

Meinhart et al. (2000) [44] and Olsen & Adrian (2000) [45] highlight **depth of correlation (DOC)** as a primary limitation, where out-of-focus particles contribute to the recorded signal, reducing spatial resolution and introducing errors, particularly in regions with velocity gradients. Additionally, **out-of-plane motion** affects the cross-correlation function, lowering the signal peak relative to background noise, making it difficult to extract accurate velocity measurements. To address these issues, Meinhart et al. (2000) propose a mathematical model to estimate and minimize the DOC, recommending high numerical aperture lenses and smaller tracer particles to enhance resolution. Olsen & Adrian (2000) complement this by refining correlation techniques to improve signal detection and reduce errors caused by out-of-plane motion.

Moreover, **wall effects and near-surface distortions** present difficulties in µPIV. Due to the finite DOC, velocity estimations near solid boundaries can be biased, particularly in regions with high velocity gradients. The limited optical sectioning capability of µPIV causes out-of-focus particles to contribute to the measurement signal, reducing spatial resolution and increasing uncertainty. Additionally, tracer particles may interact with the surface, altering their motion and further affecting measurement accuracy. These challenges highlight the need for improved optical configurations and refined data processing techniques to enhance near-wall velocity measurements in microfluidic flows [47].

A.1.2 Correlation Techniques in µPIV

Correlation techniques are fundamental to μPIV analysis, as they allow the determination of particle displacement by comparing two sequential images. The most widely used method is *cross-correlation*, which involves computing the displacement of tracer particles within interrogation windows by identifying the peak of the correlation function between two image frames [47]. Variations of this technique, such as *multi-pass correlation* and *adaptive windowing*, have been developed to improve spatial resolution and reduce measurement errors, particularly in high-shear flows. However, traditional correlation methods face challenges in low-speed microfluidic applications, where small particle displacements and noise can obscure the correlation peak. To address this, advanced techniques such as ensemble correlation have been introduced to enhance measurement accuracy by leveraging multiple image pairs [47].

Nguyen et al. [41] propose an *ensemble correlation* technique to improve the accuracy and reliability of μPIV measurements by averaging multiple image pairs instead of relying on a single-frame correlation. Traditional μPIV relies on individual image pairs to compute velocity fields, but in low-speed microfluidic flows, small particle displacements and background noise often degrade measurement accuracy. Ensemble correlation addresses this limitation by collecting a sequence of images and computing the correlation over multiple frames [41]. As illustrated in Figure A.3(a), this method involves acquiring a stack of images, denoted as $I_{1..N}$ and $I'_{1..N}$, where N represents the number of image pairs used. Instead of performing cross-correlation on a single image pair, the method selects the optimal representative image, $I_{\max}$ and $I'_{\max}$, by maximizing the correlation signal over all frames. The correlation function is then computed by averaging the cross-correlation from multiple image pairs, thereby reducing random noise and enhancing the signal-to-noise ratio.

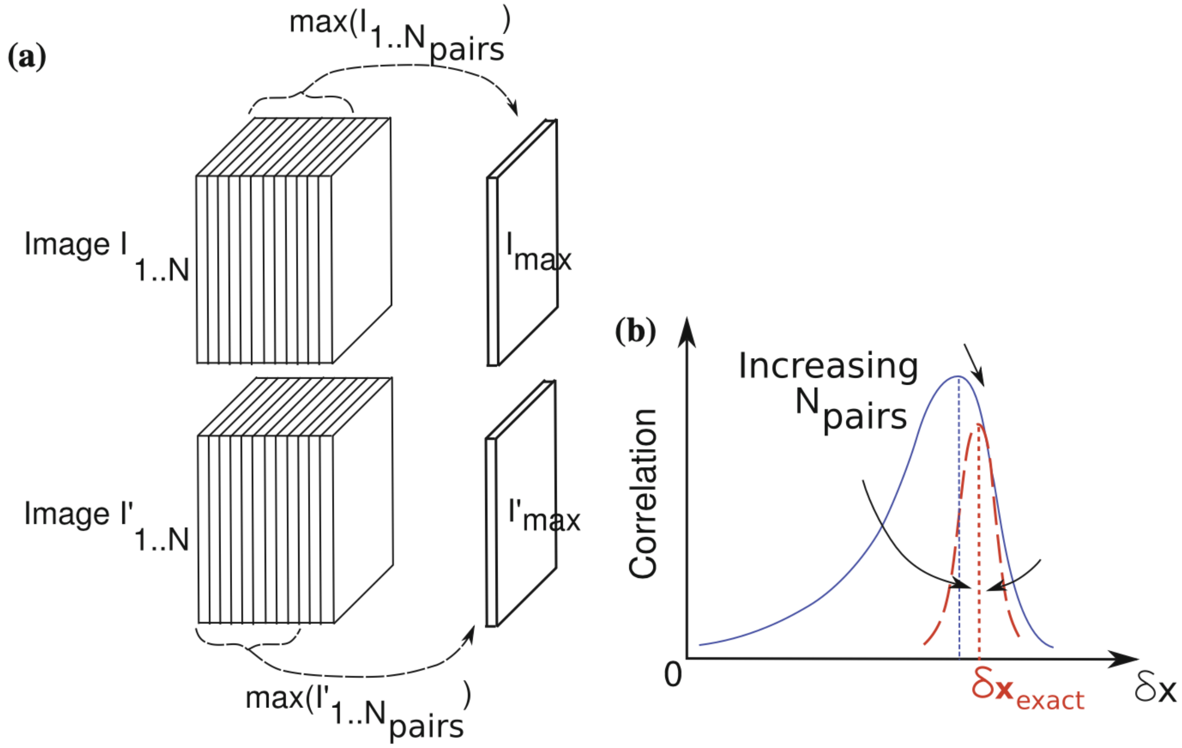

Figure A.3: Ensemble correlation technique from [41]. (a) A sequence of image pairs, $I_{1..N}$ and $I'_{1..N}$, is processed to select an optimized image pair, $I_{\max}$ and $I'_{\max}$, by maximizing the signal-to-noise ratio. (b) The effect of increasing N_{pairs} on the correlation peak.

A key advantage of this approach is its ability to refine the correlation peak, as shown in Figure A.3(b). Increasing the number of image pairs N_{pairs} sharpens the correlation function, minimizing the spread of displacement uncertainty δx [41]. This technique was also demonstrated by Pitts et al. [15] to be effective for analyzing blood flow in microchannels.

A.1.3 Application of μPIV in Blood Rheology Research

The application of µPIV is widely utilized for investigating flow phenomena in microchannels, particularly in biological experiments, where it has been employed to study blood flow in both *in vivo* and *in vitro* conditions. In *in vivo* studies, high-speed cameras are typically used, with RBCs serving as natural tracer particles [48]. Conversely, in *in vitro* applications, dual-pulsed imaging combined with fluorescent tracer particles is commonly employed to capture velocity field measurements [15, 50]. Pitts et al. [15] utilized μPIV to study blood flow in microchannels, focusing on the effects of Ht and shear rate on velocity distribution. Moreover, Werely et al. [51] demonstrated the capability of μPIV in measuring velocity fields within microchannels mimicking capillary networks. The technique allows for high-resolution analysis of plasma and RBC motion, enabling the quantification of the CFL.

A.2 Experimental Flow Measurements

Tables A.1, A.2, A.3, and A.4 display the measured flow rates tested for each channel size and fluid type (PBS and plasma), across a series of applied pressures (20 to 200 mBar). The flow rates for the 50 µm channel (Table A.3 for PBS and Table A.4 for plasma) are consistent with physiological conditions found in larger capillaries, with a range of flow rates scaled to accommodate different Hts. Similarly, for the 25 µm channel, Tables A.1 and A.2 present the flow rates adjusted for lower diameters, maintaining the physiological

WSR range for capillary blood flow.

Table A.1: Flow rate measurements for a 25 µm channel with PBS-suspension. Values are in [μL/min].

Pressure [mBar]	20.0	40.0	60.0	80.0	100.0	120.0	140.0	160.0	180.0	200.0
5% Ht	0.0190	0.0440	0.0700	0.0970	0.124	0.151	0.178	0.203	0.227	0.252
10% Ht	0.0160	0.0410	0.0680	0.0940	0.122	0.149	0.174	0.200	0.227	0.252
15% Ht	0.0190	0.0450	0.0720	0.0990	0.126	0.154	0.181	0.207	0.233	0.259
20% Ht	0.0190	0.0440	0.0700	0.0960	0.123	0.150	0.177	0.202	0.228	0.254

Table A.2: Flow rate measurements for a 25 µm channel with plasma-suspension. Values are in [μL/min].

Pressure [mBar]	20.0	40.0	60.0	80.0	100.0	120.0	140.0	160.0	180.0	200.0
5% Ht	0.0330	0.0580	0.0920	0.128	0.161	0.193	0.224	0.253	0.293	0.325
10% Ht	0.0200	0.0340	0.0560	0.0810	0.109	0.136	0.175	0.212	0.248	0.287
15% Ht	0.0240	0.0560	0.0870	0.123	0.156	0.191	0.224	0.254	0.280	0.308
20% Ht	0.0170	0.0430	0.0800	0.113	0.145	0.178	0.211	0.241	0.269	0.291

Table A.3: Flow rate measurements for a 50 µm channel with PBS-suspension. Values are in [μL/min].

Pressure [mBar]	20.0	40.0	60.0	80.0	100.0	120.0	140.0	160.0	180.0	200.0
5% Ht	0.373	0.726	1.13	1.54	1.94	2.36	2.76	3.18	3.59	4.00
10% Ht	0.362	0.715	1.07	1.45	1.79	2.18	2.39	2.77	3.23	3.55
15% Ht	0.267	0.632	0.993	1.41	1.77	2.21	2.54	2.60	3.03	3.48
20% Ht	0.308	0.648	1.04	1.44	1.80	2.15	2.59	2.97	3.37	3.77

Table A.4: Flow rate measurements for a 50 µm channel with plasma-suspension. Values are in [μL/min].

Pressure [mBar]	20.0	40.0	60.0	80.0	100.0	120.0	140.0	160.0	180.0	200.0
5% Ht	0.344	0.729	1.18	1.63	2.08	2.48	2.93	3.43	3.82	4.26
10% Ht	0.277	0.733	1.23	1.73	2.04	2.44	2.93	3.21	3.51	3.70
15% Ht	0.333	0.726	1.13	1.64	2.13	2.62	3.10	3.43	3.86	4.30
20% Ht	0.387	0.820	1.29	1.77	2.19	2.59	3.08	3.53	3.90	4.30

A.3 Core-Plasma Model Derivation

This section will go through the derivation of the model in more depth. We consider a fully developed, laminar flow in a cylindrical tube modeled as a two-layer fluid system. The outer layer, near the tube wall, consists of a Newtonian fluid with viscosity μ_p, while the core region comprises a non-Newtonian power-law fluid.

A.3.1 GOVERNING EQUATIONS AND ASSUMPTIONS

We begin with the axial component of the Navier–Stokes equation in cylindrical coordinates for an incompressible, Newtonian fluid:

$$\rho\left(\frac{\partial u}{\partial t}+u\frac{\partial u}{\partial z}+v\frac{\partial u}{\partial r}+\frac{w}{r}\frac{\partial u}{\partial \theta}\right)=-\frac{\partial p}{\partial z}+\mu_p\left[\frac{1}{r}\frac{d}{dr}\left(r\frac{du}{dr}\right)\right] \tag{A.1}$$

We apply the following assumptions:

- **Steady flow:** $\frac{\partial u}{\partial t}=0$

  The system is time-invariant, meaning conditions do not change with time, which reflects experimental conditions with constant flow rate.

- **Fully developed flow:** $\frac{\partial u}{\partial z}=0$

  Far from the inlet, the flow profile becomes constant along the length of the tube, eliminating axial derivatives of velocity.

- **Unidirectional flow:** $v=w=0$, $u=u(r)$

  Blood flows primarily along the axial direction in cylindrical vessels; radial and circumferential velocities are negligible.

- **Axisymmetric:** $\frac{\partial}{\partial \theta}=0$

  The geometry and flow are symmetric about the central axis of the vessel.

- **Newtonian fluid:** constant viscosity μ_p

  In the plasma or cell-free layer, blood behaves approximately like a Newtonian fluid due to the absence of RBCs.

- **Neglect body forces**

  Effects like gravity are negligible compared to the pressure-driven forces in microcirculatory flow.

Under these assumptions, the equation simplifies to:

$$0 = -\frac{dp}{dz} + \mu_p \left(\frac{1}{r} \frac{d}{dr} \left(r \frac{du}{dr} \right) \right) \tag{A.2}$$

Rearranging:

$$\frac{1}{r} \frac{d}{dr} \left(r \mu_p \frac{du}{dr} \right) = \frac{dp}{dz} \tag{A.3}$$

Assuming a constant pressure gradient:

$$\frac{dp}{dz} = -\frac{\Delta P}{L} \tag{A.4}$$

We define the pressure drop ΔP to be positive, so we write:

$$\frac{1}{r} \frac{d}{dr} \left(r \mu_p \frac{du}{dr} \right) = \frac{\Delta P}{L} \tag{A.5}$$

Newtonian CFL Region

We perform the integration of the governing equation with respect to r:

$$r\mu_p \frac{du}{dr} = \frac{\Delta P}{2L} r^2 + C_0 \tag{A.6}$$

Solving for $\frac{du}{dr}$:

$$\frac{du}{dr} = \frac{\Delta P}{2\mu_p L} r + \frac{C_0}{\mu_p r} \tag{A.7}$$

Define $C_1 = \frac{C_0}{\mu_p}$ to simplify notation:

$$\frac{du}{dr} = \frac{\Delta P}{2\mu_p L} r + \frac{C_1}{r} \tag{A.8}$$

Integrating:

$$u(r) = \frac{\Delta P}{4\mu_p L} r^2 + C_1 \ln(r) + C_2 \tag{A.9}$$

Now we defer solving for C_1 and C_2 until we analyze the core region.

Non-Newtonian Core Region

In the core region ($0 \leq r \leq R - \delta$), we model blood as a power-law fluid:

$$\tau_{rz} = K \left(\frac{du}{dr} \right)^n \tag{A.10}$$

Using the same momentum balance:

$$\frac{1}{r} \frac{d}{dr} \left(r\tau_{rz} \right) = \frac{\Delta P}{L} \tag{A.11}$$

Substitute power-law relation:

$$\frac{1}{r}\frac{d}{dr}\left(rK\left(\frac{du}{dr}\right)^n\right) = \frac{\Delta P}{L} \tag{A.12}$$

Multiply both sides by r:

$$\frac{d}{dr}\left(rK\left(\frac{du}{dr}\right)^n\right) = \frac{\Delta P}{L}r \tag{A.13}$$

Integrating:

$$rK\left(\frac{du}{dr}\right)^n = \frac{\Delta P}{2L}r^2 + C_3 \tag{A.14}$$

Step 1: Using Symmetry to Determine C_3 (Non-Newtonian)

In cylindrical flow, the centerline corresponds to the axis of symmetry. At this location, the shear stress must be zero because there is no fluid above or below the axis to exert a tangential force. Mathematically, this gives:

$$\tau_{rz}(r = 0) = 0 \tag{A.15}$$

From our earlier integration in the core (non-Newtonian) region, we had:

$$rK\left(\frac{du}{dr}\right)^n = \frac{\Delta P}{2L}r^2 + C_3 \tag{A.16}$$

We now substitute $r = 0$ into this equation to solve for C_3:

$$0 \cdot K \left(\left. \frac{du}{dr} \right|_{r=0} \right)^n = \frac{\Delta P}{2L} \cdot 0^2 + C_3 \tag{A.17}$$

$$0 = 0 + C_3 \tag{A.18}$$

Therefore:

$$C_3 = 0 \tag{A.19}$$

Resulting expression:

Substituting $C_3 = 0$ back into the equation gives:

$$rK \left(\frac{du}{dr} \right)^n = \frac{\Delta P}{2L} r^2 \tag{A.20}$$

Dividing both sides by r (for $r \neq 0$) yields:

$$K \left(\frac{du}{dr} \right)^n = \frac{\Delta P}{2L} r \tag{A.21}$$

Solving for $\frac{du}{dr}$:

$$\frac{du}{dr} = \left(\frac{\Delta P}{2KL} \right)^{1/n} r^{1/n} \tag{A.22}$$

Integrating:

$$u(r) = \left(\frac{\Delta P}{2KL} \right)^{1/n} \cdot \frac{n}{n+1} r^{(n+1)/n} + C_4 \tag{A.23}$$

Step 2: Continuity of Shear Stress to Determine C_1 (Newtonian)

We obtained the general velocity expression for the Newtonian region (CFL), which included an undetermined integration constant (equation (9)). At the interface $r = R - \delta$, the shear stress must be continuous:

$$\tau_{\text{core}} = \tau_{\text{cfl}} \tag{A.24}$$

From core:

$$\tau_{\text{core}} = K \left(\left. \frac{du}{dr} \right|_{r=R-\delta} \right)^n = \frac{\Delta P}{2L}(R - \delta) \tag{A.25}$$

From CFL:

$$\tau_{\text{cfl}} = \mu_p \left(\left. \frac{du}{dr} \right|_{r=R-\delta} \right) = \mu_p \left(\frac{\Delta P}{2\mu_p L}(R - \delta) + \frac{C_1}{R - \delta} \right) = \frac{\Delta P}{2L}(R - \delta) + \frac{C_1}{R - \delta} \tag{A.26}$$

Equating both:

$$\frac{\Delta P}{2L}(R - \delta) = \frac{\Delta P}{2L}(R - \delta) + \frac{C_1}{R - \delta} \Rightarrow \frac{C_1}{R - \delta} = 0 \Rightarrow C_1 = 0 \tag{A.27}$$

Thus, $C_1 = 0$ and the logarithmic term in the CFL velocity profile vanishes.

Step 3: Boundary Condition to Determine C_2 (Newtonian)

To determine the remaining constant C_2 in the Newtonian region, we apply a no-slip boundary condition at the vessel wall, $r = R$:

$$u(R) = 0 \tag{A.28}$$

Recall in the Newtonian region with $C_1 = 0$:

$$u(r) = \frac{\Delta P}{4\mu_p L} r^2 + C_2 \tag{A.29}$$

Substitute $u(R) = 0$:

$$0 = \frac{\Delta P}{4\mu_p L} R^2 + C_2 \tag{A.30}$$

$$C_2 = -\frac{\Delta P}{4\mu_p L} R^2 \tag{A.31}$$

Final Velocity Profile in the Newtonian CFL

Substituting C_2 into the velocity expression:

$$u(r) = \frac{\Delta P}{4\mu_p L} (r^2 - R^2) \tag{A.32}$$

Step 4: Continuity of Velocity to Determine C_4 (Non-Newtonian)

At $r = R - \delta$:

$$\left(\frac{\Delta P}{2KL}\right)^{1/n} \cdot \frac{n}{n+1} (R-\delta)^{(n+1)/n} + C_4 = \frac{\Delta P}{4\mu_p L} ((R-\delta)^2 - R^2) \tag{A.33}$$

Solving for C_4:

$$C_4 = \frac{\Delta P}{4\mu_p L}((R-\delta)^2 - R^2) - \left(\frac{\Delta P}{2KL}\right)^{1/n} \cdot \frac{n}{n+1}(R-\delta)^{(n+1)/n} \tag{A.34}$$

Final Velocity Profile in the Non-Newtonian Core

Substitute C_4 into the general expression for u(r):

$$u(r) = \left(\frac{\Delta P}{2KL}\right)^{1/n} \cdot \frac{n}{n+1} r^{(n+1)/n} + \frac{\Delta P}{4\mu_p L}((R-\delta)^2 - R^2) - \left(\frac{\Delta P}{2KL}\right)^{1/n} \cdot \frac{n}{n+1}(R-\delta)^{(n+1)/n} \tag{A.35}$$

Overall Simplified Core-Plasma Model

$$u(r) = \begin{cases} \dfrac{\Delta P}{4\mu_p L}(r^2 - R^2), & r \geq R - \delta \\[2em] \left(\dfrac{\Delta P}{2KL}\right)^{1/n} \cdot \dfrac{n}{n+1}\left(r^{(n+1)/n} - (R-\delta)^{(n+1)/n}\right) + \dfrac{\Delta P}{4\mu_p L}\left((R-\delta)^2 - R^2\right), & r < R - \delta \end{cases} \tag{A.36}$$

A.3.2 FLOW RATE

Newtonian CFL Region

To calculate the volumetric flow rate Q in the Newtonian layer (between $R-\delta$ and R), we integrate the velocity profile $u(r)$ over the cross-sectional area:

$$Q = 2\pi \int_{R-\delta}^{R} u(r) r \, dr$$

Substituting $u(r)$:

$$Q = 2\pi \int_{R-\delta}^{R} \frac{\Delta P}{4\mu_p L}(r^2 - R^2) r \, dr$$

Solving the integral:

$$Q = 2\pi \frac{\Delta P}{4\mu_p L} \int_{R-\delta}^{R} (r^3 - R^2 r) \, dr$$

Evaluating each term:

$$\int_{R-\delta}^{R} r^3 \, dr = \left[\frac{r^4}{4}\right]_{R-\delta}^{R} = \frac{R^4}{4} - \frac{(R-\delta)^4}{4}$$

$$\int_{R-\delta}^{R} R^2 r \, dr = R^2 \left[\frac{r^2}{2}\right]_{R-\delta}^{R} = R^2 \left(\frac{R^2}{2} - \frac{(R-\delta)^2}{2}\right)$$

Combining the results:

$$Q = \frac{\pi \Delta P}{2\mu_p L}\left(-R^2\delta^2 + R\delta^3 - \frac{1}{4}\delta^4\right)$$

Non-Newtonian Core Region

To calculate the volumetric flow rate Q within the non-Newtonian core, we integrate the velocity profile $u(r)$ over the cross-sectional area from $r = 0$ to $r = R - \delta$. The velocity distribution in this region is given by:

$$u(r) = \left(\frac{\Delta P}{2KL}\right)^{1/n} \frac{n}{n+1} r^{(n+1)/n} + \frac{\Delta P}{4\mu_p L}\left((R-\delta)^2 - R^2\right) - \left(\frac{\Delta P}{2KL}\right)^{1/n} \frac{n}{n+1}(R-\delta)^{(n+1)/n}$$

The volumetric flow rate Q is obtained by integrating $u(r) \cdot r$ over the area:

$$Q = 2\pi \int_0^{R-\delta} u(r)\, r\, dr$$

Substituting the full expression for $u(r)$ into the integral:

$$\begin{aligned} Q = 2\pi \int_0^{R-\delta} \Bigg[\left(\frac{\Delta P}{2KL}\right)^{1/n} \frac{n}{n+1} r^{(n+1)/n} + \frac{\Delta P}{4\mu_p L}\left((R-\delta)^2 - R^2\right) \\ - \left(\frac{\Delta P}{2KL}\right)^{1/n} \frac{n}{n+1}(R-\delta)^{(n+1)/n} \Bigg] r\, dr \end{aligned}$$

This integral can be separated into three simpler integrals, each corresponding to one term in the expression:

1. Power-law term:

$$I_1 = \left(\frac{\Delta P}{2KL}\right)^{1/n} \frac{n}{n+1} \int_0^{R-\delta} r^{(2n+1)/n}\, dr = \left(\frac{\Delta P}{2KL}\right)^{1/n} \frac{n}{n+1} \cdot \frac{(R-\delta)^{(2n+1)/n+1}}{(2n+1)/n+1}$$

2. Constant shift term:

$$I_2 = \frac{\Delta P}{4\mu_p L}\left((R-\delta)^2 - R^2\right) \int_0^{R-\delta} r\, dr = \frac{\Delta P}{4\mu_p L}\left((R-\delta)^2 - R^2\right) \cdot \frac{(R-\delta)^2}{2}$$

3. Offset correction term:

$$I_3 = \left(\frac{\Delta P}{2KL}\right)^{1/n} \frac{n}{n+1}(R-\delta)^{(n+1)/n} \int_0^{R-\delta} r\, dr = \left(\frac{\Delta P}{2KL}\right)^{1/n} \frac{n}{n+1}(R-\delta)^{(n+1)/n} \cdot \frac{(R-\delta)^2}{2}$$

Combining all three terms:

$$\begin{aligned}
Q &= 2\pi \cdot I_1 + 2\pi \cdot I_2 - 2\pi \cdot I_3 \\
&= 2\pi \left(\frac{\Delta P}{2KL}\right)^{1/n} \frac{n}{n+1} \cdot \frac{(R-\delta)^{(2n+1)/n+1}}{(2n+1)/n+1} \\
&\quad + \pi \frac{\Delta P}{2\mu_p L} \left((R-\delta)^4 - R^2(R-\delta)^2\right) \\
&\quad - \pi \left(\frac{\Delta P}{2KL}\right)^{1/n} \frac{n}{n+1} (R-\delta)^{(n+1)/n+2}
\end{aligned}$$

A.3.3 Shear Rate

Newtonian CFL Region ($R - \delta \leq r \leq R$)

The velocity profile in the Newtonian layer is:

$$u(r) = \frac{\Delta P}{4\mu_p L}(r^2 - R^2)$$

The shear rate, $\dot{\gamma}$, is the radial derivative of velocity:

$$\dot{\gamma} = \frac{du}{dr} = \frac{\Delta P}{4\mu_p L} \cdot 2r = \frac{\Delta P}{2\mu_p L} r$$

Non-Newtonian Core Region ($0 \leq r \leq R - \delta$)

The shear rate, $\dot{\gamma}$, in the non-Newtonian region is:

$$\dot{\gamma} = \frac{du}{dr} = \left(\frac{\Delta P}{2KL}\right)^{1/n} \frac{n}{n+1} \cdot \frac{n+1}{n} r^{1/n} = \left(\frac{\Delta P}{2KL}\right)^{1/n} r^{1/n}$$

A.3.4 Gradient of Shear Rate

The shear rate gradient, $\nabla\dot{\gamma}$, is the derivative of the shear rate with respect to r:

Newtonian CFL Region ($R - \delta \leq r \leq R$)

$$\nabla\dot{\gamma} = \frac{\Delta P}{2\mu_p L}$$

Non-Newtonian Core Region ($0 \leq r \leq R - \delta$)

$$\nabla\dot{\gamma} = \frac{\left(\frac{\Delta P}{2KL}\right)^{1/n} r^{1/n-1}}{n}$$

A.4 Comparison of Imposed, Measured, and Optimized Pressure Drops

The imposed pressure gradient (∇P) is used as the driving force in the microfluidic setup to ensure controlled and reproducible flow. To validate its accuracy, we compare the imposed ΔP to measured and optimized values. Linear regression models were fitted for each dataset, yielding the following equations: $Y = 6200X + 794.5$ ($R^2 = 0.9823$) for 50 μm PBS,

$Y = 5256X + 1066$ ($R^2 = 0.9196$) for 50 μm plasma, $Y = 75685X + 662.4$ ($R^2 = 0.9992$) for 25 μm PBS, and $Y = 61129X + 1209$ ($R^2 = 0.9670$) for 25 μm plasma. The high R^2 values confirm the strong linear relationship between flow rate and pressure drop for the 25 μm channels, indicating minimal deviation from theoretical expectations. The slight deviations in the plasma cases are expected due to Ht-dependent viscosity variations. To determine the optimized ΔP, we use an unconstrained fitting approach that adjusted parameters to best match experimental flow characteristics. The optimized ΔP, known as ΔP_{exp} in this study, were then compared against the imposed and measured values. Measured ΔP is obtained by flowing water through the tubing system without the microfluidic chip to capture intrinsic resistance from the setup. The imposed ΔP closely aligns with the optimized and measured values, confirming its reliability for imposing this value as an initial condition in the code. This suggests that, for these experimental conditions, the pressure drop in the tubing can be considered negligible and does not significantly influence the overall flow behavior. However, slight deviations observed in plasma cases indicate that non-Newtonian effects and Ht-dependent variations may introduce minor discrepancies, which should be considered when working with higher-viscosity suspensions.

Figure A.5 compares the computed pressure drop from the Core-Plasma model (ΔP_{cp}) to the measured pressure drop (ΔP) across varying Ht levels in both 50 µm and 25 µm microchannels with PBS and plasma suspensions. The data generally follow the X=Y line, indicating good agreement between the model and experimental values. However, the model tends to slightly underestimate the pressure drop in plasma suspensions, particularly at higher pressures. This underestimation is expected, as the model assumes a simplified viscosity distribution, which may not fully capture the shear-dependent variations in plasma. Despite this, the Core-Plasma model is sufficient enough for predicting pressure drop trends.

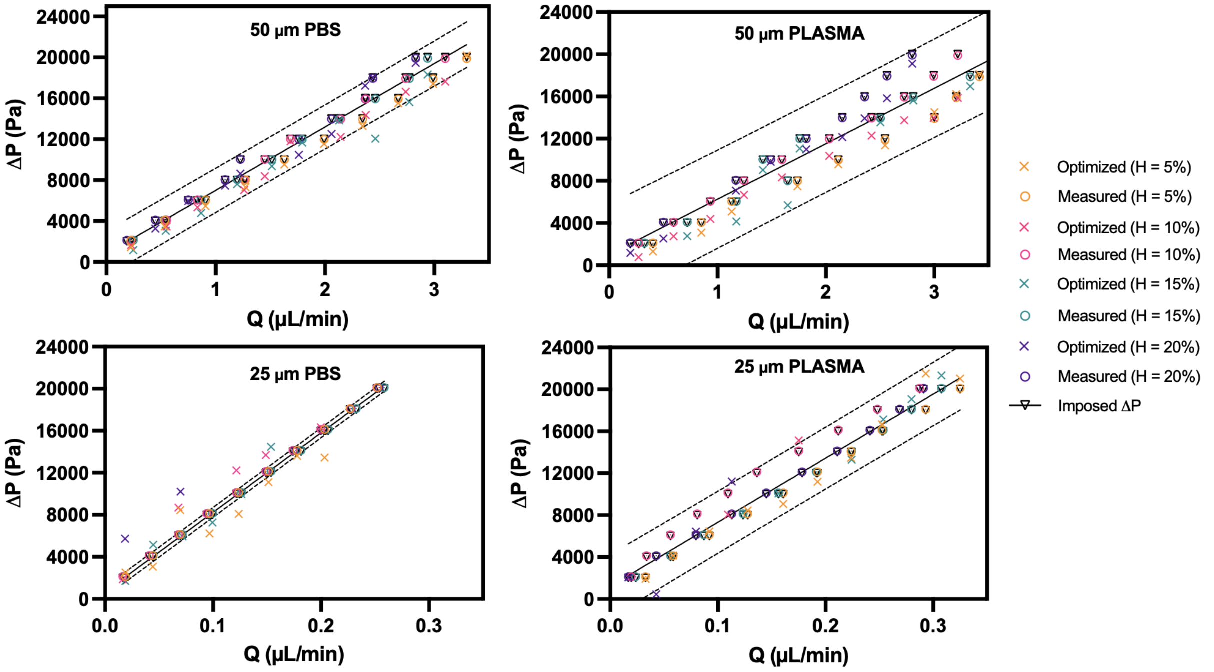

Figure A.4: Pressure drop (ΔP) as a function of flow rate (Q) for 50 µm (top) and 25 µm (bottom) microchannels with PBS (left) and plasma (right) suspensions. The **imposed pressure drop** (black triangles) represents the set pressure in the Fluigent system, while the **measured pressure drop** (circles) is obtained from direct flow measurements. The **optimized pressure drop** (crosses) is derived from model fitting across varying hematocrits (5%, 10%, 15%, 20%). The dashed lines indicate expected theoretical bounds. The results demonstrate strong agreement between the imposed and measured values, validating the use of imposed pressure drop for flow characterization in microchannels.

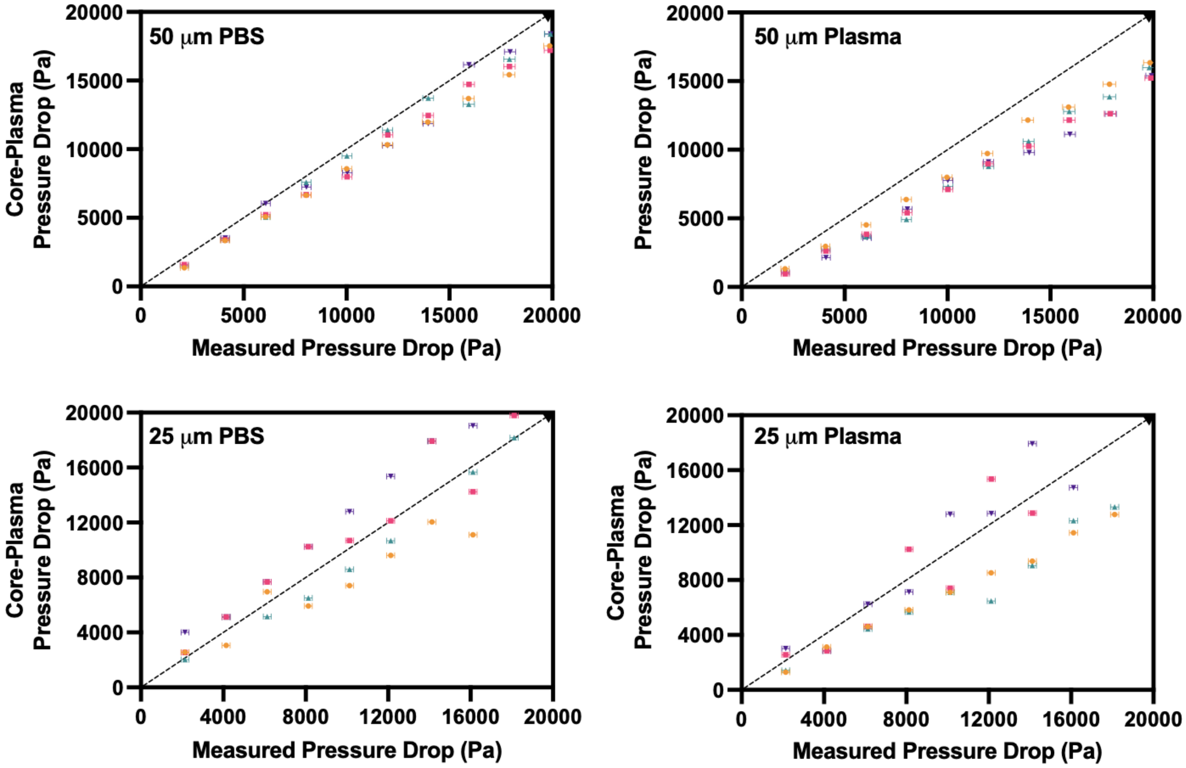

Figure A.5: Computed pressure drop from Core-Plasma Model (ΔP_{cp}) compared to measured pressure drop (ΔP) for 50 µm (top) and 25 µm (bottom) microchannels with PBS (left) and plasma (right) suspensions. The measured pressure drop is obtained from direct flow measurements. The computed pressure drop is obtained from Core-Plasma model fitting across varying hematocrits (5%, 10%, 15%, 20%). An X=Y line is plotted to for visualization of the trends.

REFERENCES

1. Popel, A. S. & Johnson, P. C. Microcirculation and Hemorheology. Annual Review of Fluid Mechanics **37,** 43–69 (2005).
2. Fedosov, D., Caswell, B., Popel, A. & Karniadakis, G. Blood Flow and Cell-Free Layer in Microvessels. Microcirculation **17,** 615–628 (2010).
3. Hendricks, N. E. The Microcirculation. Southern African Journal of Anaesthesia and Analgesia **26,** S62–S65 (2020).
4. Katanov, D., Gekle, M. & Wagner, C. Lift Force and Hematocrit Dependence of Red Blood Cell Resistance in Simulated Blood Flow. Scientific Reports **5,** 13162 (2015).
5. Fahraeus, R. & Lindqvist, T. The Viscosity of the Blood in Narrow Capillary Tubes. American Journal of Physiology **96,** 562–568 (1931).
6. Zhang, J., Johnson, P. C. & Popel, A. S. Effects of RBC Deformability and Aggregation on the Cell-Free Layer and Apparent Viscosity of Microscopic Blood Flows. Microvascular Research **77,** 265–272 (2009).
7. Reinke, W., Gaehtgens, M. & Johnson, H. C. Blood Viscosity in Small Tubes: Effect of Shear Rate, Aggregation, and Sedimentation. American Journal of Physiology-Heart and Circulatory Physiology **253,** H540–H547 (1987).
8. Pries, A. R., Neuhaus, D. & Gaehtgens, P. Blood Viscosity in Tube Flow: Dependence on Diameter and Hematocrit. American Journal of Physiology-Heart and Circulatory Physiology **263,** H1770–H1778 (1992).
9. Bugliarello, G. & Sevilla, J. Velocity Distribution and Other Characteristics of Steady and Pulsatile Blood Flow in Fine Glass Tubes. Biorheology **7,** 85–107 (1970).
10. Li, X. & Zhou, Y. Microfluidic Devices for Biomedical Applications (Woodhead Publishing, Cambridge, UK, 2013).
11. Chandran, K. B., Rittgers, S. E. & Yoganathan, A. P. Biofluid Mechanics: Part II – Biomechanics of the Human Circulation (Taylor & Francis Group, Boca Raton, FL, USA, 2012).
12. Merrill, E. W. et al. Rheology of Blood and Flow in the Microcirculation. Journal of Applied Physiology **18,** 255–260 (1963).
13. Haynes, R. H. & Burton, A. C. Role of the Non-Newtonian Behavior of Blood in Hemodynamics. American Journal of Physiology **197,** 943–950 (1959).

14. Sarelius, I. H. & Duling, B. R. Direct Measurement of Microvessel Hematocrit, Red Cell Flux, Velocity, and Transit Time. American Journal of Physiology-Heart and Circulatory Physiology **243,** H1018–H1026 (1982).

15. Pitts, K. L. & Fenech, M. Micro-particle Image Velocimetry for Velocity Profile Measurements of Micro Blood Flows. Journal of Visualized Experiments (JoVE), 50314 (2013).

16. Mehri, R., Mavriplis, C. & Fenech, M. Red Blood Cell Aggregates and Their Effect on Non-Newtonian Blood Viscosity at Low Hematocrit in a Two-Fluid Low Shear Rate Microfluidic System. PLOS ONE **13,** e0199911 (2018).

17. Fenech, M. & Haya, L. in Cardiovascular Mechanics 1st, 27 (CRC Press, Boca Raton, FL, USA, 2018).

18. Zhang, J., Johnson, P. C. & Popel, A. S. Effects of Erythrocyte Deformability and Aggregation on the Cell-Free Layer and Apparent Viscosity of Microscopic Blood Flows. Microvascular Research **77,** 265–272 (2009).

19. Brust, M. et al. The Plasma Protein Fibrinogen Stabilizes Clusters of Red Blood Cells in Microcapillary Flows. Scientific Reports **4,** 4348 (2014).

20. Fenech, M., Le, A. V., Salame, M., Gliah, O. & Chartrand, C. Semi-automated Red Blood Cell Core Detection in Blood Micro-flow. Microvascular Research **147,** 104496 (2023).

21. Thiébaud, M. D., Abkarian, M. & Misbah, C. Hydrodynamic Lift of Vesicles and Red Blood Cells in a Microchannel. Physical Review Fluids **6,** 033602 (2021).

22. Cantat, I. & Misbah, C. Lift Force and Dynamical Unbinding of Adherent Vesicles Under Shear Flow. Physical Review Letters **83,** 880–883 (1999).

23. Coupier, G., Kaoui, B., Podgorski, T. & Misbah, C. Noninertial Lateral Migration of Vesicles in Bounded Poiseuille Flow. Physical Review Letters **100,** 178106 (2008).

24. Kumar, A. & Graham, M. D. Cell to Cell Diffusion and Single Particle Dispersion in Blood Flow. Physical Review E **86,** 041924 (2012).

25. Grandchamp, X., Coupier, G., Srivastav, A., Thiébaud, M. D. & Podgorski, T. Cell-Cell Interactions in Suspensions of Red Blood Cells: Attraction and Alignment. Physical Review Letters **110,** 108101 (2013).

26. Leighton, D. & Acrivos, A. The Shear-Induced Migration of Particles in Concentrated Suspensions. Journal of Fluid Mechanics **181,** 415–439 (1987).

27. Damiano, E. R. The Effect of the Endothelial-Cell Glycocalyx on the Motion of Red Blood Cells through Capillaries. Microvascular Research **55,** 77–91 (1998).

28. Reinke, W., Johnson, P. C. & Gaehtgens, P. Effect of Shear Rate Variation on Apparent Viscosity of Human Blood in Tubes of 29 to 94 μm Diameter. Circulation Research **59,** 124–132 (1986).

29. Cerdeira, T. et al. Determination of the cell-free layer in circular PDMS microchannels in Proceedings of VIPIMAGE 2009 (ECCOMAS, Porto, Portugal, 2009).

30. Maeda, N., Seiyama, T. & Shiga, T. Erythrocyte Flow and Elasticity of Microvessels Evaluated by Marginal Cell-Free Layer and Flow Resistance. Biorheology **33,** 235–252 (1996).

31. Hariprasad, D. S. & Secomb, T. W. Two-Dimensional Simulation of Red Blood Cell Motion Near a Wall Under a Lateral Force. Physical Review E **90,** 053014 (2014).

32. Jamshidi, R., Gillissen, J. J. J., Angeli, P. & Mazzei, L. Roles of Solid Effective Stress and Fluid-Particle Interaction Force in Modeling Shear-Induced Particle Migration in Non-Brownian Suspensions. Physical Review Fluids **6,** 014301 (2021).

33. Chow, A. W., Sinton, S. W., Iwamiya, J. H. & Stephens, T. S. Shear-Induced Particle Migration in Couette and Parallel-Plate Viscometers: NMR Imaging and Stress Measurements. Physics of Fluids **6,** 2561–2566 (1994).

34. Semwogerere, D. & Weeks, E. R. Shear-Induced Particle Migration in Binary Colloidal Suspensions. Physics of Fluids **20,** 043306 (2008).

35. Koutsiaris, A. G. A Velocity Profile Equation for Blood Flow in Small Arterioles and Venules of Small Mammals *in vivo* and an Evaluation Based on Literature Data. Clinical Hemorheology and Microcirculation **43,** 321–334 (2009).

36. Bauersachs, R. M., Wenby, R. B. & Meiselman, H. J. Determination of Specific Red Blood Cell Aggregation Indices via an Automated System. Clinical Hemorheology **9,** 1–25 (1989).

37. Chartrand, C., Le, A. V. & Fenech, M. Micro-particle Image Velocimetry for Blood Flow in Thick Round Glass Micro-channels: Channel Fabrication and Velocity Profile Characterization. MethodsX **10,** 102110 (2023).

38. Bruns, D. E. & Knowler, W. C. Stabilization of Glucose in Blood Samples: Why It Matters. Clinical Chemistry **55,** 850–852 (2009).

39. Wijk, R. V. & Solinge, W. W. V. The Energy-Less Red Blood Cell Is Lost: Erythrocyte Enzyme Abnormalities of Glycolysis. Blood **106,** 4034–4042 (2005).

40. Baskurt, O., Neu, B. & Meiselman, H. J. Red Blood Cell Aggregation (CRC Press, Boca Raton, FL, USA, 2011).

41. Nguyen, C. V., Fouras, A. & Carberry, J. Improvement of Measurement Accuracy in Micro PIV by Image Overlapping. Experimental Fluids **49,** 885–899 (2010).

42. Jr., R. E. W. & Merrill, E. W. Influence of Flow Properties of Blood upon Viscosity-Hematocrit Relationships. Journal of Clinical Investigation **41,** 1591–1598 (1962).

43. Cho, Y. I. & Kensey, K. R. Effects of the Non-Newtonian Viscosity of Blood on Flows in a Diseased Arterial Vessel. Part 1: Steady Flows. Biorheology **28,** 241–262 (1991).

44. Meinhart, C. D., Wereley, S. & Gray, M. Volume Illumination for Two-Dimensional Particle Image Velocimetry. Measurement Science and Technology **11,** 809–814 (2000).

45. Olsen, M. G. & Bourdon, C. J. Out-of-Plane Motion Effects in Microscopic Particle Image Velocimetry. Journal of Fluids Engineering **125,** 895–901 (2003).

46. Baskurt, O. K. & Meiselman, H. J. Blood Rheology and Hemodynamics. Seminars in Thrombosis and Hemostasis **29,** 435–450 (2003).
47. Raffel, M., Willert, C. E., Scarano, F. & Kähler, C. J. Particle Image Velocimetry 3rd (Springer-Verlag, Berlin, Germany, 2018).
48. Sugii, Y., Nishio, S. & Okamoto, K. In Vivo PIV Measurement of Red Blood Cell Velocity Field in Microvessels Considering Mesentery Motion. Physiological Measurement **23,** 403–416 (2002).
49. Santiago, J. G., Wereley, S., Meinhart, C., Beebe, D. & Adrian, R. J. A Particle Image Velocimetry System for Microfluidics. Experiments in Fluids **25,** 316–319 (1998).
50. Pitts, K. L., Mehri, R., Mavriplis, C. & Fenech, M. Micro-Particle Image Velocimetry Measurement of Blood Flow: Validation and Analysis of Data Pre-Processing and Processing Methods. Measurement Science and Technology **23,** 115302 (2012).
51. Wereley, S. T. & Meinhart, C. D. Recent Advances in Micro-Particle Image Velocimetry. Annual Review of Fluid Mechanics **42,** 557–576 (2009).